HIGH-PERFORMANCE QUANTUM DOT LASERS AND INTEGRATED GUIDED-WAVE DEVICES ON SILICON

by

Jun Yang

A dissertation submitted in partial fulfillment
of the requirements for the degree of
Doctor of Philosophy
(Electrical Engineering)
in The University of Michigan
2008

Doctoral Committee:

Professor Pallab K. Bhattacharya, Chair
Professor Duncan G. Steel
Assistant Professor Jamie Phillips
Assistant Professor Kevin P. Pipe

To my family

ACKNOWLEDGEMENTS

This thesis would not have been accomplished without the support, collaboration, and inspiration of many people. First, I would like to express my sincere gratitude to my advisor, Prof. Pallab Bhattacharya, who has introduced me into the field of quantum dot optoelectronics, and has given me constant guidance, support, and help. The rigorous professional training and what I have learned from him is invaluable throughout my career. I specially thank Prof. Duncan Steel for his tremendous support and encouragement that has kept me inspired during difficult moments. I am also very grateful to other members of my doctoral committee, Prof. Jamie Phillips and Prof. Kevin Pipe, for their strong support and helpful advice.

The collaboration with many excellent researchers makes the challenging research journey more enjoyable. I greatly thank Prof. Zetian Mi for excellent collaboration in the early part of the project of quantum dot lasers on silicon. I also thank Prof. P. K. L Chan for his contribution to thermal imaging and reliability testing in this project. I would like to thank Prof. Zhenqiang Ma, Dr. Hao-Chih Yuan and Guoxuan Qin in University of Wisconsin for their collaboration on CMOS integration and silicon membrane transfer. I also appreciate Prof. Jian Xu and Ting Zhu in Pennsylvania State University for fabricating PbSe colloidal quantum dots. I specially thank Dr. Juraj Topolancik for great help with the design and fabrication of random photonic crystal microcavities, Dr. Kai Sun at EMAL of the University of Michigan for significant help with TEM study of quantum

dot dislocation filtering, and Tim Murphy for his mentorship in molecular beam epitaxy growth technique and cleanroom processing.

Especially, I would like to thank Prof. Herbert Winful for his insightful discussion to tackle the puzzle of Gouy phase shifts, and Prof. Fred Terry, Prof. Lingjie Guo, and Prof. Stephen Rand for their help and support in my graduate study.

I am thankful to other colleagues in our group for their friendship and technical support: Dr. Carl Fischer, Dr. Sasan Fathpour, Dr. Subhananda Chakrabarti, Dr. Zhimei Zhu, and Dr. Xiaohua Su, Dr. Mike Holub, Dr. Jonghyun Shin, Dr. Swapnajit Chakravarty, Zhuang Wu, Guan Huang, Dipankar Saha, Debashish Basu, Meng Zhang, Chung-Chiang Wu, Jeremy Moore, Junseok Heo, Chi-Sen Lee, and Ayan Paul. Especially, I would like to thank Dr. Yuan Xie, Dr. Xin Zhu, Dr. Yang Li, Dr. Xing Cheng, Dr. Guangyu Li, Dr. Guoqing Chang, Dr. Bin Li, Dan Shi, Cheng Peng, Dr. Zhishan Hua, Dr. Ming Yang, Dr. Wen-Lung Huang, Dr. Xiaochuan Bi, Dr. Guangyuan Zhao, Dr. Ding-Yuan Chen, Dr. Haiping Sun, Dr. Yu-Wei Lin, Dr. Jing Wang, Sheng-Shian Li, Dr. Dawen Li, Zeying Ren, Yuhai Mei, and Ning Gulari, Xinen Zhu, Weiming Wang, Weibin Zhu, Tao Lin, Emine Cagin, Alex Guo, Willie Bowen, Xiaoyang Cheng, Tao Li, Li-Jing Cheng, Myung-Gyu Kang, and George Meng for helpful discussion in processing and measurements.

The excellent technical support of the staff members, Dennis Schweiger, Terre Briggs, Brian VanDerElzen, Gregory Allion, Edward Tang, Matthew Oonk, Timothy Brock, Sandrine Martin, Fred Sequin, Russell Clifford, James Kulman, Katharine Beach, and Bill Knudsen in the Michigan Nanofabrication Facility is also greatly appreciated. I also thank Judi Scramlin, Melanie Caughey, Lisa Vogel, Deborah Swartz, Robin Rennie, Beth Stalnaker, Karen Liska, and Rebecca Turanski for administrative support throughout

my graduate career in Michigan.

I wish to acknowledge University of Michigan EECS department for offering fellowships to support my first-two-year graduate education, and the DARPA and AFOSR for funding this research.

I wish to express my deep gratitude to my parents Meiying Guo and Mingzheng Yang, and my sister Liu Yang for their love, patience, and support. Finally, I would like to thank my wife, Dr. Ying Yao, for her love, support, and encouragement.

TABLE OF CONTENTS

LIST OF FIGURES

LIST OF TABLES

LIST OF APPENDICES

ABSTRACT

Optical interconnects, the chip-scale integration of optoelectronic devices with complementary-metal-oxide-semiconductor (CMOS) silicon circuits, provide a promising approach for the realization of the next-generation high-speed computing and communication systems. Unfortunately, optoelectronics lacks an obvious platform for monolithic integration. One of the practical solutions is the hybrid integration, through heteroepitaxial growth, of compound semiconductor optoelectronic components with silicon technology. This thesis is devoted to developing high-performance GaAs-based quantum dot lasers directly grown on silicon substrates and their monolithic integration with waveguides and electroabsorption modulators. The investigation of 1.5 μm silicon-based high-Q random photonic crystal microcavity light emitters utilizing PbSe colloidal quantum dots has also been conducted.

High-performance quantum dot lasers directly-grown on silicon substrates have been achieved in this study. The performance of III-V-based lasers on silicon can be degraded by the inherent high-density propagating dislocations. To enhance device performance, a novel quantum dot dislocation filter has been developed. The best lasers exhibit relatively low threshold current density (J_{th} = 900 A/cm^2), large small-signal modulation bandwidth of 5.5 GHz, and a high characteristic temperature (T_0 = 278 K).

The monolithic integration of InGaAs QD lasers with waveguides and quantum well (QW) electroabsorption modulators has been achieved through molecular beam epitaxy

(MBE) growth and regrowth. Focused-ion-beam milling is utilized to create high-quality etched GaAs facets with a reflectivity of 0.28 and coupling groove with coupling coefficient greater than 20%. Quantum-dot lasers with focused-ion-beam-etched facets exhibit comparable performance to those with cleaved facets. The integrated modulator exhibits a modulation depth ~100% at 5 V reverse bias. In addition, the monolithic integration of the amorphous silicon waveguide with quantum dot laser has also been demonstrated by using plasma-enhanced-chemical-vapor deposition (PECVD).

Finally, enhanced photoluminescence at 1.5 μm wavelength has been observed from PbSe colloidal quantum dots embedded in a silicon-based random photonic crystal microcavity. Such microscale light sources on silicon can also be fabricated or integrated on silicon CMOS chips, which may provide a viable route for inter- and intrachip optical communications.

CHAPTER 1

INTRODUCTION

During the past decades, the microelectronics industry has been pursuing high-speed computers by shrinking transistor size and increasing integration density. This development trend is described by Moore's law which predicts that the number of transistors that can be placed on a computer chip, at proportionate decrease in cost, would double approximately every two years [1]. However, the progress is gradually slowing down due to effects related to the (small) transistor size and due to transmission delay and heat dissipation issues in high-density integration architectures. A detailed discussion on the limitations we have to face at present and in the future can be found in the book "*Future trends in Microelectronics*" [2]. As a result, microprocessor developers are currently in favor of multiple core processors instead of merely increasing the core-clock speed. However, even the emerging 3-D circuits based on vertical interconnects are measures which eventually cannot satisfy the ever-increasing demands on high speed information switching and communications. So what is the solution? The next-generation computers based on quantum computing [3] or bio-technology [4] are still elusive. Considering their feasibility and reliability, optical interconnect systems which require chip-scale integration of optical and electronic components are prevailing as promising substitutes for current microelectronic chips [5] [6]. Optical interconnects can not only provide higher

bandwidth for computing and switching, but also provide advantages such as inherent parallel processing without crosstalk and lower power dissipation. In fact, discrete optical components such as optics fibers and their links have been employed in communication network since 1980's.

1.1. Emission, Modulation, and Guiding of Light in Silicon

Conventional photonic devices such as lasers/amplifiers, waveguides, modulators and filters are fabricated using various materials including III-V semiconductors, glass and $LiNbO_3$, etc. For discrete components, these materials are preferred due to their excellent optical properties and optoelectronic capabilities in specific applications. However, high-speed optical interconnect systems require chip-scale integration of optical and electrical devices. In order to achieve lower cost and compatibility with mature microelectronics manufacturing, the use of silicon as a fundamental building material for integrated optoelectronics can be traced back to the 1980's [7]. However, silicon-based photonics has several challenges such as poor light emission, low linear electro-optic effect, and high waveguide-propagation loss in the wavelength range of 1.3-1.55 μm. To overcome these limitations, extensive research efforts have been made during the past decades [8] [9] [10].

As an indirect-bandgap semiconductor, silicon is a poor light emitter. While electroluminescence from silicon is still possible, enhanced light emission, caused by quantum confinement effects, has been observed in nano-structured or nano-crystaline silicon [11] [12] [13]. However, their low efficiency makes them far from practical. Recently, the silicon Raman laser using optical pumping was demonstrated [14] [15] and this tech-

nology has been widely viewed as a milestone in the development of silicon-based lasers. However, in the long run, a silicon laser using electrical injection rather than optical pumping is more desirable for chip-scale integration. An alternative scheme involves a hybrid electrically-driven III-V laser on silicon by using wafer bonding or heteroepitaxial growth. The bonding technique has evolved from simple bonding of the whole III-V laser structure onto a silicon wafer [16] to the more state-of-the-art bonding of III-V gain media onto an evanescent-coupled silicon waveguide cavity [17]. The latter is more practical in achieving monolithic integration with other silicon-based guided-wave devices. The direct growth of III-V laser heterostructures on silicon has also been extensively investigated by using a variety of buffer layers such as 2-D strained superlattice [18] [19], graded SiGe buffer layers [20], and quantum dot dislocation filters [21]. However, the reliability of such hybrid electrically-driven devices is still a challenging issue due to incompatibility of III-V semiconductors with Si. The demonstration of an electrically-pumped silicon laser remains a major goal in this field, despite the fact that laser-on-chip is not an ideal architecture due to serious heat dissipation problems [9].

Electrooptical (EO) modulation is indispensable in high-speed systems. Unfortunately, unstrained silicon does not exhibit the Pockels effect — the linear electrooptic effect due to a centro-symmetric crystal structure. The refractive index change induced in silicon by the Kerr effect — the second-order electrooptic effect and the quantum-confined Stark effect (QCSE) are only $\Delta n \sim 2\times10^{-8}$ and $\sim 2\times10^{-5}$, respectively, under a breakdown electric field of 10^5 V/m. Therefore the most common electrooptic effects, such as the Pockels effect in $LiNbO_3$ crystal, Kerr effect in polar liquids including nitrotoluene ($C_7H_7NO_2$) and nitrobenzene ($C_6H_5NO_2$), and the QCSE effect in III-V com-

pound semiconductors, have very low efficiency in silicon. An alternative mechanism of achieving electro-optic modulation in silicon is the so-called free-carrier plasma dispersion effect (FCPDE) [22], which is the linear dependence of refractive index and absorption coefficient on injection carrier density. The FCPDE effect can induce refractive changes of $\Delta n \sim 2\times10^{-3}$ at a wavelength of 1.55 μm with 10^{18} carriers/cm^3. Pioneering work on this approach was done by Soref et al.[22] [24] and then followed by others [25]. Unfortunately, their reported modulator speed is still quite low. Researchers at Intel Corp. recently utilized a metal-oxide-semiconductor (MOS) capacitor to achieve a Mach-Zehnder type modulator with speeds up to 1 Gb/s [26], and soon after demonstrated a higher speed of 10 Gb/s [27]. Another research group extended the above design to achieve a more compact modulator by using a microring resonator instead of a Mach-Zehnder interferometer [28]. On the other hand, strained silicon exhibits significant electroabsorption modulation. It has been reported that efficient electroabsorption modulation can be achieved by using the electrical-field induced delocalization of the electron wavefunction in strained Si/Ge shallow quantum wells [29]. Recently, enhanced QCSE in strained Si/Ge quantum well was observed [30], which could lead to electroabsorption modulators with efficiency comparable to III-V devices.

The propagation loss in silicon arises mainly from the waveguide surface roughness and intrinsic material absorption, where the former is usually dominant [10]. To date, with the development of microfabrication and silicon-on-insulator (SOI) technologies, silicon direct waveguides can exhibit acceptable propagation loss, below 3 dB/cm, in the wavelength range of 1.3-1.55 μm depending on the waveguide dimension and processing conditions [10] [32]. Another loss in waveguides, especially for high-density integration

on a chip, is the radiation loss due to waveguide bending which induces light leakage from guided modes to radiation modes. Compared to glass/polymer waveguides, silicon waveguides have the advantage of much less bending radius due to high refractive-index contrast. Using a modified structure with more material in the inner part of the bend, researchers have demonstrated a 90°-bend with 0.7 μm radius and losses of less than 1% [33]. Alternatively, low-loss bends with a submicrometer radius in photonic-crystal waveguide structures has been demonstrated [34].

While the above developments have been achieved with crystalline Si and SOI technology, hydrogenated amorphous Si (a:Si-H) may offer benefits in terms of lower cost, low temperature processing, as well as other unique characteristics in photonics applications [35]. These include acceptable low loss in the wavelength range of >1 μm due to dangling bonds saturated by H, refractive index and bandgap tunability dependent on H composition, and a desirable thermo-optic effect specifically useful for low-power and low-frequency switching. A Si waveguide/modulator technology realized by plasma-enhanced-chemical-vapor deposition (PECVD), or similar techniques, will introduce flexibility in design and fabrication that is important for the development of silicon photonics. One study has demonstrated a:Si-H waveguides with a propagation loss less than 2.0 dB/cm for 1.55 μm and 5 dB/cm for 1.3 μm [36], comparable to crystalline Si waveguides. The band gap engineering of amorphous silicon quantum dots for light-emitting diodes has also been investigated [37]. Since the a:Si-H thermo-optic modulation has been demonstrated and well characterized, it is believed that SOI-based waveguide thermo-optic modulators with a variety of geometries [38], including Fabry-Parot cavity, microring resonator, and photonic-crystals, can also be achieved with comparable perform-

ance by using a:Si-H waveguides.

1.2. Metamorphic Growth of III-V Semiconductors on Silicon

As discussed above, the metamorphic growth of III-V semiconductors on silicon can lead to a realistic approach of monolithically integrating III-V-based optoelectronic devices with mature silicon CMOS circuits for the realization of optical interconnects. The most difficult challenges in the growth of III-V on Si are the large lattice mismatch (> 4%), large thermo-expansion-coefficient difference, and incompatibility of polar-on-nonpolar materials. Some material properties of Si, GaAs, and InP are listed in Table 1.1.

Table 1.1: Material properties of Si, GaAs, GaSb, GaN, and InP

Properties	Si	GaAs	GaSb	GaN	InP
Crystal symmetry	Diamond	Zinc Blende	Zinc Blende	wurzite	Zinc Blende
Lattice constant (Å)	5.43	5.65 (4%)	6.09 (12%)	3.19(a)/5.189(c)	5.87 (7%)
Therm. Expan. Coeff.(10^{-6} K^{-1})	2.6	5.7	7.75	5.59(a)/3.17(c)	4.60
Therm. Conduct. ($W \cdot cm^{-1} \cdot K^{-1}$)	1.3	0.55	0.32	1.3	0.68
Youngs modulus (GPa)	130	85.9	63.1	181	61.1

** data from "semiconductors on NSM" via http://www.ioffe.rssi.ru/SVA/NSM/Semicond/*

During epitaxial growth of III-V semiconductors on Si, the group III and group V atoms experience randomness in choosing lattice sites due to the nonpolarity of Si. If growth starts with simultaneous nucleation of group III and group V atoms, both species randomly nucleate on different sites and form many small regions. Inside each region there are regular III-V bonds while III-III and V-V bonds form at the boundary between different regions. These small regions are called anti-phase domains (APDs), and the

boundaries are called anti-phase boundaries (APBs). If growth is initiated with alternate exposure to group III and group V atoms, such as migration enhanced epitaxy (MEE), APD-free crystals can be achieved. However, practical growth condition control, initial surface cleanliness, and especially, naturally occurring atomic steps on the silicon surface always make APD-free growth difficult. The odd atomic steps on silicon steps will enhance the formation of APDs, while the even atomic steps will have an opposite effect under MEE growth mode, as shown in Fig. 1.1. III-III bonds serve as acceptors and V-V bonds as donors. Therefore, the epitaxial layer of a III-V semiconductor on silicon contains a high density of highly-compensated doping regions, which can also act as non-radiative recombination centers. To date, the most effective approach to suppress the formation of APDs is utilizing 2-6º mis-oriented (100) silicon substrates which have high-density double atomic steps. Growth is initiated with MEE at low growth rate and low temperature, followed by a higher temperature annealing and subsequent continued growth. A detailed study of epitaxial growth of GaAs and other III-V compound semiconductors on silicon, with device applications, can be found in Ref [39].

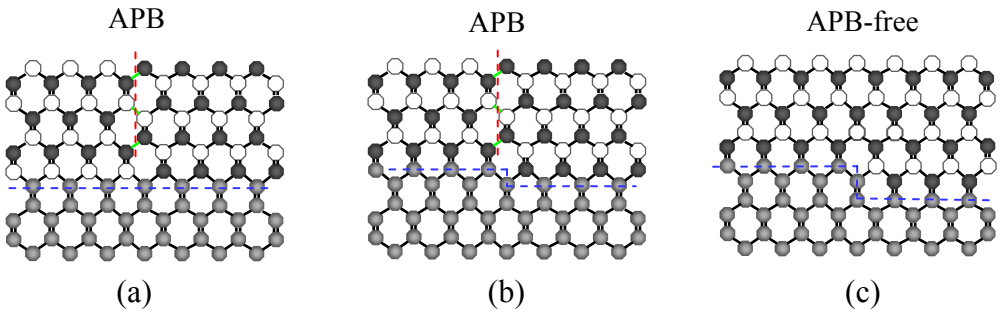

Figure 1.1: Schematic of anti-phase domain (APD) and boundary (APB) formation: (a) on ideal surfaces (no steps) by starting with random nucleation; (b) on single-atomic-step surfaces by starting with MEE; (c) on double-atomic-step surfaces by starting with MEE.

Another serious problem associated with the epitaxial growth of III-V semiconductors on silicon is the generation of a high density of dislocations due to the large difference in lattice constants and thermal expansion coefficients. The built-in strain due to lattice mismatch will create misfit dislocations if the thickness of the epitaxial layer is above a critical value. The typical dislocations in III-V (zinc-blende structure) on silicon are either edge dislocations or 60°-mixed dislocations. The dislocations degrade the epilayer quality and act as non-radiative centers. The dislocations can also climb up from the mismatched interface and propagate into device active regions due to applied stress, current injection, etc. Applied stress can be induced by internal misfit strain, thermal strain, or external mechanical strain. Device-quality III-V epitaxial layers on silicon requires the dislocation density to be smaller than 10^6-10^7 cm^{-2}. In reality, the dislocation density is usually much higher near the III-V-Si interface. A number of dislocation reduction technologies have been proposed and demonstrated, including strained-layer superlattices (SLS)[18] [19] [40] [41], thermal cycle annealing [42], selective area or patterned growth[43] [44], SiGe graded layers [20], AlSb buffer layer [45], and compliant substrates [46]. Based on these technologies, a variety of devices such as lasers (both edge emitting and VCSEL), modulators, photodetectors, solar cells, HBTs, and MESFETs have been achieved. However, despite extensive research efforts and some promising test results on device lifetime, the reliability of these hybrid III-V devices on silicon is still a big concern and bottleneck for practical applications. Dislocation propagation is considered to be the main factor to degrade device performance. In other words, a device-quality epitaxial layer will be degraded due to dislocation glide/climb and the dislocation density in the active region increases with time. For dislocation glide motion under stress,

the motion velocity (V_d) is determined by the applied shear stress (σ_a) and dislocation mobility (μ_d), namely, $V_d=\sigma_a\mu_d$ [47][48]. Here $\mu_d \sim exp\ (-E_d/kT)$, and E_d is the activation energy of dislocation motion, which is dominated by the bond strength. For simplicity, materials with wider bandgap and larger Youngs modulus exhibit slower dislocation motion. A detailed comparison of the dislocation velocity of GaAs, InP, and GaSb on silicon and GaN on sapphire is given in Appendix A, and listed in Table 1.2.

Table 1.2: Comparison of dislocation glide-motion velocity of GaAs, InP, GaSb on Si, and GaN on sapphire at 300K.

Material system	Lattice mismatch	Youngs modulus (GPa)	Band gap (eV)	Poisson ratio (v)	E_d (eV)	τ (GPa)	V_d ($\mu m/Year$)
GaAs/Si	4%	85.9	1.424	0.31	~1.25	2.5	1~5
InP/Si	8%	61.1	1.344	0.36	~1.2	3.8	10
GaSb/Si	12%	63.1	0.726	0.31	~1.2	5.5	15
GaN/Sapphire	16% (30°-rotation)	181	3.2	0.35	~2.1	44.6	1×10^{-13}

1.3.Quantum Dot Lasers: History and Current Trends

An electrically-driven silicon laser currently remains the vital missing piece in silicon photonics. If directly grown III-V lasers on silicon become a practical solution, quantum dots (QD) will provide the opportunity to achieve improved performance of such devices. As an introduction, this section discusses the development history and current trends of QD lasers.

In contrast with conventional atomic lasers, semiconductor lasers have an energy band structure with high density of states (DOS) and carrier-dependent refractive index.

High DOS enables high gain in semiconductor lasers with gain coefficient on the order of magnitude of 10^3 cm^{-1} in near infrared range, while atomic lasers such as HeNe and Nd:YAG have gain coefficient on the order of magnitude of 10^{-3}~10^{-1} cm^{-1}. As a result, a semiconductor laser with small volume (typically 1 mm in length and 10^{-4} mm^2 in cross section area) can emit several watts of CW light. On the other hand, band structure with high DOS enhances carrier interactions and causes problems including spectral broadening and thermal effects which lead to the degradation of laser performance. The dependence of refractive index on carrier injection induces spectral linewidth broadening and lasing wavelength shifting, i.e. frequency chirping, a serious problem for semiconductor lasers. Many applications, from optical communications to pump sources, require semiconductor lasers having low threshold current, high output power and efficiency, large modulation bandwidth, little or no temperature-dependence of the threshold current, and negligible chirp. The goal of semiconductor lasers with low-dimensional heterostructures, including quantum well, quantum wire, and quantum dots in the active region, is to realize the desired performance. In what follows, the basic concept, growth, fabrication and characteristics of quantum dot lasers are reviewed. Sec.1.3.1 introduces optical and electric properties of quantum dots. Sec.1.3.2 addresses the growth of self-organized quantum dots. Sec.1.3.3 discusses the development of self-organized quantum dot lasers and their performance.

1.3.1. Optical and Electric Properties of Quantum Dots

Semiconductor lasers of low-dimensional quantum confined heterostructures as the gain media have higher gain and differential gain due to the increase in DOS. The success

of two-dimensional quantum well lasers [50] [51] inspires interest in lower-dimensional heterostructures, i.e., quantum wires and quantum dots. Figure 1.2 illustrates the energy level of atoms, bulk semiconductors and quantum dots. In bulk semiconductor material, broad energy bands with allowed states, via lattice vibration (phonon), enable the transition/or scattering of carriers in the energy range comparable to the lattice temperature (~ 26 meV at 300 K). The tails of the carrier distribution near the conduction and valence band edges collapse and elongate markedly with temperature. Consequently, the concentration of carriers per unit energy interval near the band edges drops, which decreases gain and degrades laser performance. In addition, hot-carrier effects such as Auger recombination, temperature dependence of the threshold current, and frequency chirp are also direct consequences of the presence of energy bands. In quantum dots, the energy spectra exhibit discrete levels instead of bands. It is similar to the electron energy quantization in atoms. Therefore, quantum dots are referred as artificial atoms. Using a simplified model of the infinite square well (particle in a box), we can estimate the energy quantization $E \sim (\pi\hbar n/L)^2/2m^*$, where n=1, 2, … and m^* is the effective mass of carriers (for example, $m^* \sim 0.063m_e$ for electrons and $m^* \sim 0.51m_e$ for heavy holes in GaAs). Thus, a GaAs-based QD of L ~10 nm can yield an energy separation ΔE ~ 100 meV for electrons and ~10 meV for holes, respectively. The former is much larger than the room-temperature phonon energy of ~26 meV.

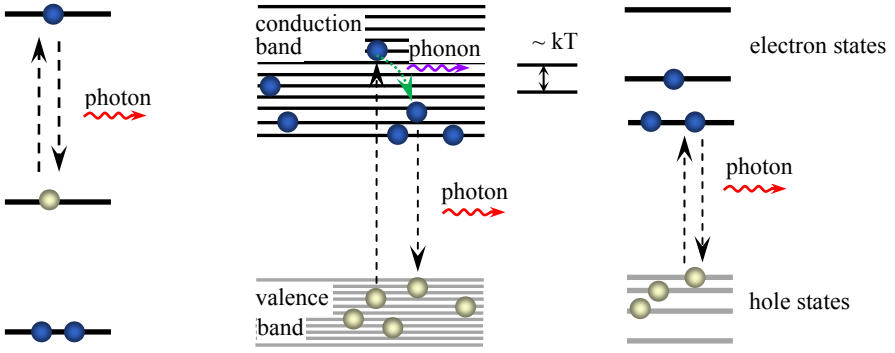

Figure 1.2: Comparison of the energy level of atoms, bulk semiconductors and quantum dots (modified from Ref.[49]).

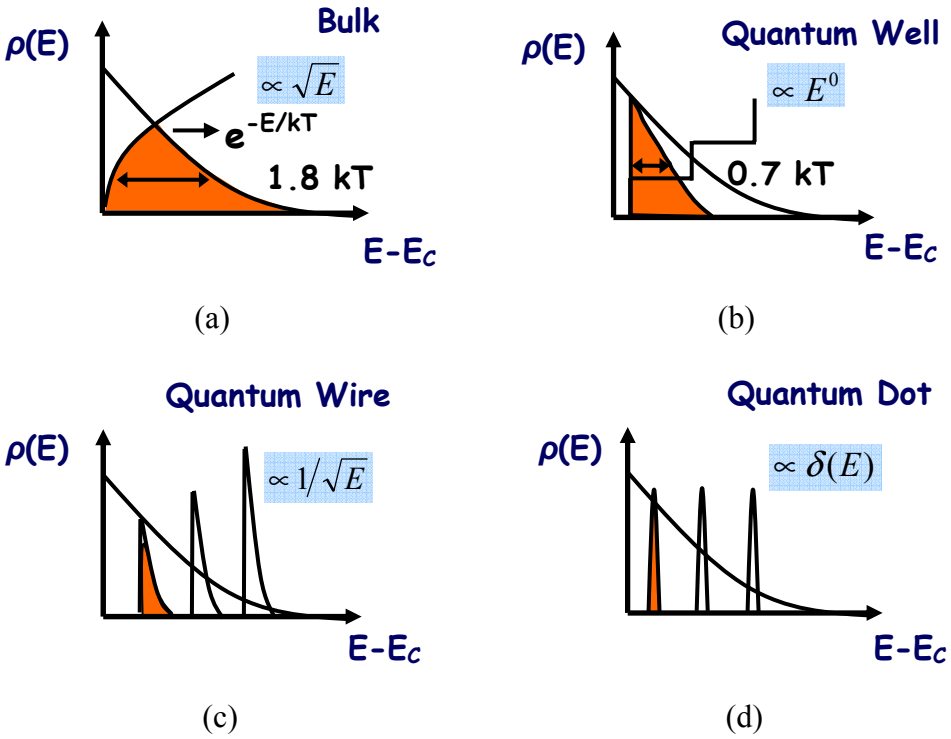

Figure 1.3: Density of states (DOS) and ρ(E) versus energy with respect to the conduction band edge for different dimensional structures: (a) bulk (3-D), (b) quantum well (2-D), (c) quantum wire (1-D), and (d) quantum dot (0-D). The shade areas denote carrier densities with identical quasi-Fermi levels.

As illustrated in Fig.1.3, the DOS would remarkably increase and become less temperature-dependent with dimensionality reduction. QDs provide the most desirable characteristics of atom-like discrete energy levels with delta-function DOS and efficient overlap of electron-hole wavefunctions [52] [53] [54]. These advantages provide QD optoelectronic devices significant performance advantages and unique characteristics:

1) High DOS and efficient overlap of carrier wavefunctions give rise to high gain and high differential gain in QD lasers;
2) Large gain and differential gain enable low threshold current density J_{th} and large output power;
3) Large differential gain also allows higher modulation frequency for extremely high speed operation, low linewidth enhancement factor α, and low/no dynamic chirp;
4) Discrete energy spectrum reduces phonon coupling for high temperature stability;
5) Higher tolerance for defects and radiation due to electron and holes localization;
6) Tunable wavelength of emission and absorption by changing QD size reduces dependence on materials (heterostructure bandgaps).

A detailed discussion on large modulation bandwidth, low chirp, and small α-parameter in QD lasers due to high differential gain is included in Appendix B. The modulation of QD lasers is determined by carrier dynamics in QDs that can be studied with the femtosecond pump-probe differential transmission (DT) spectroscopy [55] [56]. In principle, the differential transmission signal is proportional to the carrier population of the level probed, and therefore reflects the temporal and spectral carrier population. Temperature-dependent DT spectroscopy reveals that the relaxation of electrons from excited states to the ground state takes 5-6 ps at 10 K but >100 ps above 100 K. There exist

mainly two competing processes: electron-hole scattering and phonon bottle effect [57]. Electron-hole scattering gives rise to the fast decay, which is dominant at low temperatures. The carrier scattering rate is strongly temperature dependent and rapidly decreases as the temperature increases due to a marked reduction of the hole population in the ground states by thermal-broadening. On the other hand, the slow decay is governed by the phonon bottleneck, which originates from nongeminate capture of electrons and holes amongst the dots when the number of injected carriers is smaller than the number of accessible dots. The slow decay process enhances with increasing temperature. Additionally, the presence of wetting layer states and barrier states also significantly affects carrier capture and relaxation into QD ground states. It is evident that at room temperature injected electrons preferably occupy excited states in the dots and states in the wetting/barriers layers. The relaxation time of these carriers to the dot ground state is about 100 ps. This leads to large gain compression in QD lasers and limits the attainable small-signal modulation bandwidth to 5-7 GHz. In the same devices small-signal modulation bandwidth up to 30 GHz is observed at cryogenic temperature because the hot carrier distribution is minimized and carriers relax via efficient electron-hole scattering at low temperature [58]. The problem can be alleviated by tunneling "cold" electrons directly into the lasing states of the dots from an adjoining quantum well layer—the "tunneling-injection" [58].

1.3.2. Growth of Self-Organized Quantum Dots

As the superiority of QDs in optoelectronic device applications was recognized in the 1980's [52] [53] [54], extensive research on fabrication and growth of quantum dots, including e-beam lithography, focused-ion-beam (FIB) etching, and self-organized epi-

taxial growth [59] [60] [61], has been carried out. The lithography and etching related techniques suffer from the generation of surface defects. Self-organized epitaxy, on the other hand, enables the coherent growth of defect-free nanostructures and has become the dominant technique to achieve high-quality quantum dots with desirable performance. Depending on the lattice mismatch between the epitaxial layer and substrate, epitaxial growth usually occurs in three modes: Frank-van der Merwe (FM) [62], Stranski-Krastanow (SK) [63], and Volmer-Weber (VW) [64], as shown in Fig. 1.4. FM mode occurs in lattice-matched system with two-dimensional layer-by-layer growth. In the case of large lattice mismatch (>12%), VW mode occurs with three-dimensional (3-D) island growth. SK growth mode occurs in the case of moderate lattice mismatch (>1.8%) starting with a few monolayers of layer-by-layer growth (wetting layer) followed by the formation of 3-D islands (QDs). The driving force for the self-organized 3-D island (QDs) is the elastic relaxation on the island facet edges, minimization of the surface energy of facets and the interaction between neighboring islands via the substrate.

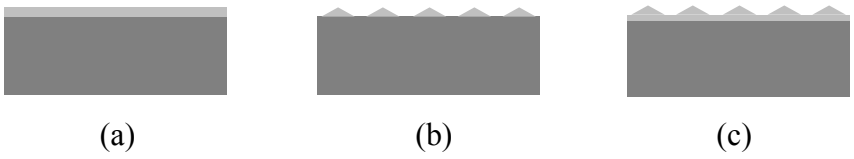

Figure 1.4: Schematic illustration of three epitaxial-growth modes: (a) Frank-van der Merwe (FM), (b) Stranski-Krastanow (SK), and (c) Volmer-Weber (VW).

Typically, the temperature for molecular beam epitaxial (MBE) growth of In(Ga)As-GaAs quantum dots via SK mode is around 460~520 °C. The formation of InAs QDs is initiated at 1.5-1.7 monolayers (ML) and ends at ~2.5-3 ML (~50% overgrowth), while

$In_{0.5}Ga_{0.5}As$ QD starts at 5-6 ML and ends at ~7 ML (10~30% overgrowth). They are next followed by the growth of In(Ga)As capping/barrier. We know multiple layer quantum dots are very useful in QD lasers and photodetectors to enhance the gain and absorption, respectively. If the capping/barrier is thin (usually ~20 Å), the dots in the second layer can be formed exactly on top of the dots in the first layer. This trend continues, resulting in a 3-D array of vertically aligned and electronically coupled dots. Usually, a thinner layer of InGaAs QDs needs to be deposited for subsequent quantum dot layers depending on the GaAs barrier thickness. For example, in the case of InGaAs/GaAs quantum dots, 7 monolayers (ML's) of InGaAs need to be deposited for the first dot layer and subsequent dot layers are formed with 4 ML's of InGaAs. For a thicker barrier layer (≥ 150 Å), the formation of adjacent QD layers are no longer correlated. The QD shape, size and density can be tailored through engineering growth rate, time, temperature, material composition, and substrate orientation. A rule of thumb is that faster rate, lower temperature, and shorter time lead to smaller and higher-density QDs. Table 1.3 lists typical parameters of In(Ga, Al)As/GaAs quantum dots grown in our laboratory.

Table 1.3: Parameters of $In_{0.6}Al_{0.4}As$, $In_{0.5}Ga_{0.5}As$ and InAs quantum dots

Quantum dots	Capping	Photoluminescence wavelength	Dot density	base width	Height
			(cm^{-2})	(nm)	(nm)
$In_{0.6}Al_{0.4}As$	GaAs		$1\sim2\times10^{11}$	9-14	3-4
$In_{0.5}Ga_{0.5}As$	GaAs	1.1 μm	$5\sim6\times10^{10}$	16-22	5-6
InAs	~45Å $In_{0.15}Ga_{0.85}As$	1.3 μm	$2\sim3\times10^{10}$	20-30	7-8

1.3.3. Development of Self-Organized Quantum Dot Lasers and Their Performance

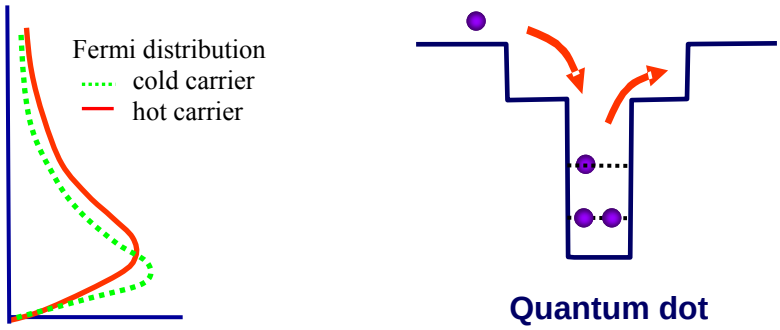

(a)

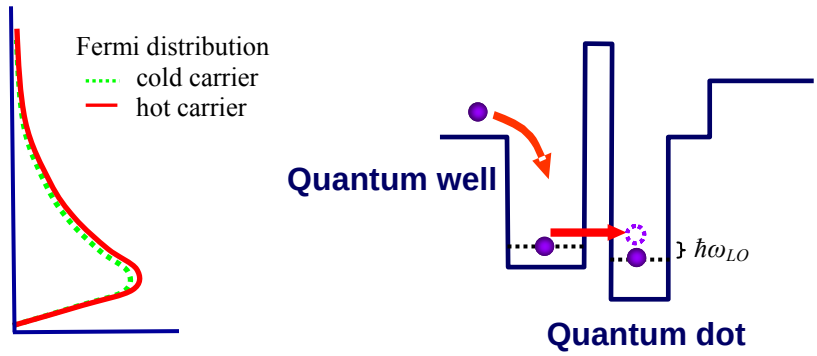

(b)

Figure 1.5: Schematic of a tunneling injection (TI) quantum dot. When cold electrons are introduced into the quantum dot ground states by phonon-assisted tunneling, and the tunneling rate is comparable to the stimulated emission rate, the carrier distribution will be maintained close to a quasi-Fermi distribution even at high injection levels.

The first QD laser was developed in 1994 by using e-beam lithography/etching fabricated QDs [65]. However, its threshold current density of 7.6 KA/cm^2 was quite high even at 77 K due to high-density interface defects surrounding the QDs. Soon after, a self-organized QD laser was reported with lower threshold current density of 120 A/cm^2

at 77 K [66], and was followed by the demonstration of room-temperature operation [67] [68]. A typical InGaAs-GaAs quantum dot laser is basically the same as conventional multi-quantum well separate-confinement heterostructure (SCH) lasers except replacing QWs with QDs. Some tips for the design of typical SCH lasers can be found in Appendix C. The structure consists of an AlGaAs outer cladding, a GaAs inner waveguide, and a single or multiple layers of InGaAs self-organized quantum dots as the active region. Such QD SCH lasers exhibit threshold current density as low as 13 A/cm^2 [69], large differential gain [70] [71], low chirp [72] and reduced linewidth enhancement factor (α-factor) [73]. However, as discussed Sec.1.3.1, QDs have an intrinsic phonon bottleneck, which limits the high-speed operation of lasers. In addition, a relatively small energy-level separation for holes makes lasers susceptible to thermal effects which can degrade gain and induce temperature-dependent operation. The solutions to these problems are introducing tunneling injection (TI) and acceptor (p)-doping technologies to quantum dot laser design and fabrication.

The concept of using tunneling injection in semiconductor lasers to alleviate hot-carrier problem and enhance modulation speed was proposed by Bhattacharya et al. and demonstrated for the first time in quantum well lasers [74]. In a conventional SCH semiconductor laser, carriers injected into quantum well/dots will not only fill the ground state, but also create thermal heating which forces more carriers to stay at higher energy and eventually leak to adjacent layers. Hot carrier effects deform the quasi-Fermi distribution of carriers, and consequently decrease carrier density near the band-edge, induce gain compression and degrade high-speed performance. This problem can be alleviated by tunneling "cold" electrons into the lasing states of quantum-well/dots from an adjacent

injector layer, as shown in Fig. 1.5. The only requirement is that the tunneling rate should be less than/or comparable to the lasing emission rate. DT spectroscopy measurements confirm the tunnel injection time to be <2 ps in TI-QD/QW laser heterostructures with temperature-insensitivity. Enhanced modulation bandwidth, reduced Auger recombination and chirp were demonstrated in TI-quantum well lasers [75] [76]. When TI scheme was used in quantum dot lasers, the most significant improvement is in high-speed performance because TI scheme offered much shorter tunneling time of <2 ps in comparison to the room-temperature carrier relaxation time of 50-100 ps from higher states to ground state. Experiments showed QD TI lasers exhibit small-signal-modulation frequency up to 30GHz, chirp < 0.1 Å, and nearly-zero α-factor, etc.

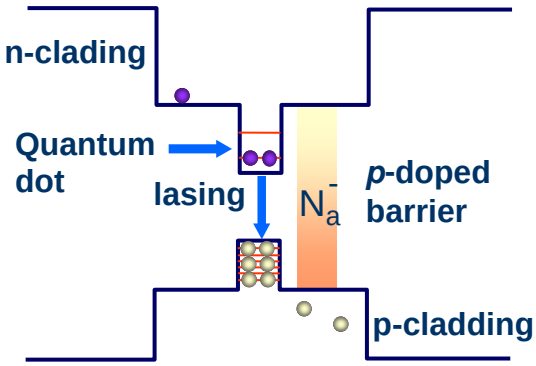

Figure 1.6: Schematic of p-doped quantum dot.

The energy separation of the hole states in QDs is less than the phonon energy, which induces thermal broadening of the hole distribution and temperature-sensitive operation. P-doping of the quantum dots [77] can provide excess holes to fill the ground state at high temperatures as illustrated in Fig. 1.6. Consequently, both the gain and dif-

ferential gain will remain high, and deleterious effects such as gain compression due to hot carriers and carrier leakage associated with the thermal broadening of injected holes are reduced. P-doped QD lasers with remarkably improved performance such as large modulation frequency and high T_0 has been demonstrated [78] [79] [80]. P-doping in QDs is achieved either by direct doping or modulation doping. Considering the relatively-low dot density and the discrete energy levels in QDs, the optimum p-doping levels are ~ 5.0×10^{11} cm^{-2}. The excess holes provided by p-doping can occupy the wetting layer states, which can severely limit the potential benefits of this technique [81]. Additionally, p-doping enhances Auger recombination in QDs [80], which increases the threshold current.

In conclusion, TI and p-doping enable QD lasers with significantly improved performance compared to conventional SCH QD lasers. The current status of self-organized QD lasers with figures of merit is listed in Table 1.4.

Table 1.4: The current status of self-organized QD lasers

Figure of merit	Representative Value	References
J_{th}	13 A/cm^2 (1.2 μm broad-area) 1.4 mA (1.3 μm, single mode)	Eliseev et al., IEEE JSTQE 7, 135 (2001) Livshits et al., Tech. Phys. Lett. 30, 9 (2004)
T_0	232 K (0-80°C, p-doping) 363 K (5-60°C TI) ~∞ (5-65°C, P-doping)	Shchekin et al., Elec. Lett. 38, 712 (2002) Pradhan et al., Elec. Lett. 38, 1449 (2002) Mi et al., APL 86, 153109 (2005)
f_{-3db}	12 GHz (1.3 μm, InGaP cladding) 22 GHz (tunnel injection) 25 GHz (1.1 μm p-doping TI) 11 GHz (1.3 μm p-doping TI)	Kim et al., IEEE PTL 16, 377 (2004) Ghosh et al., APL 81, 305 (2002) Fathpour et al., J.Phys.D 38, 2103 (2005) Mi et al., APL 86, 153109 (2005)
α-factor	0.1-0.7 <0.7 (TI) 0.15 (TI) ~0 (p-doped TI)	Newell et al., IEEE PTL 11, 1527 (1999) Fathpour et al., Elec. Lett. 39, 1443 (2003) Kondratko et al., APL 83, 4818 (2003) Fathpour et al., J. Phys. D 38, 2103 (2005)
Chirp	0.1 Å (1.6μm, 2.5GHz modulation) <0.2 Å (p-doped TI, 1.3 μm, 2-10 GHz modulation)	Saito et al., Elec. Lett. 37, 1293 (2001) Fathpour et al., J. Phys. D 38, 2103 (2005)
λ	0.707 μm (InAlAs dots) 1.45 μm (metamorphic) 2 μm (InP based)	Fafard et al., Science 274, 1350 (1996) Mi et al, APL 89, 153109, (2006) Qiu et al., APL 84, 263 (2004)

1.4. Overview

With the goal of achieving on-chip integration of lasers and guided-wave devices on silicon substrates for optical interconnects, this thesis work represents one of the first attempts to develop InGaAs/GaAs QD lasers directly grown on silicon and their monolithic integration with waveguides and modulators, using MBE metamorphic growth and regrowth, focused-ion-beam milling, plasma-enhanced-chemical-vapor-deposition (PECVD), and silicon membrane transfer technologies. Additionally, as an alternative approach, a novel silicon-based random photonic-crystal microcavity light emitter, which exhibits enhanced spontaneous emission, has also been explored by using PbSe colloidal quantum dots.

High performance quantum dot lasers directly grown on silicon substrates are described in Chapter 2. The use of multiple layers of self-organized InAs/GaAs quantum dots as a three-dimensional (3-D) dislocation filter is proposed, and the effectiveness of this technique is analyzed by a quasi 3-D model of strain-dislocation interaction. The benefits are verified experimentally by cross-section transmission electron microscopy, photoluminescence and characterization of $In_{0.5}Ga_{0.5}As/GaAs$ quantum dot SCH lasers on silicon. These lasers exhibit improved performance with low threshold current density of J_{th}~900 A/cm^2 at 273K, large characteristic temperature (T_0 = 278 K) in the temperature range of 5 to 85 °C and temperature independency of the output slope efficiency (~ 0.4 W/A) in the range of 5 to 50 °C.

Chapter 3 describes the monolithic integration of InGaAs QD lasers with waveguides and quantum well (QW) electroabsorption modulators through MBE growth and regrowth. FIB milling is utilized to create high-quality etched GaAs facets with a reflectiv-

ity of 28% and coupling groove with coupling coefficient greater than 20%. The integrated modulator exhibits a modulation depth ~100% at 5 V reverse bias.

Chapter 4 presents the monolithic integration of quantum dot lasers with amorphous silicon waveguides fabricated by PECVD.

A silicon-based random photonic crystal microcavity light emitter with PbSe colloidal quantum dots is described in Chapter 5. Emission with a minimum linewidth of 4 nm at 1.5 μm wavelength is observed. Such microscale light sources on silicon can also be fabricated or integrated on silicon CMOS chips, which may provide a viable route for inter- and intrachip optical interconnects.

Finally, Chapter 6 concludes this study, and gives suggestions for future work.

CHAPTER 2

HIGH-PERFORMANCE InGaAs/GaAs QUANTUM-DOT LASERS ON SILICON

Compound-semiconductor-based lasers grown directly on silicon substrates will become an important technology option for the realization of on-chip optical interconnects. The performance of GaAs- or InP-based devices on silicon can be degraded by the large density of propagating dislocations resulting from the large lattice mismatch (>4%). The use of multiple layers of self-organized In(Ga,Al)As/GaAs quantum dots as a three-dimensional dislocation filter to impede the propagation of dislocations and reduce dislocation density in GaAs/Si lattice-mismatched heterostructures has been investigated. The effectiveness of this technique and its dependency on quantum dot composition, size, areal density and number of dot layers, has been analyzed with a quasi three-dimensional model of strain-dislocation interaction. It is found that 10 layers of InAs quantum dots of size ~20-30 nm constitute the most effective dislocation filter. This has been verified experimentally by cross-section transmission electron microscopy, photoluminescence and performance characterization of $In_{0.5}Ga_{0.5}As$/GaAs quantum dot separate confinement heterostructure lasers on Si. The lasers exhibit J_{th}~900 A/cm^2 at 273K, large characteristic temperature (T_0 = 278 K) in the temperature range of 5–85 °C and their output slope efficiency (~ 0.4 W/A) is independent of temperature in the range of 5 to 50 °C.

2.1. Introduction

Most optical components such as waveguides and modulators have been achieved using silicon, but the silicon laser is the final frontier. Schemes for optically-pumped silicon lasers with Raman amplification [14] [15] and nanostructures [13] have been demonstrated, but the realization of an electrically injected laser on silicon is still elusive. The directly-grown III-V compound-semiconductor laser on silicon is one of promising approaches. However, III-V compound semiconductors have a large lattice mismatch with silicon (> 4%). Additionally, the epitaxial growth of polar material on a non-polar substrate is a challenge. Due to the large lattice mismatch, high-density misfit dislocations are formed at the substrate-epitaxial layer interface. These defects eventually propagate upward and into the active regions as growth proceeds. Various devices have been demonstrated with such *metamorphic* layers in heterostructure systems, by using different dislocation reduction techniques such as strained-layer superlattices (SLS)[40] [41], thermal cycle annealing [42], selective area or patterned growth[43] [44], SiGe graded layers [20], AlSb buffer layer [45], and compliant substrates [46], and selective evaporation of dislocated region [82].

In principle, a strained layer is capable of bending the propagation of dislocations [83]. Such bending increases the chance of annihilation of the threading dislocation, or their transport to the sample edge, therefore resulting in a reduction of the dislocation density [84]. Strain-driven self-organized quantum dots [59] [60] [61], formed in the Stranski-Krastanow growth mode, have been very successfully incorporated in the active region of devices such as lasers, amplifiers, infrared detectors, and single photon sources. The strain field surrounding the three-dimensional islands is much larger than that pro-

duced by two-dimensional strained layer superlattices. Consequently, dislocations propagating near and under the islands will experience stronger Peach-Koehler forces [85], and are expected to be bent more easily. Reduction in defect density due to the presence of quantum dots in the GaN material system has been observed and investigated experimentally using etching techniques [86]. However, the mechanism of dislocation filtering by the islands has not been elucidated and its effectiveness has not yet been demonstrated in real devices.

The performance characteristics of InGaAs/GaAs quantum dot lasers grown directly on silicon without any special dislocation filtering was previously reported by us [87]. In the present research, multiple layers of In(Ga, Al)As/GaAs self-organized quantum dots as a dislocation filter, in the growth of GaAs-based InGaAs QD lasers on silicon substrates, has been proposed and studied in detail. The QD composition, size, areal density and the number of dot layers were optimized with a quasi three-dimensional model based on the strain relaxation in mismatched heterostructures. Dislocation bending was confirmed by cross-sectional transmission electron microscopy (XTEM) and the effectiveness of the QD dislocation filters was confirmed by photoluminescence (PL) and performance characterization of the lasers on silicon. The lasers demonstrated substantially improved luminescence and vastly reduced threshold currents. Their dynamic characteristics were also comparable to those of QD lasers on GaAs. In what follows, the effectiveness of dislocation bending is theoretically calculated in Sec 2.2. The experiments, including epitaxial growth of the QD laser heterostructures with multiple-layer QD dislocation filters, and their characterization by cross-sectional transmission electron microscopy

(XTEM), photoluminescence and performance characteristics are described in Sec.2.3. Finally, conclusions are made in Sec.2.4.

2.2. Quantum Dot Dislocation Filters: Modeling

From energy minimization considerations in a unit cell of the growing layer, it can be shown that for misfits ~2%, the island mode of growth is preferred [59]. Elastic relaxation on the facet edges, renormalization of the surface energy of the facets and interaction between neighboring islands via the substrate are the driving forces for self-organized growth. In general, the islands are coherently strained and dislocation-free, but can be partly relaxed. If the islands continue to grow, coherent growth degrades to incoherent growth beyond a critical size, with the generation of misfit dislocations. In our model and experiment we have considered coherently strained islands smaller than the critical size.

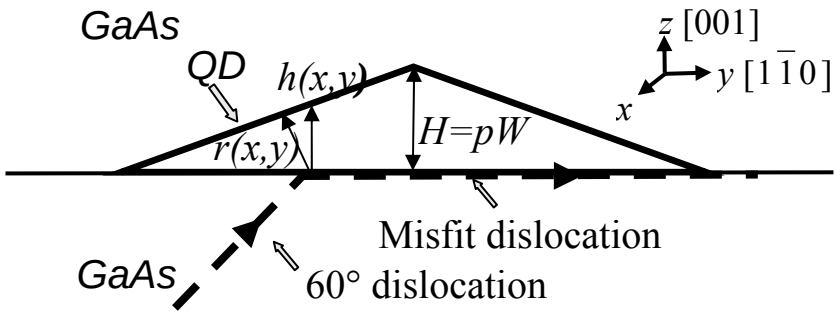

Figure 2.1: Cross-sectional schematic description of the bending of a 60° dislocation by a quantum dot.

As shown schematically in Fig. 2.1, we assume that the self-organized islands are pyramidal in shape and that a dislocation generated at the lattice mismatched interface propagates towards the base of the island. The bending of this dislocation will generate a segment of misfit dislocation, which glides below the island. Bending will occur when the strain energy released due to the generation of the misfit dislocation, ΔE_{rel}, is equal to or greater than the dislocation self energy, ΔE_{dis} [88] [89], where ΔE_{rel} and ΔE_{dis} are described by:

$$\frac{\Delta E_{rel}}{L} = \frac{2G_{dot}(1+\nu)}{(1-\nu)} f_{eff} b_{eff} h \,, \tag{2-1}$$

$$\frac{\Delta E_{dis}}{L} = \frac{1}{2\pi} \frac{G_{buff} G_{dot}}{G_{buff} + G_{dot}} b^2 \left(\frac{1-\nu\cos^2\beta}{1-\nu} \right) \left[\ln\left(\frac{2r}{b} \right) + 1 \right]. \tag{2-2}$$

Here, L is the length of the misfit dislocation, G_{dot} (G_{buff}) is the shear modulus of dots (buffer layer), ν is the Poisson ratio ($\cong 0.3$ for GaAs and related alloys), b_{eff} is the Burger's vector component parallel to dot-buffer layer interface, and $h(x)$ is the quantum dot height as a function of x. β is the angle between the Burgers vector and the dislocation line. $r(x)$ represents an outer cut-off radius of the dislocation strain field, which is usually assessed either by the distance to the nearest free space or by the averaged mutual half dislocation distance. $f_{eff} = f\sqrt{1-\exp(-\kappa/p)}$ is the effective lattice mismatch between the quantum dot and the underlying buffer layer (where $\kappa \cong 0.09$ from the simulation of three dimensional strain-fields with the valence force field model [90]). We assume that

the pyramidal quantum dot has a base width W and height $H=pW$, where p is a geometrical factor. L is assumed to be comparable to W.

Calculations were done for InAs, $In_{0.5}Ga_{0.5}As$ and $In_{0.6}Al_{0.4}As$ quantum dots on GaAs buffer layers. The properties of the different materials used in the calculations are listed in Table 1. From the XTEM data, to be shown later, it is evident that pure misfit dislocations with line vector $\vec{l} = [1\,\bar{1}\,0]/\sqrt{2}$ and Burgers vector $a/2[101]$ are produced when dislocation bending takes place. Using Eqs. (2-1) and (2-2), we calculate the bending area underlying the quantum dot within which a propagating dislocation can be bent, i.e., when $\Delta E_{rel} \geq \Delta E_{dis}$. Table 2 lists the bending area ratio for the three types of quantum dots, together with the actual sizes and density of these dots when grown under optimal conditions of temperature and growth rate by molecular beam epitaxy (MBE). Here, the bending area ratio of a single quantum dot is defined as the bending area divided by the area of the quantum dot base. Consequently, the bending area ratio of a single layer is obtained by taking into account the quantum dot density. The results are also plotted in Fig. 2.2. It is apparent that larger dots with a higher dot density are the most suitable as dislocation filters.

Table 2.1: Material properties of $In_{0.5}Ga_{0.5}As$, $In_{0.6}Al_{0.4}As$ and InAs

Parameter	GaAs	$In_{0.5}Ga_{0.5}As$	$In_{0.6}Al_{0.4}As$	InAs
a (Å)	5.653	5.856	5.896	6.058
f (%)	0	3.47	4.12	6.69
G (GPa)	48.62	39.93	37.94	31.24

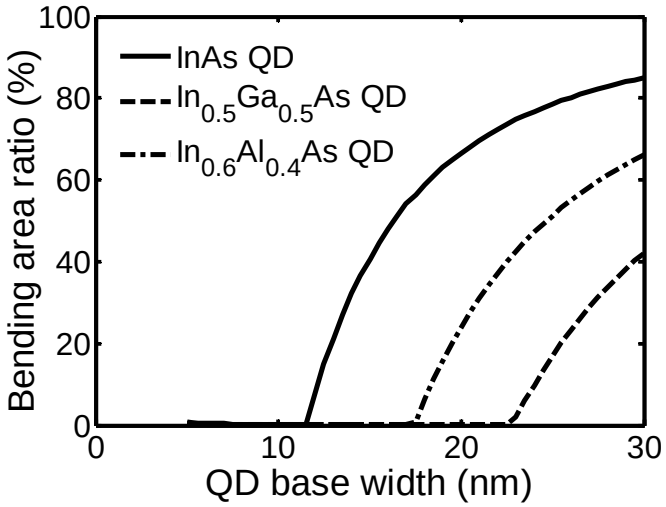

Figure 2.2: Bending area ratio versus quantum dot base width for InAs, $In_{0.5}Ga_{0.5}As$, and $In_{0.6}Al_{0.4}As$ dots.

Table 2.2: Bending area ratio of $In_{0.6}Al_{0.4}As$, $In_{0.5}Ga_{0.5}As$ and InAs quantum dots

Quantum dots	Dot density	Size	Height	*p*	Bending area ratio of a single QD	Bending area ratio of a single layer
	(cm^{-2})	(nm)	(nm)			
$In_{0.6}Al_{0.4}As$	$2x10^{11}$	9-14	3-4	1/3	~0	~0
$In_{0.5}Ga_{0.5}As$	$5x10^{10}$	16-22	5-6	1/ 3.5	<1%	~0
InAs	$2x10^{10}$	20-30	6-7	1/ 4	80%	10%

As in the case of the multiple strained-layer superlattice, it is expected that a multiple quantum dot layer stack will be a more efficient dislocation filter and will enhance the bending of propagating dislocations. However, the cumulative strain can become excessive for a large number of dot layers, in which case it will be released by generating single-kink and double-kink misfit dislocation loops. The former depends on the depth of the buried dot layers and will preferentially occur first due to a lower energy barrier. Using the excess stress model developed by Tsao and Dodson [91], one can estimate the

critical number of quantum dot layers before single-kink dislocations are generated. Accordingly, the maximum number of dot layers that can be grown is given by [91]:

$$2G_{dot}\left(\frac{1+\nu}{1-\nu}\right)\varepsilon_{eq}(z)-\frac{b}{2\pi z\cos\beta}\frac{G_{buff}G_{dot}}{G_{buff}+G_{dot}}\left(\frac{1-\nu\cos^2\beta}{1-\nu}\right)\left[\ln\left(\frac{4z}{b}\right)\right]\geq 0, \qquad (2\text{-}3)$$

where

$$\varepsilon_{eq}(z)=\int_0^z f_{avg}\frac{dz'}{z}=f_{avg}h/(h+h_s) \qquad (2\text{-}4)$$

is the accumulated strain. Here, z is the thickness of multiple QD layers, $h=H/3$ is the effective height of pyramidal-shaped QD, and h_s is the thickness of GaAs spacer layers. In calculating the accumulated strain, for simplicity, the quantum dot is assumed equivalent to a two-dimensional uniformly strained layer with thickness of $h=H/3$ and equal strain energy per area. The parameter f_{avg} is defined as the average misfit between the GaAs barrier layer and the quantum dot layer. Since the strain energy per unit area of quantum dot layer is

$$E_{ela}=2G_{dot}f_{eff}^2\frac{(1+\nu)}{(1-\nu)}\left(\rho_{dot}\int_{dot}dV\right)\Big/h, \qquad (2\text{-}5)$$

while the coherent strain energy of a uniformly strained film is $E_{ela}=2G_{dot}(1+\nu)/(1-\nu)f_{avg}^2$, one can express the average misfit f_{avg} as

$$f_{avg}=W\rho_{dot}^{1/2}f\left(1-\exp(-\kappa/p)\right)^{1/2}, \qquad (2\text{-}6)$$

where ρ_{dot} is the areal dot density.

The calculations show that the critical layer number depending on real dot size are 10~15 for InAs dots, 20~30 for $In_{0.5}Ga_{0.5}As$ dots and 15~35 for $In_{0.6}Al_{0.4}As$ dots, respectively, with 50nm GaAs barrier layers in between [see Fig. 2.3].

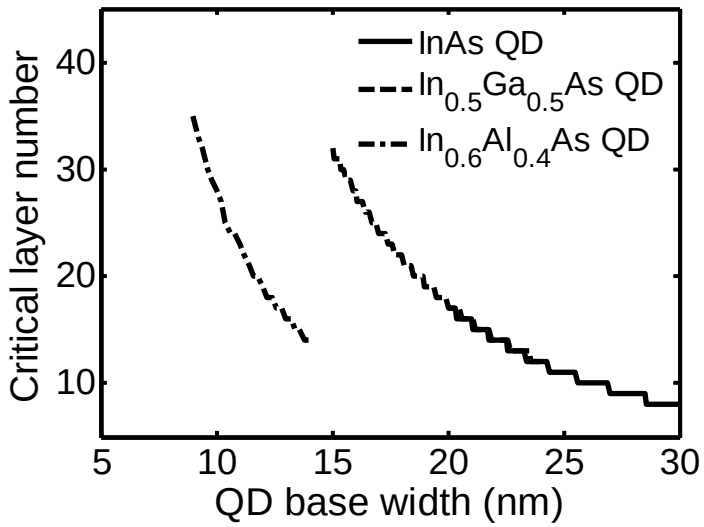

Figure 2.3: Calculated critical layer number corresponding to single-kink dislocation loop for InAs, $In_{0.5}Ga_{0.5}As$ and $In_{0.6}Al_{0.4}As$ quantum dot multilayers.

2.3. Experiments

2.3.1. Molecular Beam Epitaxial Growth and Device Fabrication

The laser heterostructure, shown in Fig. 2.4, was grown on (001)-oriented Si substrates misoriented 4° toward <111>. A thin (≤2 μm) GaAs buffer layer is first grown by metal-organic vapor phase epitaxy (MOVPE). This layer is almost free of anti-phase domains and the dislocation density at its surface is estimated to be $(2\text{-}5)\times10^7$ cm^{-2}. The GaAs/AlGaAs/$In_{0.5}Ga_{0.5}As$ QD separate confinement heterostructure laser, with or without p-doping of the quantum dots and incorporating InAs, $In_{0.5}Ga_{0.5}As$ or $In_{0.6}Al_{0.4}As$ quantum dot buffer layers for dislocation filtering is grown by MBE. It has been established that p-doping of the active quantum dots improves the gain and differential gain and reduces the temperature dependence of quantum dot lasers [78][79][80]. The active region quantum dot layers, the GaAs layers and the $Al_{0.7}Ga_{0.3}As$ layers were grown at

500 °C, 580 °C and 620 °C, respectively. P- and n-type doping were accomplished with Be and Si, respectively. The dislocation filter is made up of 10 quantum dot layers separated by 500 Å GaAs layers. The growth rate was maintained at 2 Å/s throughout the laser heterostructure. For comparison purposes, identical laser heterostructures were also grown on Si and (001) GaAs substrates without the QD buffer layer. The growth conditions for the QD buffer layers are listed in Table 2.3. In both InGaAs quantum dot active layers and quantum dot buffer layers, the GaAs spacer layers are grown at 580 °C. This high-temperature spacer layer can minimize the generation of dislocations in quantum dot layers [87][92]. Some tips for the design of typical SCH lasers can be found in Appendix C.

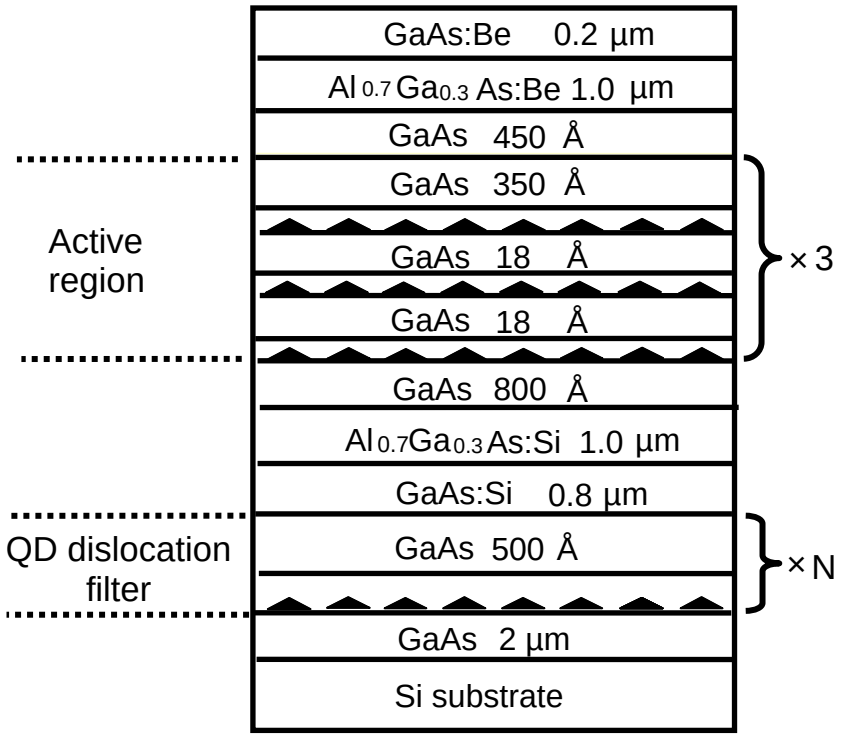

Figure 2.4: Schematic of self-organized $In_{0.5}Ga_{0.5}As$ quantum dot laser heterostructures grown on Si substrates with the dislocation filter consisting of N quantum dot layers (N=0, 5, 10 and 15).

Table 2.3: Quantum dot lasers on Si with different growth conditions and structures

Laser	InAs QD buffer	Active region
1	w/o	SCH
2	10-layers, grown @460°C	SCH
3	10-layers, grown @510°C	SCH
4	15-layers, grown @510°C	SCH
5	10-layers, grown @510°C	SCH with p-doping

2.3.2. Cross-Sectional Transmission Electron Microscopy (XTEM)

Transmission electron microscopy (TEM) could be the most convincing evidence to investigate the effectiveness of dislocation filters. XTEM measurements were made to study the propagation of dislocations in the 10-layer InAs QD buffer region of the laser heterostructure on Si. Images of dislocations were recorded under various diffraction conditions along the (110) axis, specifically for g = $(2\bar{2}0)$, $(1\bar{1}1)$, $(\bar{1}11)$, (004), and $(1\bar{1}3)$ (see Fig. 2.5). According to the $\mathbf{g}\cdot\mathbf{b}=0$ invisibility criterion (see Table 2.4), GaAs/Si heteroepitaxy generally creates two types of threading dislocations: pure edge dislocations with Burger's vector $\mathbf{b}=\pm(\bar{1}10)$ (labeled as C in Fig. 2.5) and 60° mixed dislocations with $\mathbf{b}=\pm(01\bar{1})$ or $\pm(101)$ (labeled as A and B in Fig. 2.5). It is apparent that InAs QD buffer layers can efficiently bend 60° mixed dislocations (labeled as B). More significantly, pure-edge dislocations (labeled as C), which cannot be blocked by SLS due to zero shear force [84], can terminate at the surface of QDs. This is probably because of either the formation of a dislocation loop at the QD surface due to stronger and anisotropic stress surrounding the nano-island, or the formation of a dislocation of reverse Bur-

ger's vector which annihilates the preexisting dislocation. The detailed termination mechanism is not yet well understood. In addition, point defects with tensile (compressive) strain tend to be trapped in a localized compressive (tensile) strain region beneath the quantum dot due to minimization of the local strain energy. This also improves the quality of subsequent epitaxial layers.

Table 2.4: Dislocation type and g·b value

g \ b	110	$\bar{1}10$	011	$01\bar{1}$	101	$10\bar{1}$
$\bar{1}11$	0	1	1	0	0	-1
004	0	0	1	-1	1	-1
$1\bar{1}3$	0	-1	1	-1	1	-1
$1\bar{1}1$	0	-1	0	-1	1	0
$33\bar{1}$	0	-1	-1	-1	1	1
$2\bar{2}0$	0	-1	-1	-1	1	1

Note: Dislocation A and B with b=±$(01\bar{1})$ or ±(101) are mixed dislocation; Dislocation C with b=±$(\bar{1}10)$ is edge dislocation.

The significant suppress of dislocation propagation by the QD dislocation filters and GaAs buffer can be clearly shown in the XTEM image of dislocations near the GaAs-Si interface and the active region, as shown in Fig. 2.6.

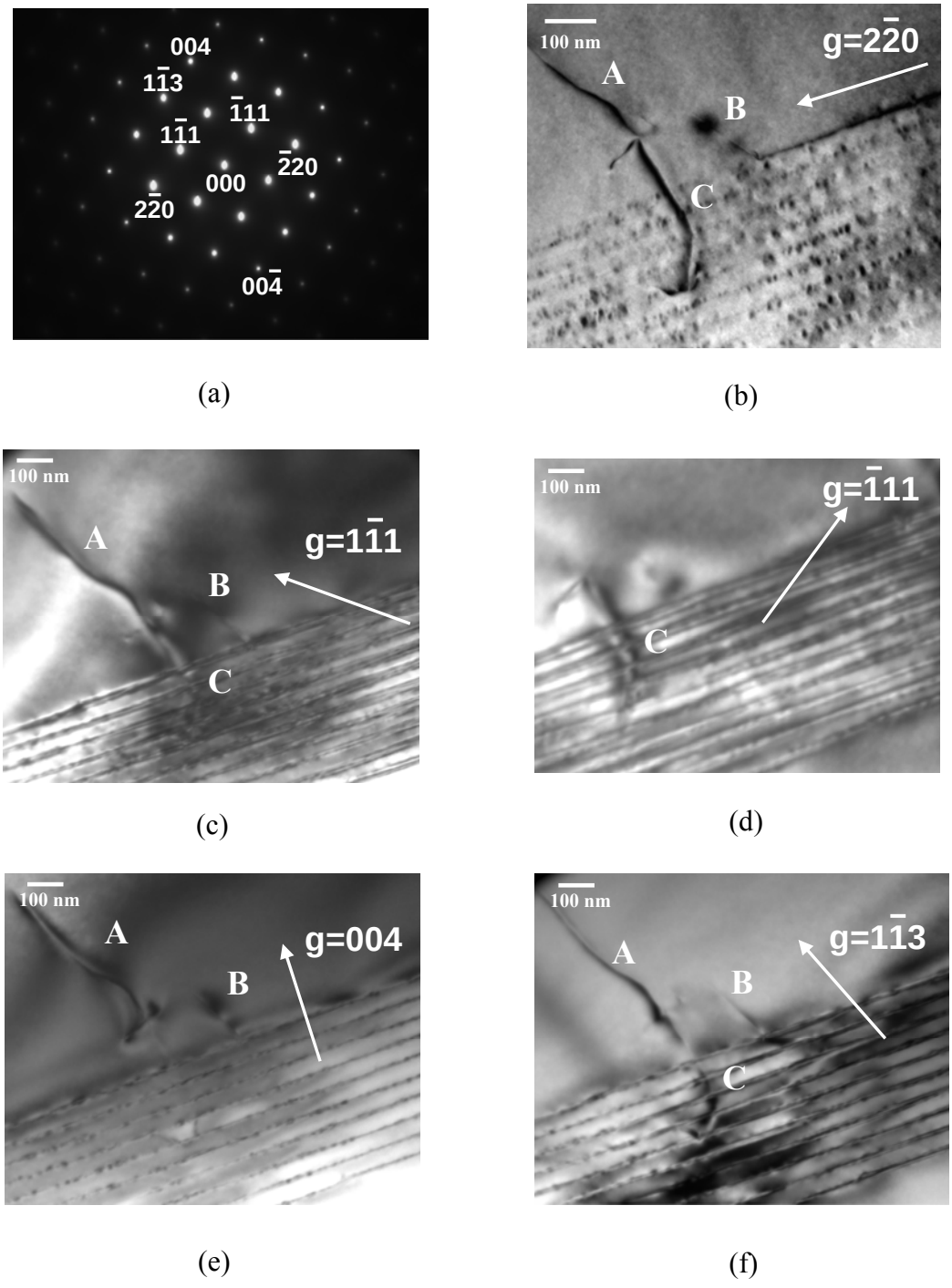

Figure 2.5: Electron diffraction pattern (a), and cross-sectional transmission electron microscopy image of dislocation propagation in the 10-layer InAs quantum dots buffer layer with various diffraction conditions: (b) g=$(2\bar{2}0)$, (c) g=$(1\bar{1}1)$, (d) g=$(\bar{1}11)$, (e) g=(004) and (f) g=$(1\bar{1}3)$. The zone axis is (110).

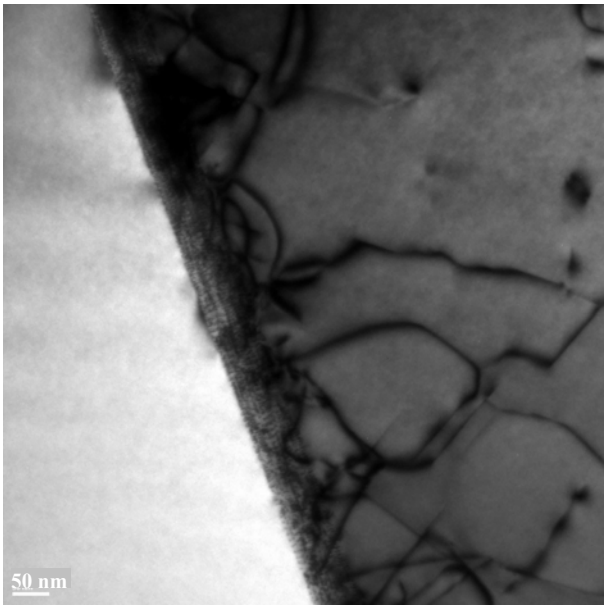

(a)

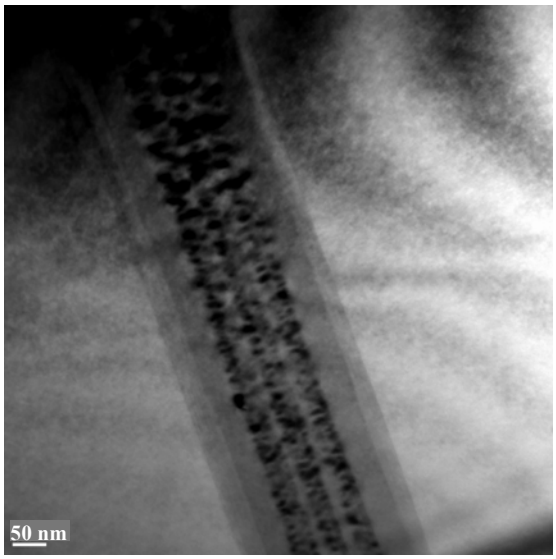

(b)

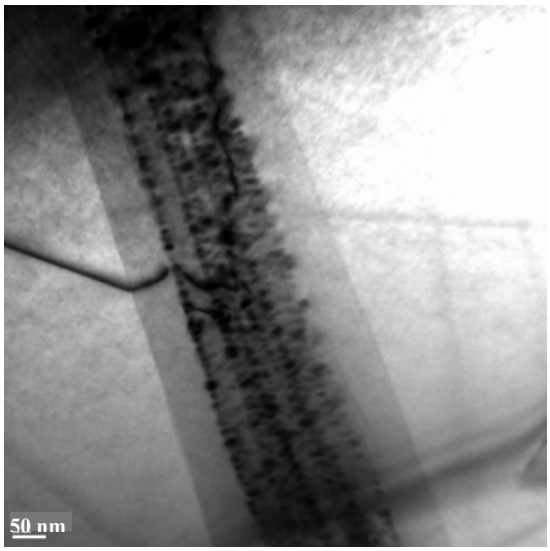

(c)

Figure 2.6: Cross-sectional transmission electron microscopy image of dislocation near the GaAs-Si interface (a), and the active region (b) and (c).

2.3.3. Photoluminescence Spectra

Room temperature photoluminescence from the laser active region quantum dots was measured in a small piece of the grown wafers in which the top GaAs p-contact layer and most p-cladding were removed by wet etching. Photoluminescence spectra were recorded with an argon ion laser, a 0.75 m scanning spectrometer and a liquid nitrogen cooled Ge photodiode.

Figure 2.7(a) depicts room temperature photoluminescence (PL) spectra from the active $In_{0.5}Ga_{0.5}As$ QDs in laser heterostructures grown on Si with 10 layers of InAs, $In_{0.5}Ga_{0.5}As$ and $In_{0.6}Al_{0.4}As$ quantum dots as the dislocation filters. The highest luminescence intensity is observed in the sample with the InAs quantum dot buffer layer. The linewidth (full width at half maximum) is 60 meV, which is comparable to that measured in laser heterostructures grown on GaAs substrates. Figure 2.7(b) compares the PLs measured in QD laser heterostructures grown on GaAs and Si substrates, and on Si with a buffer layer consisting of 10 InAs QD layers. There is a difference of only a factor of 2 in the peak PL intensity of the heterostructures grown on GaAs and that on Si with InAs QD buffer layer. Figure 2.7(c) shows the optimum PL spectra obtained from a heterostructure grown on Si, with 10 QD layers of InAs as the buffer with these QDs grown at a higher temperature of 510 °C. In addition to PL from the active $In_{0.5}Ga_{0.5}As$ QDs, PL from the InAs QD buffer layer is also clearly observed, in spite of the defects around this layer. It is evident that InAs QDs are most effective in improving the luminescent properties of the active quantum dot region, suggesting that they might bend propagating dislocations more efficiently, because of their large size and higher strain. We next examine the effect of varying the number of InAs QD layers in the buffer region. The PL data is also shown

in Fig. 2.7(c). It appears that 10 QD layers are optimum. These results are in agreement with the calculated results presented earlier.

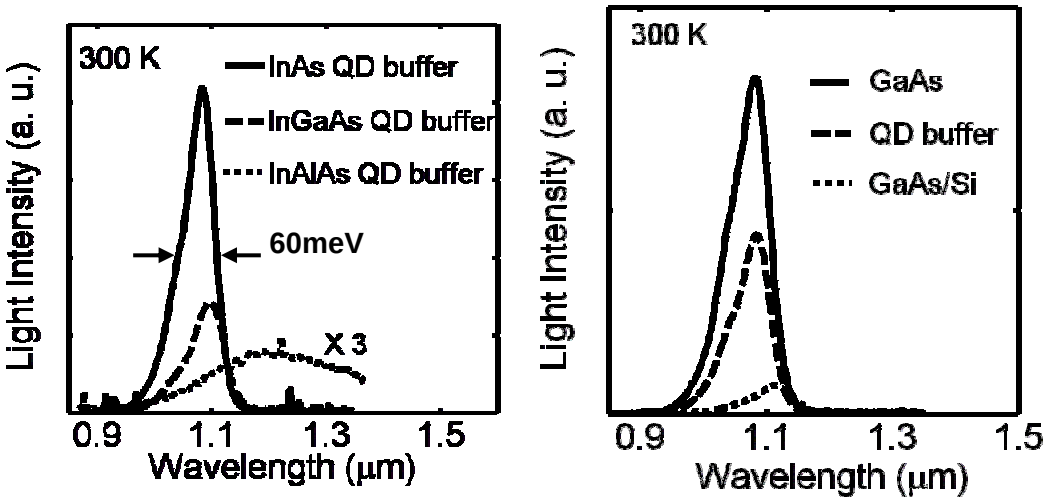

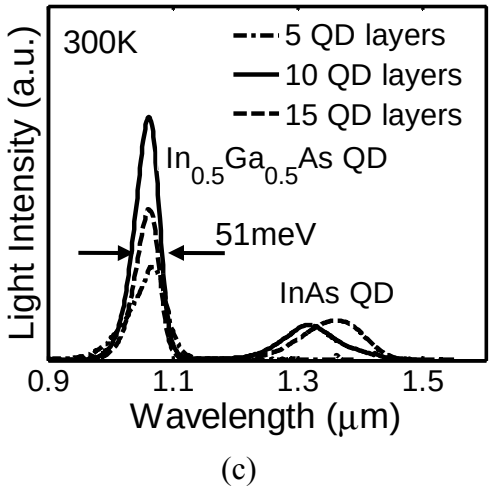

Figure 2.7: Photoluminescence spectra measured at 300 K from $In_{0.5}Ga_{0.5}As$ quantum dots grown on Si: (a) with different quantum dot buffer layers grown at 460°C; (b) with and without InAs quantum dot buffer layers, and on GaAs; and (c) by using 5, 10 and 15-layer InAs quantum dots in the buffer layer grown at 510°C.

2.3.4. Laser Characteristics

Both broad area and ridge waveguide lasers were fabricated by standard photolithography, wet and dry etching and contact metallization techniques. Finally, the laser wafers were lapped down to ~80 μm for cleaving along the (110) direction.

The characteristics of $In_{0.5}Ga_{0.5}As$/GaAs QD lasers on Si substrate, with and without a dislocation filter consisting of multiple quantum dot layers, are next described. Only the lasers with InAs QD buffer layers have been characterized, since it is evident that InAlAs or InGaAs QD buffer layers do not yield the highest PL intensity from the active $In_{0.5}Ga_{0.5}As$ QDs. Our objective is to confirm the optimal number of QD layers in the dislocation filters that yields the best laser performance. The description of the different lasers is listed in Table 2.3.

The light-current (L-I) characteristics of laser 1, without any QD buffer but implementation with similar thickness GaAs, shows the threshold current density greater than 1500 A/cm^2. The threshold current density of laser 2, by using 10-layer InAs QDs grown on 460 °C, decreases to 1100 A/cm^2 [shown in Fig. 2.8(a)]. The measured threshold current densities of lasers 3 and 4, with 10 and 15 InAs QD layers in the buffer, are shown in Fig. 2.8(b). There is an increase in threshold current beyond 10 QD layers in the buffer, in agreement with calculated results. The lowest threshold current density of 900 A/cm^2 is measured in laser 3, in which the 10-layer QD buffer is grown at 510 °C to enhance the dot size. The temperature dependence of the threshold current and the slope efficiency of laser 1(no QD buffer) and laser 5 (10 QD layer buffer and p-doping of dots) are shown in Figs. 2.9(a) and (b), respectively. The temperature dependence of J_{th} is characterized by the empirical equation $J_{th}(T) = J_{th}(0)\exp(T/T_0)$. As expected, p-doping increases T_0,

but also increase the threshold current because of increased Auger recombination [80]. On the other hand, T_0 is extremely high in the temperature range of 5–85 °C and the output slope efficiency (~ 0.4 W/A) is independent of temperature in the range of 5–50 °C. These are extremely desirable attributes for practical applications.

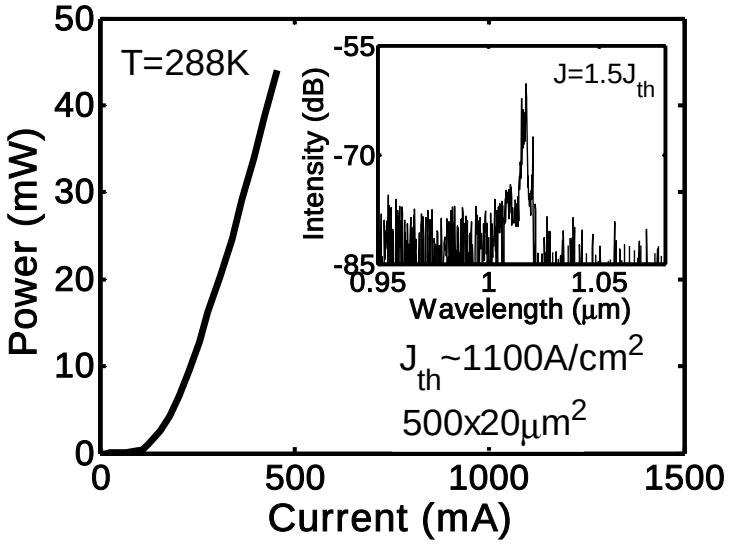

(a)

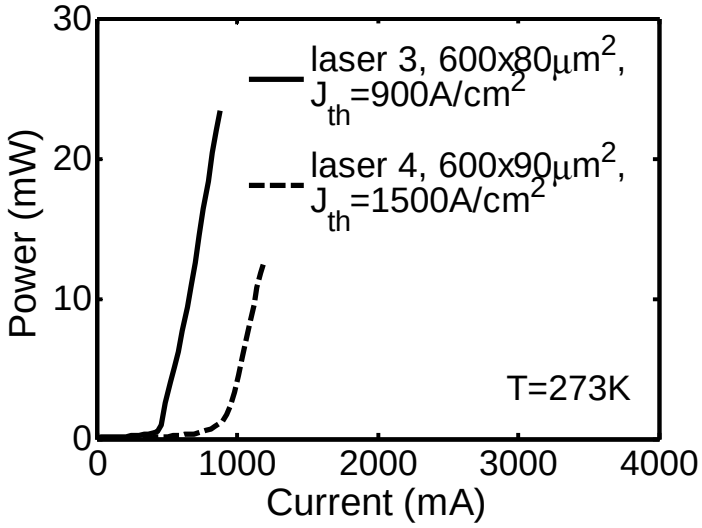

(b)

Figure 2.8: Light-current characteristics under pulsed mode (1% duty cycle of 100 μs) of: (a) laser 2 (spectrum in inset), and (b) lasers 3 and 4.

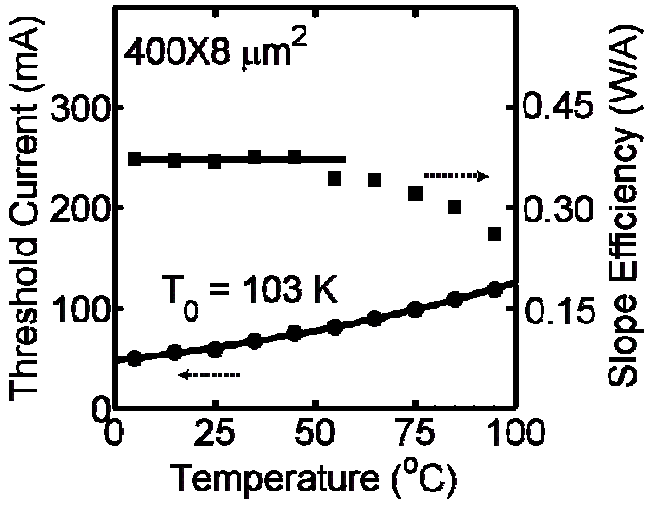

(a)

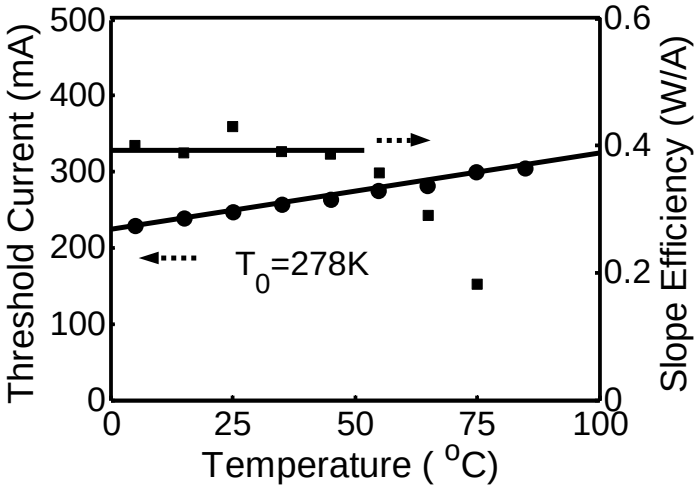

(b)

Figure 2.9: Threshold current and slope efficiency versus temperature under pulsed mode (1% duty cycle of 100 μs) of: (a) laser 1 and (b) laser 5.

2.4. Conclusion

In conclusion, we have demonstrated that multiple layers of self-organized quantum dots can act as an effective dislocation filter at the Si/GaAs interface and can substantially improve the performance characteristics of GaAs-based In(Ga)As QD lasers. Results obtained from analysis with a quasi three-dimensional model of strain-dislocation interaction and from measured characteristics of $In_{0.5}Ga_{0.5}As$/GaAs quantum dot lasers grown on the GaAs/Si interface with In(Ga,Al)As/GaAs quantum dot dislocation filters confirmed the effectiveness of this technique. It is possible that similar quantum dot dislocation filters will be equally effective in the growth of devices on other mismatched heterostructure systems such as the wide-bandgap nitrides on sapphire and the narrow gap HgCdTe on silicon. The technique of using quantum dots to block or terminate dislocation propagation could be extended to other self-organized nanostructures. For example, nanovoids [93], formed in-situ during the quantum dot overgrowth process, may serve as efficient terminators of dislocations.

CHAPTER 3

MONOLITHIC INTEGRATION OF GaAs-BASED LASERS AND MODULATORS ON SILICON SUBSTRATES

Monolithic integration of the GaAs-based laser, waveguide, and electroabsorption modulator on silicon has been demonstrated with InGaAs/GaAs quantum dot and quantum well heterostructures directly grown on silicon by molecular beam epitaxy growth and regrowth. Focused-ion-beam etching is utilized to form high quality laser mirrors for feedback and grooves for coupling as well as electrical isolation. Based on a transmission matrix and generalized beam propagation approach in terms of intensity moments and Gouy phase shifts, a self-consistent model has been developed to estimate the reflectivity and coupling coefficient of etched grooves and optimize these parameters for real devices. High quality focused-ion-beam etched facets with a reflectivity R~0.28 and efficient coupling with coupling coefficients up to 30% for well-defined grooves have been achieved. Moreover, monolithic integration of an $In_{0.5}Ga_{0.5}As$/GaAs quantum dot laser and an $In_{0.2}Ga_{0.8}As$/GaAs quantum well electroabsorption modulator on silicon has been demonstrated for the first time. The laser-modulator coupling coefficient is larger than 20% and the depth of modulation is 45% and 100% at 3V and 5V reverse bias, respectively.

3.1. Introduction

To achieve information switching and transmission in optoelectronic integrated circuits on silicon, it is important to develop the monolithic integration of the electrically-injected laser, waveguide, and modulator. It is envisaged that most of these integrations will involve coupled waveguides to guide laser light into guided-wave devices such as modulators and amplifiers. Therefore, it is important to develop a monolithically integrated laser/waveguide coupling system on silicon substrates to achieve high performance lasing with electrical injection as well as efficient coupling between the laser and waveguide. Unfortunately, silicon-based light emitters and electroabsorption modulators exhibit very low efficiency due to the indirect energy band structure of silicon. One attractive alternative is the integration of silicon with III-V semiconductors such as GaAs and InP and their alloys, with which high-performance lasing as well as efficient electroabsorption modulation based on the quantum-confined Stark effect (QCSE) in quantum well (QW) structures can be realized [23] [94]. Reasonably high-performance InGaAs/GaAs QD lasers grown directly on silicon have also been demonstrated [21], as discussed in Chapter 2. Although strong QCSE can be ideally realized in QDs [95], the low density of In(Ga)As/GaAs self-organized QDs and non-uniformity of dot size make such quantum dots inferior to quantum wells for the application in electroabsorption modulators.

This thesis work first conducted theoretical examination and experimental investigation of a monolithically integrated laser-waveguide device fabricated with the *same* InGaAs/GaAs quantum dot (QD) heterostructures grown on silicon by solid-source molecular beam epitaxy (MBE). Focused-ion-beam (FIB) etching was utilized to form high qual-

ity facets for laser cavity feedback and grooves for coupling as well as electrical isolation between the laser and waveguide. A theoretical model, based on the transmission matrix and generalized laser beam propagation approach, has been developed to analyze the dependence of laser-waveguide coupling on etched facet reflectivity, groove width and laser beam quality, and was applied to optimize the device design. The model, which is not limited to a Gaussian beam, more accurately describes the coupling behavior of an edge-emitting laser groove-coupled with another guided-wave section. In the development of this novel coupling model for coupled-cavities, the physical origin of Gouy phase shifts has been revisited (see Appendix D). The dependence of laser-waveguide coupling on the etched groove width and injection current has been characterized and compared to simulations. It is observed that high-quality FIB etched facets has reflectivity R~0.28 (comparable to R~0.31 for cleaved GaAs facets), which produce laser performance comparable to those with cleaved facets. Efficient coupling with coefficients up to 30% for well defined grooves has been achieved in our integrated laser/waveguide on silicon.

Next, the monolithic integration of an InGaAs/GaAs QD laser and a QCSE-based QW electroabsorption modulator directly on silicon, by using molecular beam epitaxial (MBE) growth and regrowth and focused-ion-beam (FIB) etching techniques, was implemented and characterized. The scheme allows independent design of the laser and modulator active regions and accurate alignment of the absorption band edge of QWs with respect to the lasing wavelength of QDs. Such alignment is achieved through optimization of the QD growth conditions and QW thickness and composition, which are characterized by photoluminescence (PL) and lasing spectra measurements. The groove-

coupled laser/modulator on silicon exhibits a coupling coefficient greater than 20% and a modulation depth of ~100% at a bias of -5V.

In what follows, the generalized coupling model is discussed in Sec 3.2. Sec. 3.3 discusses high-performance FIB-etched-facet QD lasers. The integrated QD laser-waveguide on silicon is described in Sec.3.4. The monolithic integration of QD lasers and QW electroabsorption modulators on silicon is addressed in Sec.3.5. Finally, Sec.3.6 gives a conclusion.

3.2. Groove-Coupled Cavity: Modeling

A critical issue of the monolithic integration of the edge-emitting laser and planar guided-wave devices is the optimization of the optical coupling between both devices involving etched facet quality and groove dimension in a groove-coupling scheme [96]. A simplified coupling mode, suitable for Gaussian beams, was presented in terms of transmission matrices [96] [96]. However, the planar edge-emitting laser beam is usually far from a Gaussian shape [98]. Here, a novel coupling model based on transmission matrices, generalized beam propagation theory and Gouy phase shifts has been developed. This model requires information concerning facet reflectivity, waveguide cavity loss, Gouy phase shift, and beam quality characteristics such as waist width w_0 and beam-quality factor M^2 [99]. The facet reflectivity and waveguide cavity loss are obtained from evaluating the dependence of threshold current density and slope efficiency of light-current characteristics on laser cavity length, respectively. The beam quality characteristics are obtained from images of the laser near/far field patterns. As we know, Gouy phase shift is the additional axial phase shift for any focused or transversely-confined

light wave [100] [101] [102]. However, the discussion on physical origin of Gouy phase shift is ongoing [103] [104] [105]. In fact, even though this basic phenomenon was observed over 100 years ago, a quantitative characterization of Gouy phase shifts for a general beam is still not available until a recent work by Yang and Winful [106]. A detailed discussion of this work is included in Appendix D.

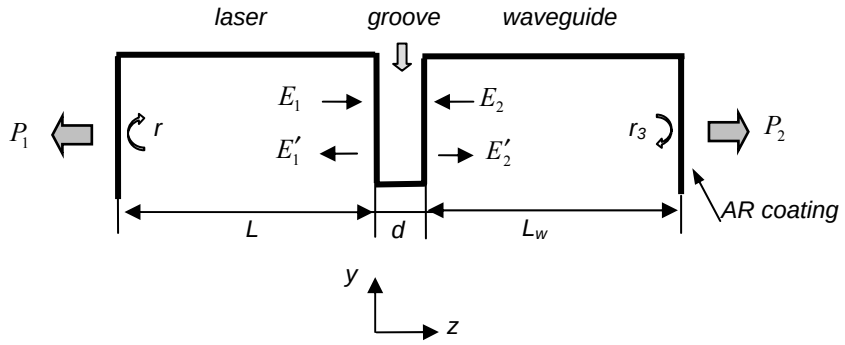

Figure 3.1: Schematic description of a laser-waveguide coupled system.

The schematic of the coupled-cavity integrated laser-waveguide system is shown in Fig. 3.1. Compared to a single cavity in which the facet reflectivity is constant for a certain wavelength, the effective reflectivity in a coupled cavity also depends on the dimensions of etched grooves, which is determined by the Fabry-Perot cavity modes formed inside grooves. Here we have developed a model based on the transmission matrix and generalized beam propagation theory to describe the reflectivities and coupling coefficients in such groove-coupled structures. Referring to Fig. 3.1 and using transmission matrices [96] [97], the optical fields E in the coupled cavity are related by:

$$\begin{pmatrix} E_1' \\ E_2' \end{pmatrix} = \begin{pmatrix} S_{11} & S_{12} \\ S_{21} & S_{22} \end{pmatrix} \begin{pmatrix} E_1 \\ E_2 \end{pmatrix}. \tag{3-1}$$

Here

$$S_{11} = r_1 - \frac{r_2(1-r_1^2)t(2d)}{1-r_1 r_2 t(2d)}, \tag{3-2a}$$

$$S_{22} = r_2 - \frac{r_1(1-r_2^2)t(2d)}{1-r_1 r_2 t(2d)}, \tag{3-2b}$$

$$S_{12} = S_{21} = \frac{t(d)\left[(1-r_1^2)(1-r_2^2)\right]^{1/2}}{1-r_1 r_2 t(2d)}, \tag{3-2c}$$

where $r_{1,2}$ are the amplitude reflectivities of each etched facets. Amplitude transmission functions *t(d)* and *t(2d)* account for the phase shift and loss experienced by optical fields for a single pass and roundtrip inside the groove, respectively (d is the groove width shown in Fig. 1). These losses arise mainly from beam diffraction and have been estimated using a Gaussian beam propagation method [96]. Here we utilize the generalized beam propagation approach, with intensity-moment based beam parameters such as beam width and beam quality factor M^2, to estimate the diffraction loss. In addition, the phase contribution from Gouy phase shifts is taken into account in this generalized model.

Transmission functions *t(d)* and *t(2d)* are given by

$$t(z = d, \text{or } 2d) = \exp\left(ikz + i\Phi_G(z)\right)T(z), \tag{3-3}$$

where $k=2\pi/\lambda$ (λ is the wavelength in vacuum). The phase shifts include not only the plane wave phase shift kz but also the Gouy phase shift Φ_G defined in Eq. (D-20b).

$$\Phi_G = -\sum_{r=x,y}\left(M_r^2/2\right)\tan^{-1}\left(z/z_r\right)$$

The Gouy phase shift is an extra axial phase shift due to the transverse spatial confinement of finite beams, and becomes significant when the groove width is comparable to or larger than the Raleigh range. Note that the Raleigh range is typically around the order of micrometer for edge-emitting semiconductor lasers due to their small beam-

waist width perpendicular to the diode junction plane [98]. Unfortunately, the Gouy phase shift was omitted in previous analyses for coupled cavities. The function *T(z)* represents the diffraction losses. It can be expressed as the overlap integration of amplitude profiles of a beam at facets experiencing a single pass or a roundtrip in the groove, namely

$$T(z=d,\text{or } 2d) = \frac{\left|\int_{-\infty}^{\infty} E_{z'=0}(x,y)E_{z'=z}(x,y)dxdy\right|}{\left(\int_{-\infty}^{\infty} E_{z'=0}^2(x,y)dxdy \cdot \int_{-\infty}^{\infty} E_{z'=z}^2(x,y)dxdy\right)^{1/2}} = \prod_{\xi=x,y}\left(\frac{2w_\xi(0)w_\xi(z)}{(w_\xi(0)^2 + w_\xi(z)^2}\right)^{1/2}. \quad (3\text{-}4)$$

In the above derivation, we use for simplicity an equivalent Gaussian amplitude profile for the real beam with the equal beam width $w_\xi(z)$, which is defined by intensity moments through

$$w_\xi(z)^2 = 4\int_{-\infty}^{+\infty}\xi^2 E(\xi)^2 d\xi \Big/ \int_{-\infty}^{+\infty} E(\xi)^2 d\xi \quad (3\text{-}5)$$

and is governed by the following propagation law [107][108]

$$w_\xi(z - z_{0\xi}) = w_{0\xi}\left[1 + \left((z - z_{0\xi})/z_{R\xi}\right)^2\right]^{1/2}. \quad (3\text{-}6)$$

Here $z_{0\xi}$ is the position of beam waist along the x- or y-axis (ξ=*x, y*).

This approach, which applies to a general beam (not limited to a Gaussian beam) and includes Gouy phase shifts, more accurately describes the behavior of an edge-emitting semiconductor laser beam in coupled cavities.

3.2. QD Lasers with Focused-Ion-Beam Etched Facets

Facet cleaving provides almost perfect mirrors; however, it tends to be incompatible with monolithic integration. An alternative approach is to form Fabry-Perot cavity mir-

rors by etching facets with reactive ion etching (RIE) [96] [109] and FIB etching [110] [111] techniques. RIE etched facets usually suffer from sidewall roughness and non-perfectly parallel mirrors. FIB etching has the advantages of direct milling to form fine patterns with a high aspect ratio. Here, the FIB etching tool we use is the FEI Nova nano-lab dualbeam FIB workstation, in the University of Michigan Electron Microbeam Analysis Laboratory (EMAL). This tool uses gallium as etching source and Pt as protection coating source, and is associated with a high-resolution scanning electron microscope (SEM).

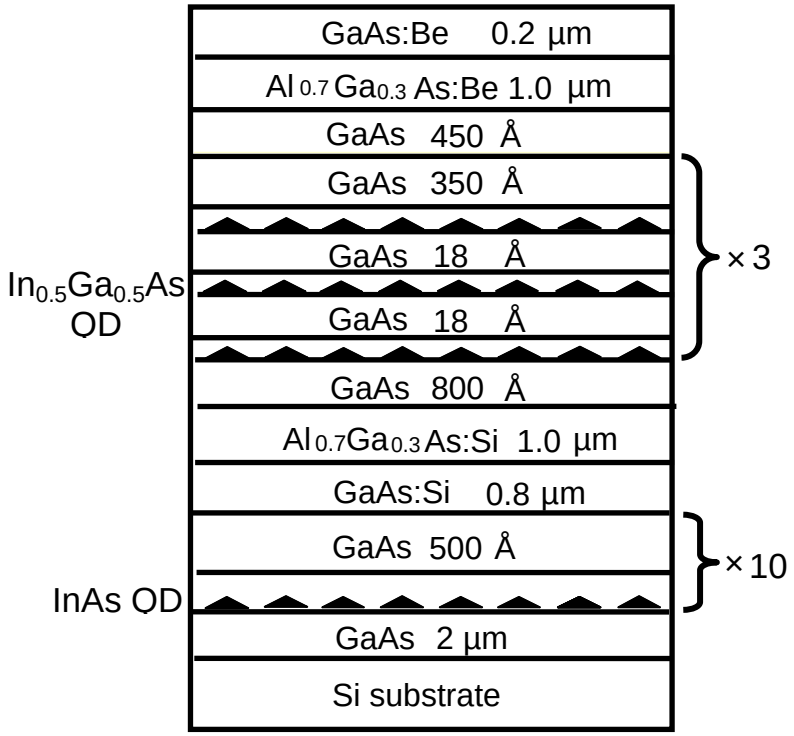

Figure 3.2: Schematic of self-organized $In_{0.5}Ga_{0.5}As$ quantum dot laser heterostructures grown by MBE on Si substrates with GaAs buffer and a dislocation filter consisting of 10-layer InAs quantum dots.

First, the GaAs/AlGaAs/$In_{0.5}Ga_{0.5}As$ QD separate confinement heterostructure, shown in Fig. 3.2, is grown by MBE on GaAs and on (001)-oriented Si substrates misoriented 4° toward <111>, respectively. For lasers on silicon, as discussed in Chapter 1, a thin (≤2 μm) GaAs buffer layer was first grown by metal-organic vapor phase epitaxy (MOVPE), and ten layers of InAs QDs are incorporated as an additional dislocation filter [21]. The In(Ga)As QD layers, GaAs layers and $Al_{0.7}Ga_{0.3}As$ cladding layers were grown at 500°C, 580°C and 620°C, respectively. Then, ridge waveguide lasers were fabricated by standard photolithography, wet/dry etching, contact metallization and facet cleaving techniques.

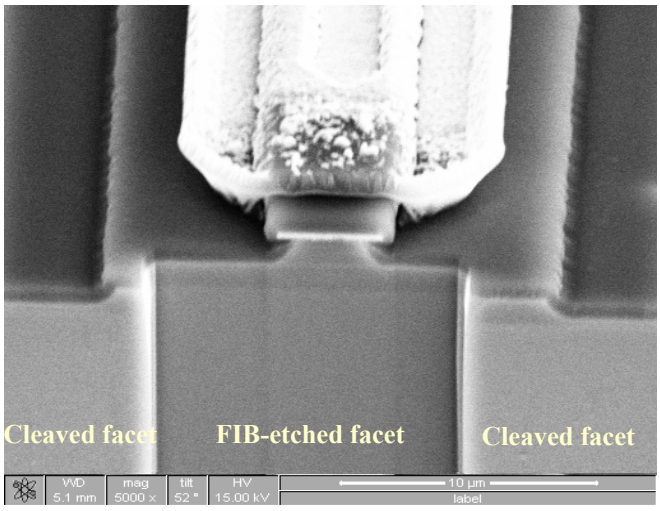

Figure 3.3: Scanning electron microscopy image of the cross-section of an InGaAs/GaAs quantum dot laser with a focused-ion-beam etched facet.

We initially used FIB to create facets of InGaAs/GaAs QD lasers grown on GaAs substrates. The scanning-electron-microscopy (SEM) image of FIB-etched facets is shown in Fig. 3.3. The measured output light-current characteristics for a laser with

cleaved facets and a laser with one cleaved and one FIB-etched facet are shown in Fig. 3.4(a). The reflectivity of the etched facets can be estimated from a plot of the threshold current density J_{th} versus the reciprocal cavity length L, as shown in Fig. 3.4(b). This relationship is [112]

$$J_{th} = J_{th}(\infty) + (C / L)\ln\left(r^{-2}\right), \tag{3-7}$$

where r is the reflectivity of the cavity facets and the constants $J_{th}(\infty)$ and C are extracted from the cleaved facet data shown in Fig. 3.4(b). Then, according to the threshold current for a laser with one cleaved and one FIB-etched facet [shown in Fig. 3.4(a)] and Eq. (3-7), we can get the reflectivity of the etched facets $r\sim0.53$ ($R=r^2\sim0.28$), which is comparable to $r=0.556$ ($R=r^2\sim0.31$) for cleaved GaAs facets.

FIB etching was extended to create facets of the InGaAs/GaAs QD laser grown on Si. A SEM image of the FIB-etched facet is shown in Fig. 3.5(a). Figure 3.5(b) displays the output light-current (L-I) relation for QD lasers on Si with cleaved facets and FIB-etched facets. The performance of both cleaved and FIB-etched facets are comparable, indicating that FIB etching can provide high quality etched facets for integrated QD laser/waveguide on Si.

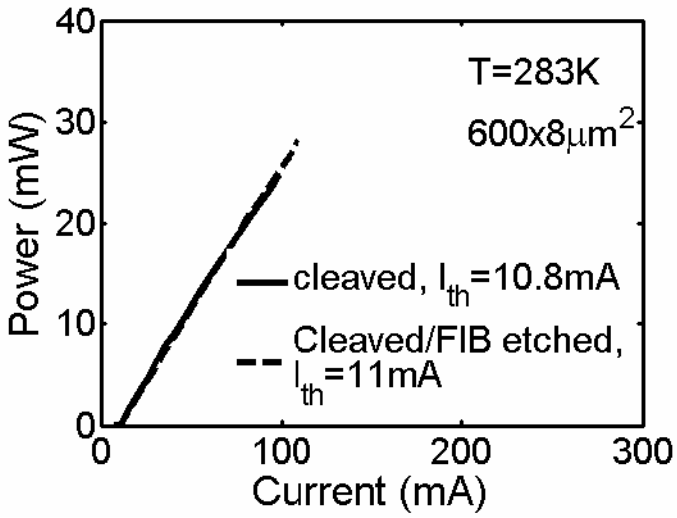

(a)

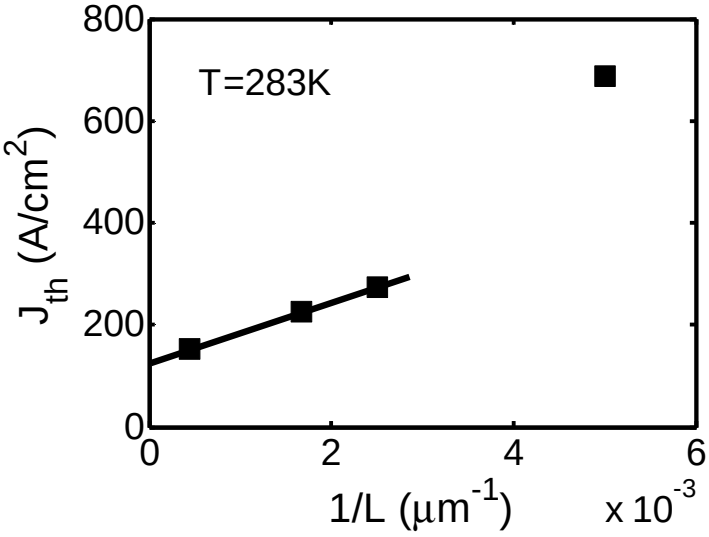

(b)

Figure 3.4: (a) Light-current characteristics of InGaAs quantum dot laser on GaAs with cleaved facets, and with one cleaved and one focused-ion-beam etched facet; (b) threshold current versus the reciprocal cavity length.

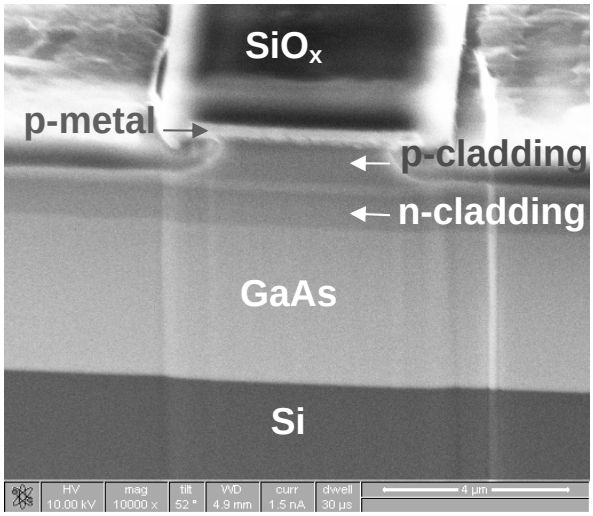

(a)

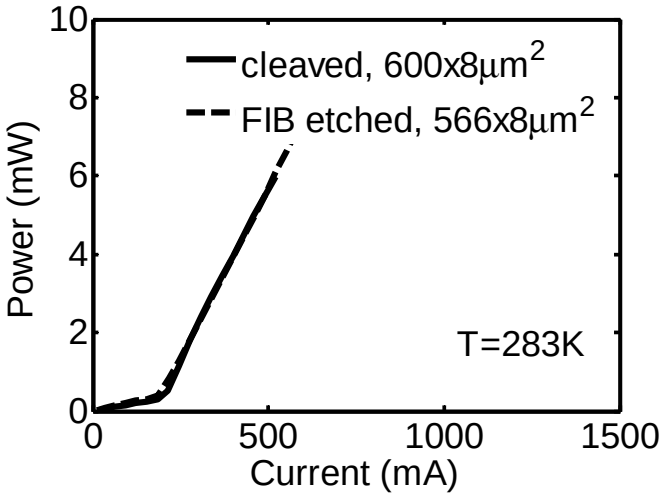

(b)

Figure 3.5: Scanning electron microscopy image of focused-ion-beam etched facet of an In-GaAs quantum dot laser on Si; (b) light-current characteristics of lasers with cleaved facets and focus-ion-beam etched facets.

3.3. Groove-Coupled Laser/Waveguide on Silicon

The beam quality, which determines the coupling coefficient as mentioned in the model above, is a critical parameter in laser-waveguide coupled systems. From Eq. (3-6), the beam quality characteristics such as waist width w_0 and beam-quality factor M^2 can be estimated from near/far field patterns on different planes along the propagation direction. The field patterns of QD lasers were captured with an *Electrophysics 7290A Micron-viewer* infrared camera and one of which is shown in Fig. 3.6(a). The output beam was imaged by a lens and attenuated by neutral density filters to avoid signal saturation in the CCD camera. For an elliptic laser beam shape, the beam quality factor M^2, beam width w_0 and Rayleigh range z_R have to be determined separately for the *x*- or *y*- axis. The measured beam characteristics are listed in Table 3.1 under a bias current I=1.5I_{th} (I_{th}— laser threshold current). The ridge waveguide edge-emitting QD laser on silicon exhibits an elliptic beam shape with M^2~2.2, w_0~4.5 μm and z_R~28 μm along the x-axis (the direction parallel to diode junction plane) and M^2~1.5, w_0~0.65 μm and z_R~1 μm along the y-axis (the direction perpendicular to diode junction plane). The Rayleigh range along the y-axis is much shorter than that along the x-axis because the former has a smaller beam waist. This finding indicates that the beam properties perpendicular to the diode junction plane play a dominant role in determining the coupling characteristics. Additionally, it is found that the beam quality degrades and becomes more divergent under higher current bias, as shown in Figs. 3.6(b) and (c). This phenomenon has been observed by other researchers as well [113].

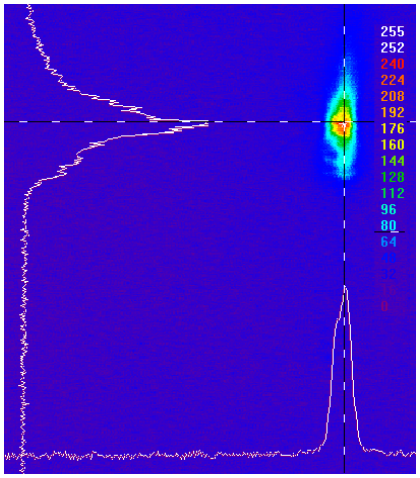

(a)

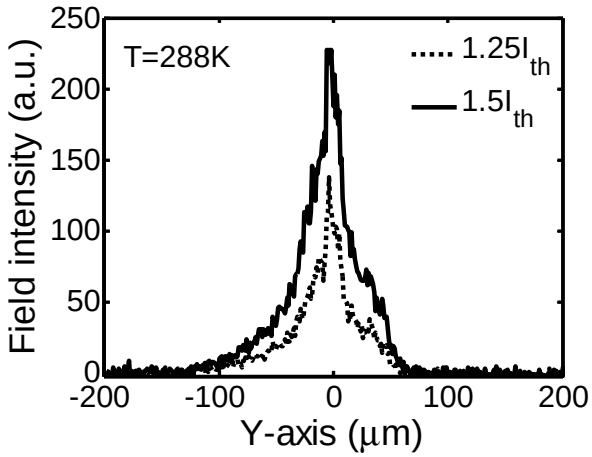

(b)

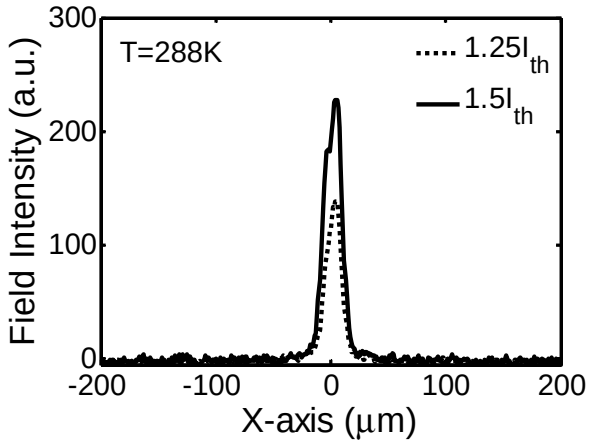

(c)

Figure 3.6: (a) Two-dimensional field pattern of the quantum dot laser beam at injection current $I=1.5I_{th}$; field intensity along the x-axis (b) and the y-axis (c) under different bias conditions.

Table 3.1: Beam quality characteristics along x-and y-axis with $I=1.5I_{th}$

Parameter	Parallel (x-axis)	Perpendicular (y-axis)
M^2	2.2	1.5
W_0 (μm)	4.5	0.65
z_R(μm)	28	1

FIB is used to etch grooves with different dimensions for electrical isolation and optical coupling between the laser and waveguide. The length of lasers and waveguides are 400 μm and 250 um, respectively. Additionally, the output facet of the waveguide is anti-reflection-coated with λ/4-thick Al_2O_3 film deposited by using e-beam evaporation. The refractive index of the film is measured to be 1.578, which yields transmission up to 97% by using following relation

$$R = \left(\frac{n_{sub} n_{air} - n_c}{n_{sub} n_{air} + n_c} \right)^2 \tag{3-8}$$

where, n_{sub}, n_{air}, and n_c are the reflective index of substrates, air and anti-reflection coating.

The coupling grooves are FIB-etched through the whole QD heterostructures to achieve complete electrical isolation between the laser and waveguide. By using the model above with measured reflectivity of etched facets as well as measured beam characteristics such as waist width w_0 and quality factor M^2, we plotted the groove reflectivity $|S_{11}|^2$ and coupling coefficient $|S_{12}|^2$ versus groove width d in Fig. 3.7. From the dependence of $|S_{11}|^2$ and $|S_{12}|^2$ on d, we chose the value of d for which a cavity reflectivity $|S_{11}|^2$ comparable to a single cleaved facet and an acceptable value $|S_{12}|^2$ are obtained simultaneously. In our experiments, we etched grooves with d of 1.25 μm, 3.3 μm and 8.9 μm. A

SEM image of the QD heterostructure laser/waveguide on Si with a FIB-etched groove with d=3.3 μm is shown in Fig. 3.8(a). We measured the L-I light-current characteristics from both the laser and coupled waveguide ends, as shown in Fig. 3.8(b). Measurements are made under pulsed bias conditions (1% duty cycle of 100 μs). Care is taken to prevent scattered light from the coupling groove to reach the detector.

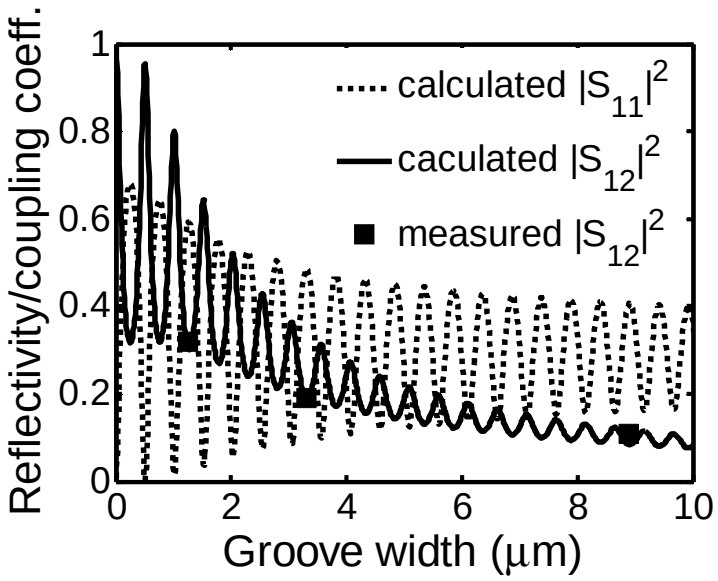

Figure 3.7: Reflectivity ($|S_{11}|^2$), calculated and measured coupling coefficient ($|S_{12}|^2$) versus the groove width of a laser beam with w_0~4.5μm, M^2~2.2 along the x-axis, and w_0~0.65μm, M^2~1.5 along the y-axis.

Using the experimental data and referring to Fig. 3.1, the coupling coefficient is calculated through the following formula

$$|S_{12}|^2 = \frac{P_2}{P_1} \cdot \left| \frac{1 - S_{11} r_3 t_2^2}{t_2} \right|^2 \left(\frac{t_1}{t_3} \right)^2 \sim \frac{P_2}{P_1} \cdot \left(\frac{t_1}{|t_2| t_3} \right)^2 . \tag{3-29}$$

Here P_1 is the output power from the laser end, P_2 the output power from the waveguide end. t_1 is the transmittance of cleave facet, t_3 is the transmittance of AR coating. $t_2=exp[(ik-\alpha/2)L_w]$, and L_w is the waveguide length. α~10±2 cm^{-1} is the cavity loss of QD heterostructure waveguides. This value is estimated from the dependence of the slope efficiency $\Delta P/\Delta I$ of the L-I characteristics on laser cavity length L [112], namely, $\Delta P/\Delta I \propto \left(\alpha L + \ln(1/r^2)\right)^{-1}$ where r=0.556 is the reflectivity of GaAs facets. The experimental coupling coefficients $|S_{12}|^2$ measured for different current bias and groove width are listed in Table 3.2. These results are consistent with the simulated results as shown in Fig. 3.7. It is observed that the coupling effect degrades with higher bias and wider groove. As mentioned above, since the beam quality degrades under higher current bias, more light spreads out off the groove, which becomes more influential for wider grooves.

Table 3.2: Coupling coefficients with different current bias and groove width

Injection current	Coupling coefficients $\|S_{12}\|^2$ (with variation ×10%)		
I	*d=1.25μm*	*d=3.3μm*	*d=8.9μm*
$1.25I_{th}$	35%	25%	13%
$1.5I_{th}$	31%	20%	11%
$2I_{th}$	27%	17%	9%

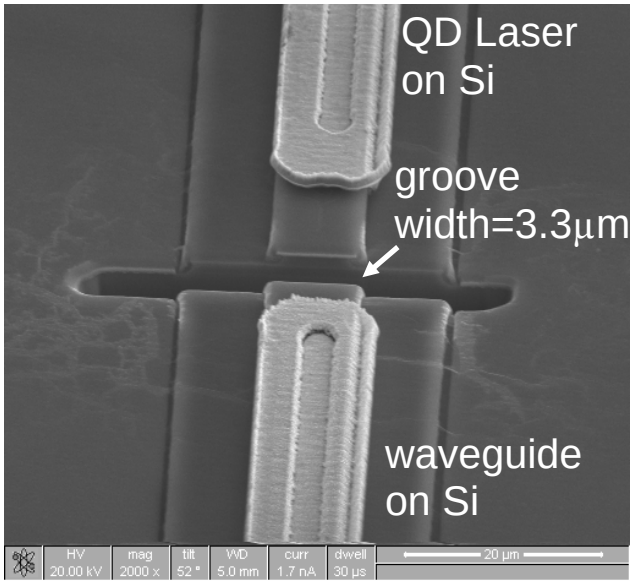

(a)

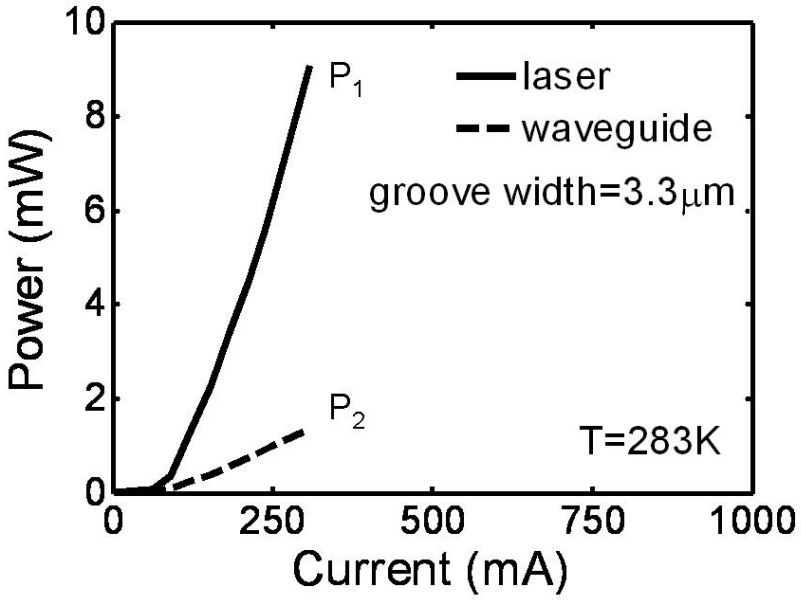

(b)

Figure 3.8: (a) Scanning electron microscopy image of an integrated quantum dot laser/waveguide on silicon; (b) light-current characteristics of an InGaAs quantum dot laser and coupled waveguide under pulsed bias mode (1% duty cycle of 100 μs), showing output from cleaved facet and from waveguide.

3.4. Monolithic Integration of Quantum Dot Lasers and Quantum Well Electroabsorption Modulators on Silicon

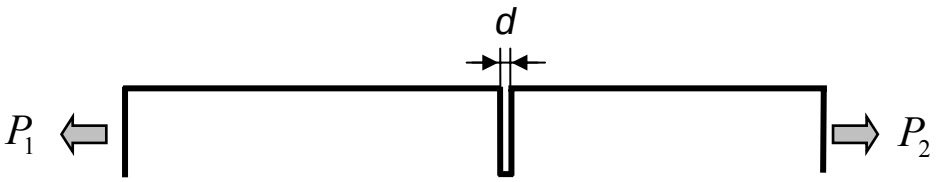

(a)

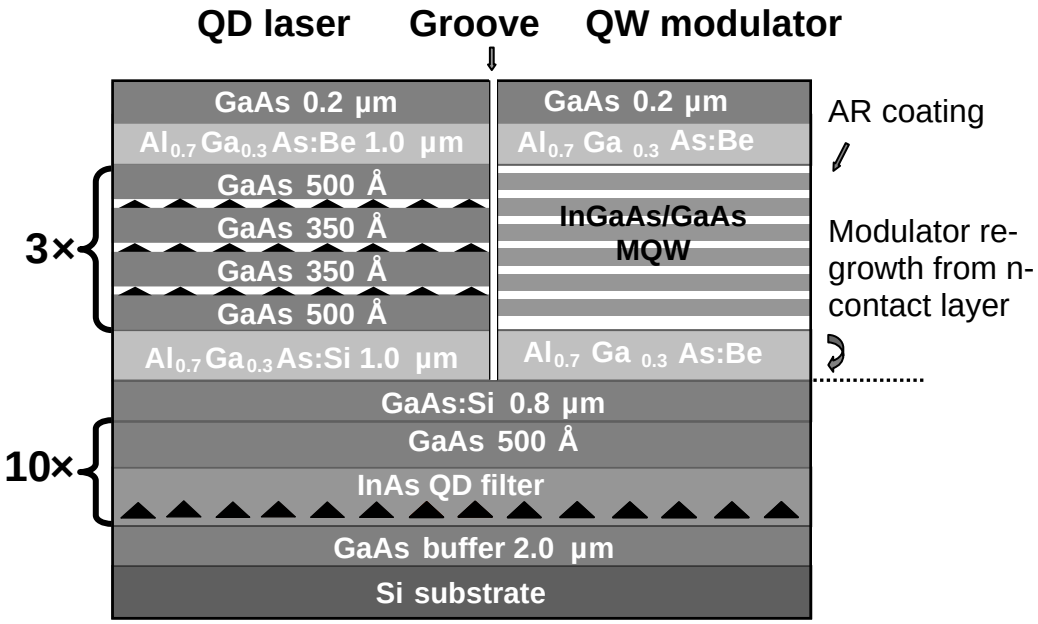

(b)

Figure 3.9: Schematic of an integrated quantum dot laser and quantum well modulator on silicon with a GaAs buffer layer and a dislocation filter consisting of 10-layers of InAs quantum dots: (a) groove-coupled cavities and (b) heterostructure, grown by molecular beam epitaxy (drawing is not to scale).

The groove coupled laser-modulator heterostructure is schematically shown in Fig. 3.9. The laser heterostructure is grown by MBE following the same procedure as discussed in Chap.1. Then, the wafer consisting of the laser heterostructure is patterned and etched to create trench where the modulator heterostructure is to be regrown. Most material within defined regions is etched by Cl_2/Ar inductively coupled plasma (ICP) dry etching which can get vertical profile of trenches. Then, BHF wet etching is use to selectively remove the rest thin layer of $Al_{0.7}Ga_{0.3}As$ n-cladding (~0.1-0.2 μm), and stop at the top surface of GaAs n-contact layer. Before MBE regrowth, 0.2 μm-thick SiO_x is deposited, by PECVD, as a protection layer, and then is repattern and etch to open the defined trenches. The p-i(MQW)-n QCSE modulator heterostructure with seven $In_{0.2}Ga_{0.8}As$/GaAs QWs in the active region is regrown by MBE in the patterned grooves. It is important to note that the depth of the grooves and the total thickness of the modulator heterostructure are carefully adjusted such that the QD and QW active regions of the laser and modulator, respectively, are closely aligned. For an ideal QCSE modulator, the best modulation results are obtained when the incident photon energy is ~15-20 meV below the excitonic absorption peak of the QWs at zero applied bias. With the application of an appropriate transverse bias, the absorption edge is red shifted, resulting in strong absorption [23]. In our experiments, the QW thickness and composition are tuned by measuring the PL emission of the QD and QW materials shown in Fig. 3.10(a), noting that the excitonic absorption edge and PL peak of the QW are very close for negligible Stokes shift. It may also be noted that QD lasers on silicon generally lase from the first excited states of the dots due to a relative large cavity loss [see Fig. 3.10(b)]. A 15 meV

energy difference between QW and QD (first excited state) emission is achieved by 85 Å $In_{0.2}Ga_{0.8}As$ QWs with 150 Å GaAs barriers.

After regrowth of the QW heterostructures, processing of the ridge waveguide coupled laser-modulator is done using standard optical photolithography, wet/dry etching and contact metallization techniques. The wafers are thinned down to ~90 μm and the laser facet is cleaved in the (110) direction. An anti-reflection (AR) coating consisting of λ/4-thick Al_2O_3 is deposited on the modulator facet by electron beam evaporation. The refractive index of the film is measured to be 1.578, which yields a transmission upto 97%. Finally, FIB etching is used to create the coupling groove between the laser and modulator. The groove also electrically isolates the two devices. In our experiments the length of the laser and modulator sections are 400μm and 250um, respectively. A SEM image of the fabricated laser-modulator is shown in Fig. 3.11. Taking into account lateral growth that takes place during the ~2 μm modulator regrowth step, the groove width needs to be ~ 5 μm. Coupling grooves of 5.25 μm width and 5-7 μm deep were etched in the devices, which provide a reflectivity comparable to cleaved facets and an acceptable value of coupling coefficient simultaneously [referring to Fig. 3.12]. The more detailed processing flow and recipe is described in Appendix E.

The measured light-current characteristics for output from the laser end and the coupled modulator end at zero bias are shown in Fig. 3.14(a). The modulated output, for laser injection current $J=2J_{th}$, versus reverse bias is plotted in Fig. 3.14(b). Care is taken to prevent scattered light from the coupling groove to reach the detector. The coupling coefficient $|S_{12}|^2$ is greater than 20%. The modulation depth is ~45% for an applied bias of -3 V and increases to ~100% at a bias of -5 V. We attribute the large bias in the latter case to

the quality of the regrowth interface, which may contain interfacial defects. A deeper etching and regrowth on the GaAs buffer layer, instead of on the n-contact layer, would help to improve the material quality and performance of regrown modulators.

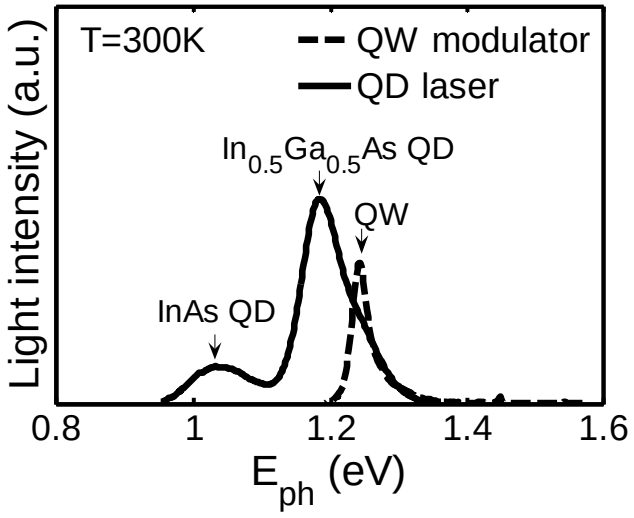

(a)

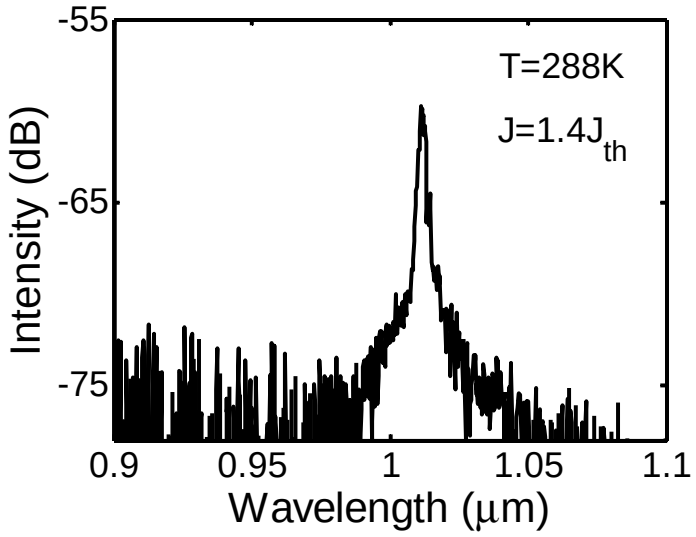

(b)

Figure 3.10: (a) Room-temperature photoluminescence spectra for the $In_{0.5}Ga_{0.5}As$ quantum dot active region, InAs quantum dot buffer layer and multiple $In_{0.2}Ga_{0.8}As$ quantum wells on silicon; (b) lasing spectrum for the $In_{0.5}Ga_{0.5}As$ quantum dot laser section of a coupled laser-modulator on silicon.

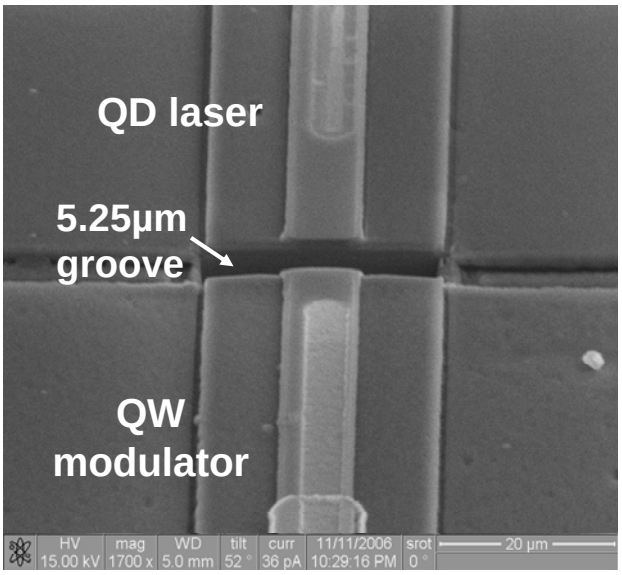

Figure 3.11: A scanning electron microscopy image of the groove-coupled quantum-dot laser and quantum-well electroabsorption modulator on silicon.

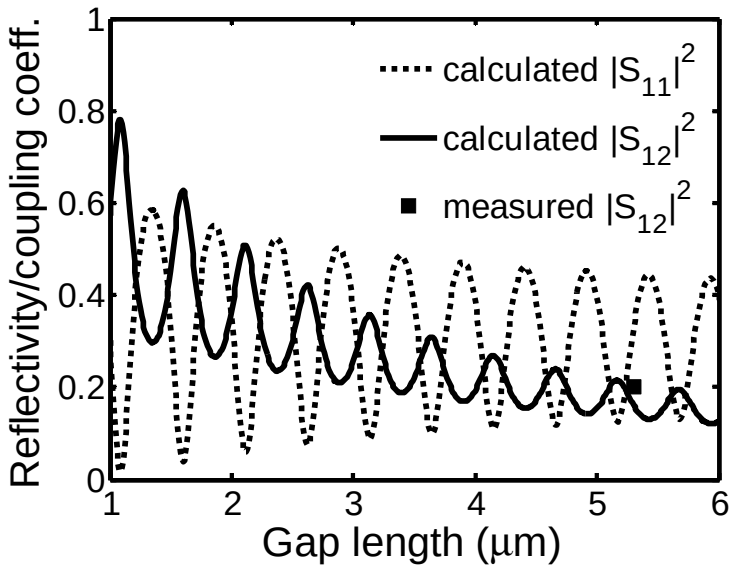

Figure 3.12: Calculated coupling coefficient versus groove width for a laser beam with the beam width 0.65 μm and beam quality factor M^2~1.5 perpendicular to the junction plane. The measured coupling coefficient is for a groove width of 5.25 μm under a laser injection current $J=2J_{th}$.

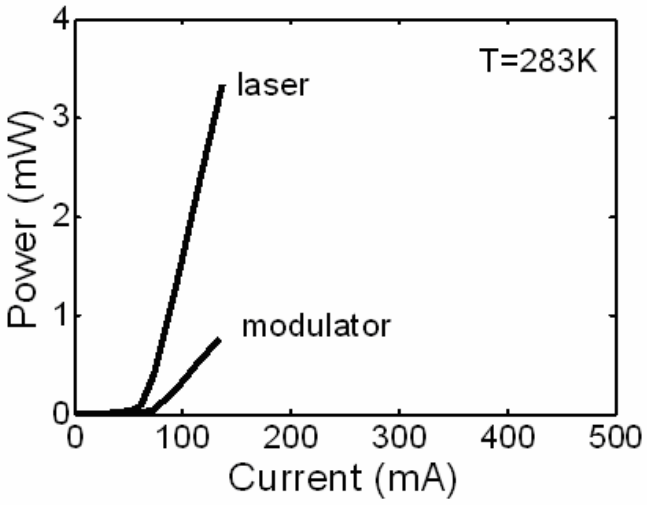

(a)

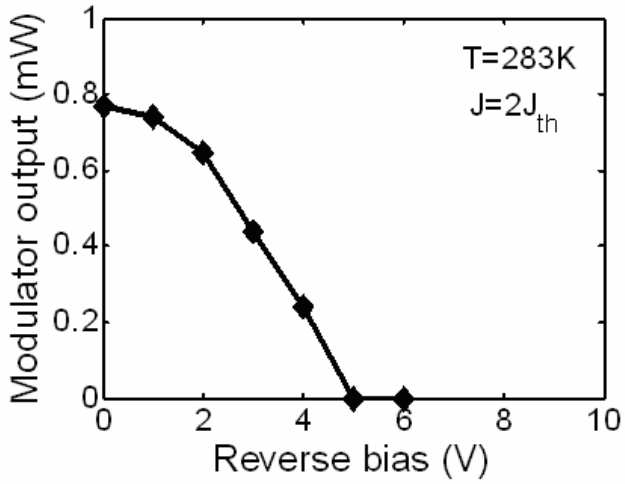

(b)

Figure 3.13: (a) Light-current characteristics for output from the laser end and the coupled modulator end at zero bias; (b) modulator output versus reverse bias under laser injection current $J=2J_{th}$. The dimensions of the laser and modulator sections are 400×8 μm^2 and 250×8 μm^2, respectively.

3.5.Conclusion

In conclusion, a groove-coupled laser/waveguide on silicon implemented with MBE grown In(Ga)As/GaAs quantum dot heterostructures and focused-ion-beam etched facets has been demonstrated. The efficient coupling between the two devices was verified with a model based on transmission matrix, generalized beam propagation theory in terms of intensity moments and Gouy phase shifts, and measured characteristics of devices. A coupling coefficient up to 30% has been achieved for well-defined grooves. A mono-lithically integrated laser and modulator grown and fabricated directly on Si substrate has been demonstrated. The laser and modulator have quantum dot and quantum well active regions, respectively. Efficient coupling between the laser and modulator sections $\geq$ 20% and a modulation depth of ~100% with a bias of -5 V applied to the modulator section has been measured.

CHAPTER 4

QUANTUM DOT LASER INTEGRATED WITH HYDROGENATED AMORPHOUS SILICON WAVEGUIDE ON SILICON

The monolithic integration of epitaxially-grown InGaAs/GaAs self-organized quantum dot lasers with hydrogenated amorphous silicon (a:Si-H) waveguides on silicon substrates is demonstrated. Hydrogenated amorphous silicon waveguides, formed by plasma-enhanced-chemical-vapor deposition (PECVD), exhibit a propagation loss of ~10 dB/cm at the wavelength of 1.05 μm. The laser-waveguide coupling, with coupling coefficient of 22%, has been achieved through a 3.2 μm-wide groove etched by focused-ion-beam (FIB) milling which creates high-quality etched GaAs facets.

4.1. Introduction

An important component of silicon photonics is the light guide and associated guided-wave devices such as modulators and switches. With the development of microfabrication and silicon-on-insulator (SOI) technologies, reasonably low loss (≤ 3 dB/cm) silicon waveguides operating in the wavelength range of 1.3-1.55 μm have been developed [10] [31] [32]. Similarly, silicon-based modulators, based on quantum-confined Stark effect (QCSE) [23], and free-carrier plasma dispersion effect (FCPDE) [22] with various geometries such as Mach-Zehnder interferometer [26] [27] and microring resonator [28], have also been developed.

While the above developments have been achieved with crystalline silicon and SOI technology, hydrogenated amorphous silicon (a:Si-H) may offer benefits in terms of lower cost, low temperature processing, as well as other unique characteristics in photonics applications [35]. These include refractive index and bandgap tunability dependent on H composition, and a desirable thermo-optic effect specifically for low-power and low-frequency switching. Different from crystalline silicon, amorphous silicon does not have a clearly defined band structure and an abrupt band edge. In addition, the dangling bonds in a:Si-H can be saturated by H. As a result, a:Si-H exhibits an acceptable absorption loss in the wavelength range of 0.95-1.15 μm (while crystalline silicon has much higher loss in this range), and certainly a lower absorption loss at longer wavelengths [35]. Moreover, a silicon waveguide/modulator technology realized by plasma-enhanced-chemical-vapor deposition (PECVD), or similar techniques, will introduce flexibility in design and fabrication that is important for the development of silicon photonics. With this in mind, we have investigated the integration of light sources with a:Si-H waveguides, both formed on silicon substrates. This thesis work has demonstrated the on-chip integration of InGaAs/GaAs self-organized quantum dot (QD) lasers grown directly on silicon with a:Si-H waveguides formed by PECVD. The waveguides exhibit a propagation loss of ~10 dB/cm for λ=1.05 μm. The laser-waveguide coupling is achieved through a groove etched by focused-ion-beam (FIB) milling. A coupling coefficient is measured to be 22%.

4.2. Device Growth, Fabrication, and Characteristics

The groove-coupled edge-emitting QD laser/a:Si-H waveguide is schematically shown in Fig. 4.1. The GaAs-AlGaAs-$In_{0.5}Ga_{0.5}As$ QD separate confinement laser het-

erostructure was grown by molecular beam epitaxy with incorporation of ten layers of InAs QDs as a dislocation filter in the GaAs buffer layer [21]. The wafer was patterned and then dry etched, using Cl_2/Ar inductively coupled plasma (ICP), to delineate the regions where the waveguide is to be deposited. The SiO_x/a:Si-H/SiO_x multimode waveguide was deposited by PECVD at 380 °C. The PECVD processing parameters are listed in Table 4.1. Before the deposition of the SiO_x upper cladding layer, the transverse dimension of the a:Si-H waveguide was defined by ICP dry etching. It is important that the depth of the etched trench and the thickness of the waveguide core/cladding are carefully adjusted such that the laser active region and waveguide core are closely aligned. The groove-coupled laser/waveguide was fabricated by using standard photolithography, wet and dry etching, and contact metallization techniques. The wafer substrates were lapped down to ~80 μm for optimized cleaving and the integrated laser-waveguide segments were cleaved along the <110> direction. An antireflection (AR) coating consisting of λ/4-thick Al_2O_3 was deposited on the a:Si-H waveguide output facet by e-beam evaporation. The coating has the refractive index of 1.58, which is measured using ellipsometry and yields a calculated transmission of 97%.

Table 4.1: PECVD processing parameters for SiO_x and a:Si-H

Conditions	SiO_x	a:Si-H
Temperature (°C)	380	380
Gas and flow (sccm)	SiH_4 : N_2O : He=45:1980:250	SiH_4 : He=45:495
Pressure (Torr)	2.6	2.4
Power (W)	300 @RF 13.56MHz	250 @RF 13.56MHz

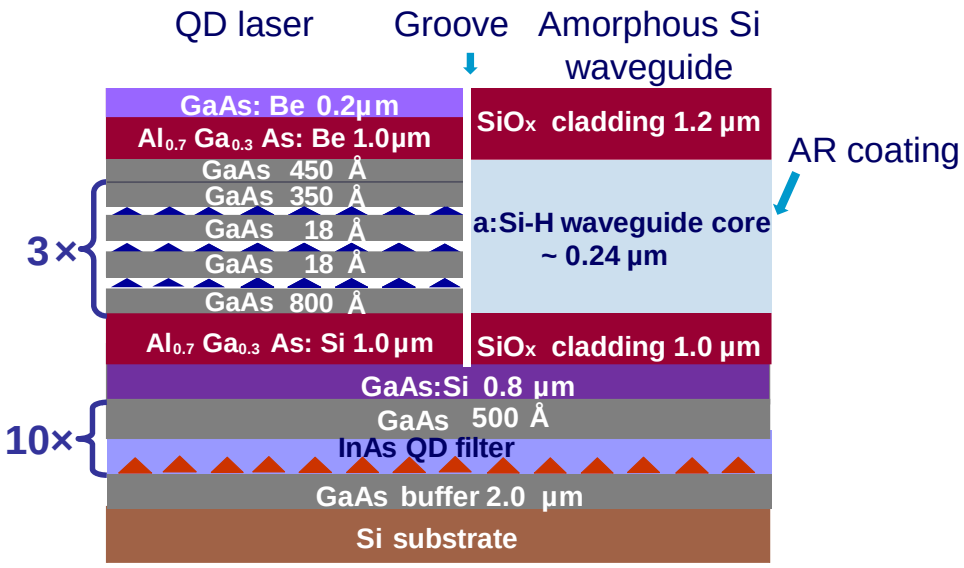

Figure 4.1: Schematic of an integrated quantum dot laser and a:Si-H waveguide on silicon with a dislocation filter consisting of 10-layers of InAs quantum dots.

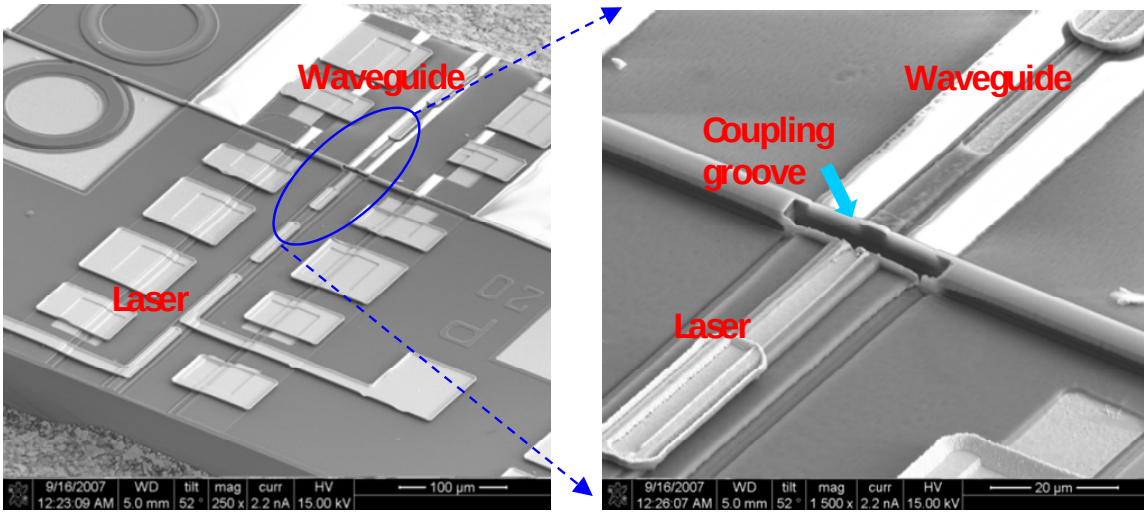

Figure 4.2: Scanning electron microscopy image of an integrated InGaAs quantum dot laser/a:Si-H waveguide on silicon with the focused-ion-beam etched coupling groove.

As discussed in Chapter 3, a critical issue in the groove-coupled edge-emitting laser and planar waveguide is optimization of the optical coupling between the two devices, which is dependent on the etched facet quality and groove dimension. In comparison with other dry etching techniques such as reactive ion etching (RIE) and ICP, FIB has the advantage of maskless etching and produces smoother surfaces and vertical sidewalls. We have utilized FIB to etch GaAs facets with a reflectivity of R~0.28 [114], which is comparable to that of a cleaved GaAs facet. In addition to high-quality etched facets, the dimension of the etched groove is critical for optimum coupling. We have calculated this coupling using a generalized transmission matrix model [114]. The model, which is not limited to a Gaussian beam, more accurately describes the coupling behavior of an edge-emitting laser groove-coupled with another guided-wave section. In our experiment, the length of the laser and a:Si-H waveguide segment are 400 μm and 250 μm, respectively, separated by a FIB-etched groove with a width of 3.20 μm. SEM images of the groove-coupled laser/waveguide are shown in Fig. 4.2.

The InGaAs/GaAs QD lasers on silicon emit at a wavelength of 1.02 μm [inset of Fig. 4(a)]. To determine the propagation loss of the PECVD a:Si-H waveguides at this wavelength range, light from a 1.05 μm Nd:glass laser was coupled into and out of the waveguide segments using single mode fibers. The output power was measured for waveguide segments of varying length, with λ/4-thick Al_2O_3 AR coating deposited on the facets. From these measurements, the waveguide propagation loss is estimated to be 10 dB/cm. The light-current (L-I) characteristics from the QD laser and coupled a:Si-H waveguide ends have been measured under pulsed bias (500 μs pulses with 1% duty cycle) and the results are shown in Fig. 4(a) and 4(b), respectively. With the measured wave-

guide loss and L-I characteristics, we have estimated the laser-waveguide coupling using the generalized matrix transmission model through the Eq. (3-29)

$$|S_{12}|^2 = \frac{P_2}{P_1}\left|\frac{1-S_{11}(1-t_3)^{1/2}t_2^2}{t_2}\right|^2\left(\frac{t_1}{t_3}\right)^2 \overset{t_3\sim 1}{\approx} \frac{P_2}{P_1}\left(\frac{t_1}{|t_2|t_3}\right)^2$$

Here, P_1 and P_2 are the output power from the laser and waveguide ends, respectively. t_1 (t_1^2~0.69) is the transmittance of the cleaved GaAs facet and t_3 (t_3^2~0.97) is the transmittance of the waveguide output facet with AR coating. $t_2=exp[(ik-\alpha/2)L_w]$, where α~10 dB/cm is the a:Si-H waveguide loss and L_w is the waveguide length. The coupling coefficient $|S_{12}|^2$ measured for the groove width of 3.20 μm is 22% at an injection current of J=1.5J_{th}, which is in good agreement with calculated values.

Laser-waveguide integration is an important aspect of integrated photonics and has been extensively investigated. The main point of this study was to demonstrate laser-waveguide integration on silicon, for potential application in optical interconnects, with a lower cost and CMOS-compatible a:Si-H waveguide technology. In addition, it should be noted that the loss of a:Si-H at longer wavelengths is smaller [35] [36], which will generate interest in the integration of these waveguides with 1.3-1.55 μm QD lasers. Such lasers have been demonstrated on GaAs substrates [115], and we are currently in the process of realizing them on silicon.

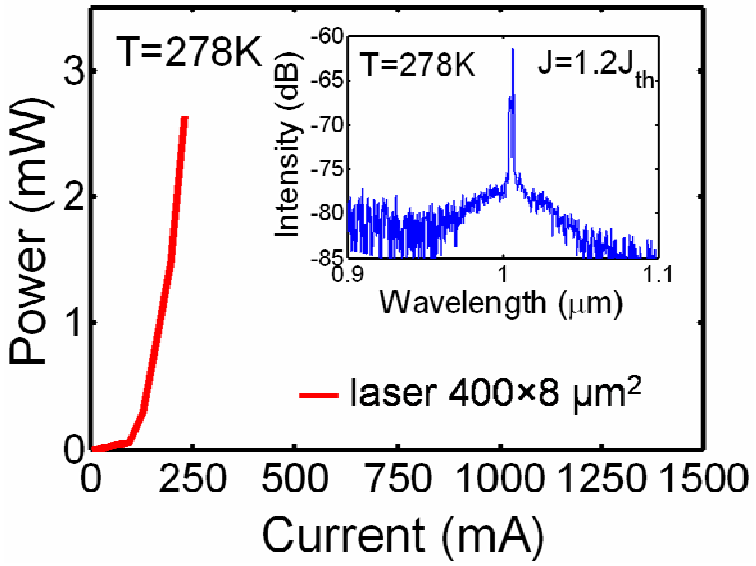

(a)

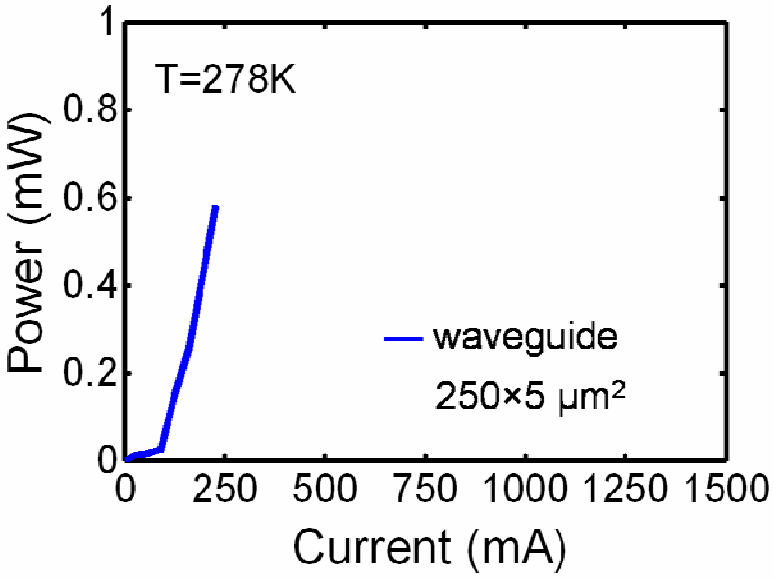

(b)

Figure 4.3: Light-current characteristics for output from the InGaAs quantum dot laser end (a) and the coupled a:Si-H waveguide (b). The inset in (a) is the lasing spectrum.

4.3. Conclusion

The monolithic integration of an epitaxially-grown quantum dot laser with a PECVD-formed a:Si-H waveguide on silicon substrates has been demonstrated for the first time. The two devices are coupled by a FIB-etched groove and the coupling coefficient is estimated to be 22%. Waveguide loss could be decreased by optimizing PECVD processing and waveguide fabrication. This technology can be extended to integrate the laser with other passive or quasi-active a:Si-H guided-wave devices on silicon.

CHAPTER 5

ENHANCED PHOTOLUMINESCENCE FROM PbSe COLLOIDAL QUANTUM DOTS IN SILICON RANDOM PHOTONIC CRYSTAL MICROCAVITIES

The experimental observation of coherent emission from high-Q silicon-based random photonic crystal microcavities embedded with PbSe colloidal quantum dots has been investigated. The emission is optically excited at room temperature by a continuous-wave Ti-Sapphire laser and exhibits randomly-distributed localized modes with a minimum spectral linewidth of 4 nm at 1.5 μm wavelength.

5.1. Introduction

There have been a host of attempts to extract light from silicon and to demonstrate lasing with radiative host materials embedded within or deposited on top of silicon. Nanostructured silicon emitters with various degrees of quantum confinement have also been investigated for light emission, with limited success [12] [13]. The two essential requirements for coherent emission are a gain medium with a high quantum efficiency and a resonant cavity with a high quality factor. A promising approach is to use chemically synthesized nanocrystals, such as Pb(S, Se) and CdSe colloidal quantum dots (QDs) as gain media, embedded in a high-Q silicon-based microcavity. Enhanced luminescence

has been demonstrated with Pb(S, Se) QDs embedded in Si photonic crystal (PC) cavities [116] [117]. The colloidal QDs, which exhibit size-tunable luminescence with high efficiency (> 80%) in the near-infrared (IR) range, represent a technologically interesting choice of gain medium for potential applications in silicon photonics [118] [119].

Photonic crystals are periodic dielectric structures, usually two-dimensional (2D) arrays of air-holes in high-refractive-index membranes, that selectively inhibit light propagation in certain bands of frequencies [120]. Destroying the periodicity of the lattice introduces small defects which act as optical cavities with high Qs wherein light can be localized by total internal and Bragg reflections. Q-factors of the order of 10^6 have been measured in engineered microcavities in 2D PCs [121]. On the other hand, Topolancik *et al.* have recently investigated and reported a different approach to photon localization in PCs, which relies on random structural perturbations introduced uniformly throughout the crystal by deliberately changing the shapes and orientations of the lattice elements (air holes) [122]. Such random disorder superimposed onto the crystal causes backscattering which impedes propagation of Bloch-waves along line-defects defined in the 2D lattice. Extended modes that propagate with a low-group-velocity at frequencies approaching the mode-edge become spatially confined in sections of the disordered waveguide. This subtle interplay of order and disorder was predicted to give rise to Anderson localization in disordered lattices [123]. Incorporation of suitable gain media into these structures could enable self-optimized lasing from random nanocavities operating around the guided mode's cutoff — similar to what has been observed at the photonic band-edge in *crescent*-deviation disordered PCs [124]. It is worth noting that disordered waveguide struc-

tures could support self-optimized nanocavity lasers with significantly smaller modal volumes and lower thresholds than the large-area, disordered PC band-edge lasers [124].

This chapter reports an experimental observation of coherent emission from PbSe QDs embedded in silicon-based random PC microcavities.

5.2. Device Fabrication

The fabrication of the devices uses a simple scheme of incorporating colloidal PbSe QDs into the random PC microcavities. The disordered PCs were fabricated on silicon-on-insulator substrates using standard electron-beam lithography and reactive ion etching. A line-defect waveguide is formed by equally spaced circular holes defined in a hexagonal lattice of randomly rotated squares. The top image of the fabricated structure is shown in the scanning electron micrograph (SEM) in Fig. 5.1(a). The thickness of the silicon slab (h=220 nm), the radius of the defect holes (r=105 nm), and the lattice constant (a=470 nm) and the fill factor (~30%) of the bulk PC were chosen so that the cutoff of the guided mode aligns spectrally with the photoluminescence (PL) peak of colloidal PbSe QDs at 1510 nm. The dispersion of the waveguide in the underlying periodic crystal calculated by plane-wave expansion method and the room temperature PL spectrum of the dots are shown in Fig. 5.1(b). The superimposed random scatterers which trigger mode-edge localization can be viewed as the difference between circles in the underlying (ideal) crystal and randomly oriented squares in the disordered crystal.

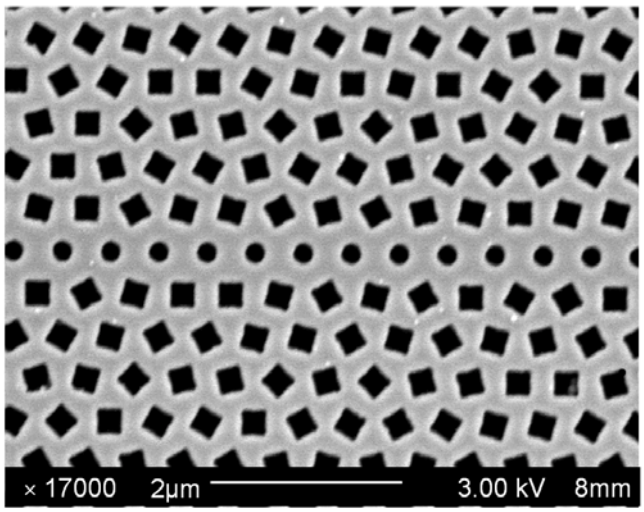

(a)

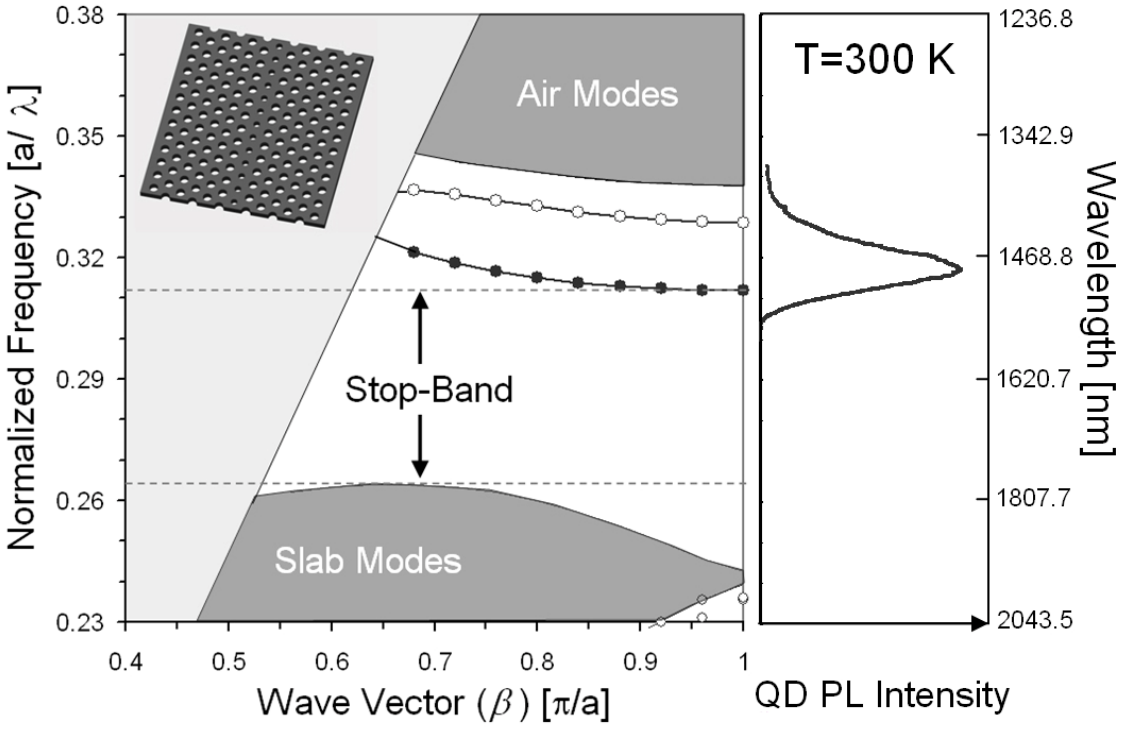

(b)

Figure 5.1: (a) Scanning electron micrograph of the fabricated Si-based two-dimensional membrane disordered photonic crystal nanocavity, (b) calculated dispersion of the defect waveguide in ideal crystal shown in the inset (hollow circles denote odd modes and solid circles denote even modes).

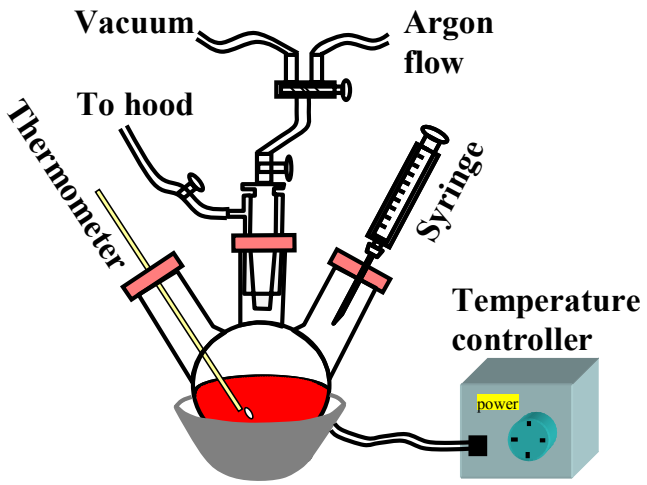

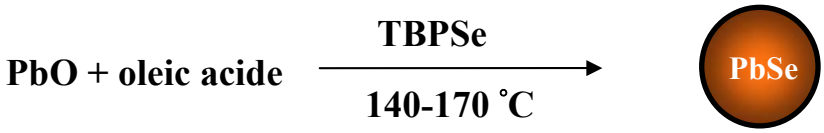

Process Flow:

- Dissolving PbO in hot stearic acid (150°C) under argon flow;
- Addition of coordinating ligands, oleic acid and trioctylphosphine oxide (TOPO), at elevated temperature to produce Pb^{2+} ions in the reaction solution;
- Initializing nanocrystal nucleation by rapidly injecting Selenide-TBP-dioctylamine reagents into the reaction solution;
- Raising solution temperature (~280-300°C) to promote the growth of highly crystalline nanoparticles;
- Growth is monitored through UV/visible absorption spectroscopy in order to reach the desired NQD size;
- Final NQD products are separated by centrifugation and decantation.

Figure 5.2: Process and flow chart for colloidal synthesis of PbSe semiconductor nanocrystal quantum dots (Courtesy of Jian Xu, Pennsylvania State University).

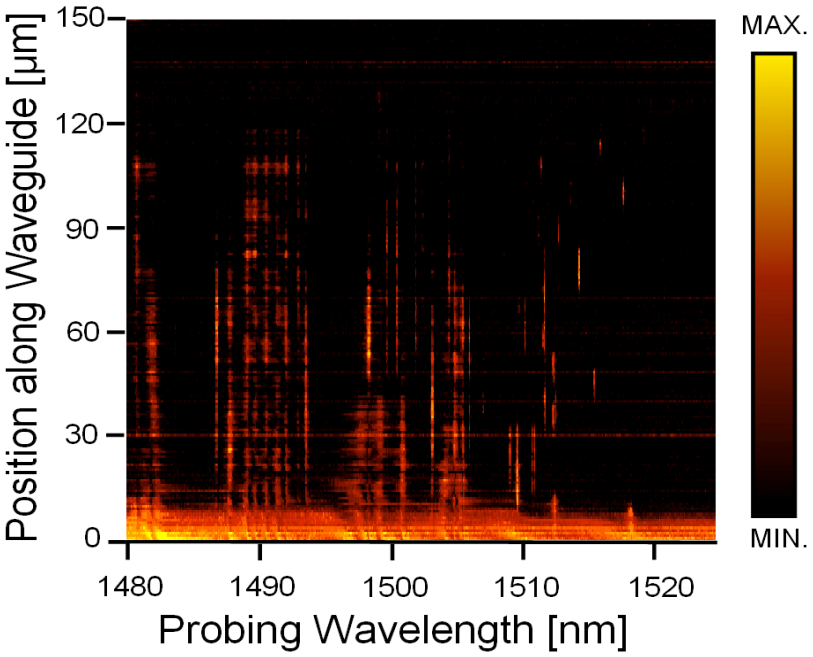

(a)

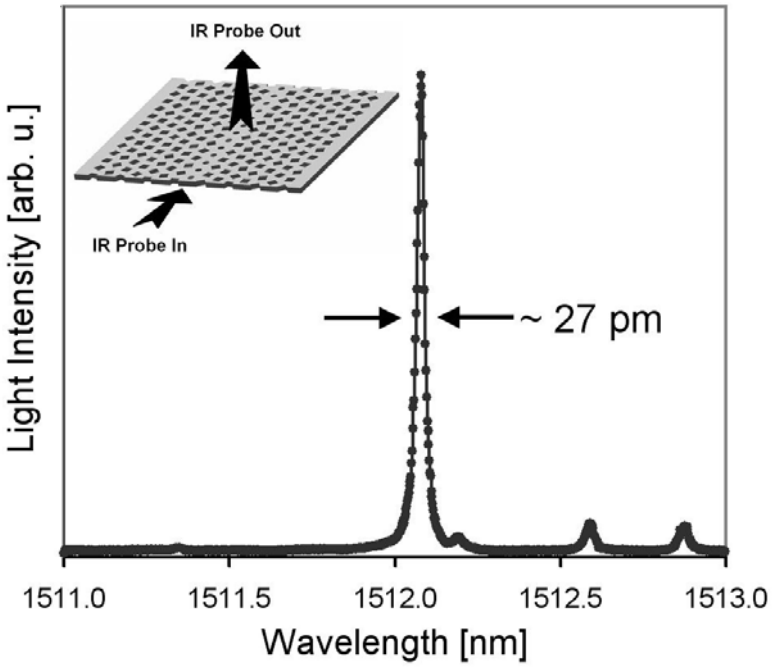

(b)

Figure 5.3: (a) Contour plot of the spatially-resolved spectra of a 150 μm-long disordered waveguide. (b) Example of a well-localized, high-Q resonance in the passive random photonic crystal microcavities. The probing and collection directions are indicated in the inset.

PbSe quantum dots were synthesized using a noncoordinating solvent technique [118] [119]. As shown in Fig. 5.2, the synthesis procedure starts with the preparation of a solution of PbO and oleic aid and the subsequent heating of the solution up to an elevated temperature of 160 °C. Rapid injection of selenium-trioctylphosphine reagents (TBPSe) into the hot solution induces the nucleation of PbSe and subsequently cooling down the reaction temperature to 135 °C allows the nuclei to grow into highly crystalline nanoparticles. The size of PbSe quantum dots can be tailored by carefully controlling the growth conditions. The QD growth was monitored using visible/near infrared absorption spectroscopy to achieve the desired wavelength emission wavelength around 1.55 μm.

5.3.Measurements and Results

The width of the localization band and the positions of random resonators before QD deposition were measured with a 1475-1580 nm broadly-tunable laser source which was coupled laterally into the waveguide. The vertically scattered light emitted from random cavities was collected with a high-resolution objective lens and recorded with either a photodiode to obtain vertically-scattered spectra from small sections of the waveguide or with an infrared (IR) camera to obtain 2D spatially resolved spectra shown in Fig. 5.3 (a). The plot shows an approximately 40 nm-broad band filled with confined fields with various localization lengths. Note that these are random patterns, i.e. every device has a unique spectral signature and both Q-factor and localization position may vary across the pattern and from pattern to pattern. Figure 5.3 (b) shows a resolved projected spectrum collected from a 5 μm-long section of the disordered PC waveguide. The spectrum exhibits a high Q (~ 55,000) resonance near 1512 nm. Such randomly-distributed and localized

high-Q resonances are typical for random cavities based on multiple scattering feedbacks [125] [126] [127], which will be reflected in the following characterization of active devices as well.

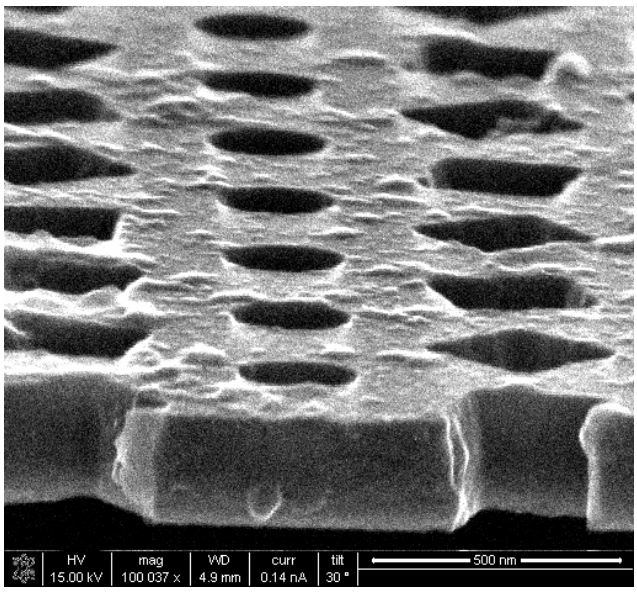

Figure 5.4: A cross section of the photonic crystal showing PbSe quantum dots embedded into photonic crystal microcavities.

To characterize active devices, colloidal PbSe quantum dots were embedded in the nanoscale air-holes comprising the line defects in disordered PCs. To maximize the density of QDs coupling with the microcavities, the samples were soaked in the PbSe QD solution for several hours. The SEM image in Fig. 5.4 shows a cross-section of the PCs embedded with PbSe quantum dots. The devices were optically excited at room temperature with a continuous wave (CW) Ti:sapphire laser operating at 810 nm. Emission from the QDs in the microcavities was focused with a high-resolution objective lens with numerical aperture of 0.7. The output spectrum was analyzed with a 0.75 m high-resolution

spectrometer and detected with an InGaAs photomultiplier tube using phase lock-in amplification. The pump light is blocked by a bandpass filter placed in front of the spectrometer. Unlike emission from the conventional, engineered PC microcavities the exact position of which is known, the output spectral characteristics for the random microcavities are sensitive to the location of the excitation. The disordered waveguides were probed systematically by scanning the focused pump-beam along the waveguide axis (x) as shown schematically in Fig. 5.5 (a). A strong dependence of excited modes' spectral characteristics on the excitation position was observed. Figure 5.5(b) shows a typical emission spectrum collected from a single excitation spot for varying excitation intensities. At lower pump intensity, the spectrum exhibits a broad spontaneous emission peak. Once the pump intensity exceeds a certain threshold, a much narrower emission peak emerges (~ 4 nm linewidth). There is a visible shoulder to the peak and hence the linewidth of the main peak might be smaller. It is also possible that multiple random resonances are being excited. The plot of the peak emission intensity versus the pump intensity (L-L), shown in Fig. 5.5(c), exhibits a threshold at ~ 100 μW. Figure 5.5(d) depicts the measured abrupt narrowing of the emission linewidth above the pump threshold. The data shown in Fig. 5.5 do not indicate lasing, but suggest the onset of coherent emission with the existence of strong feedback from random PC microcavities. Such feedback enables photon intensity around the resonance peak to quickly build up over that of the spontaneous emission.

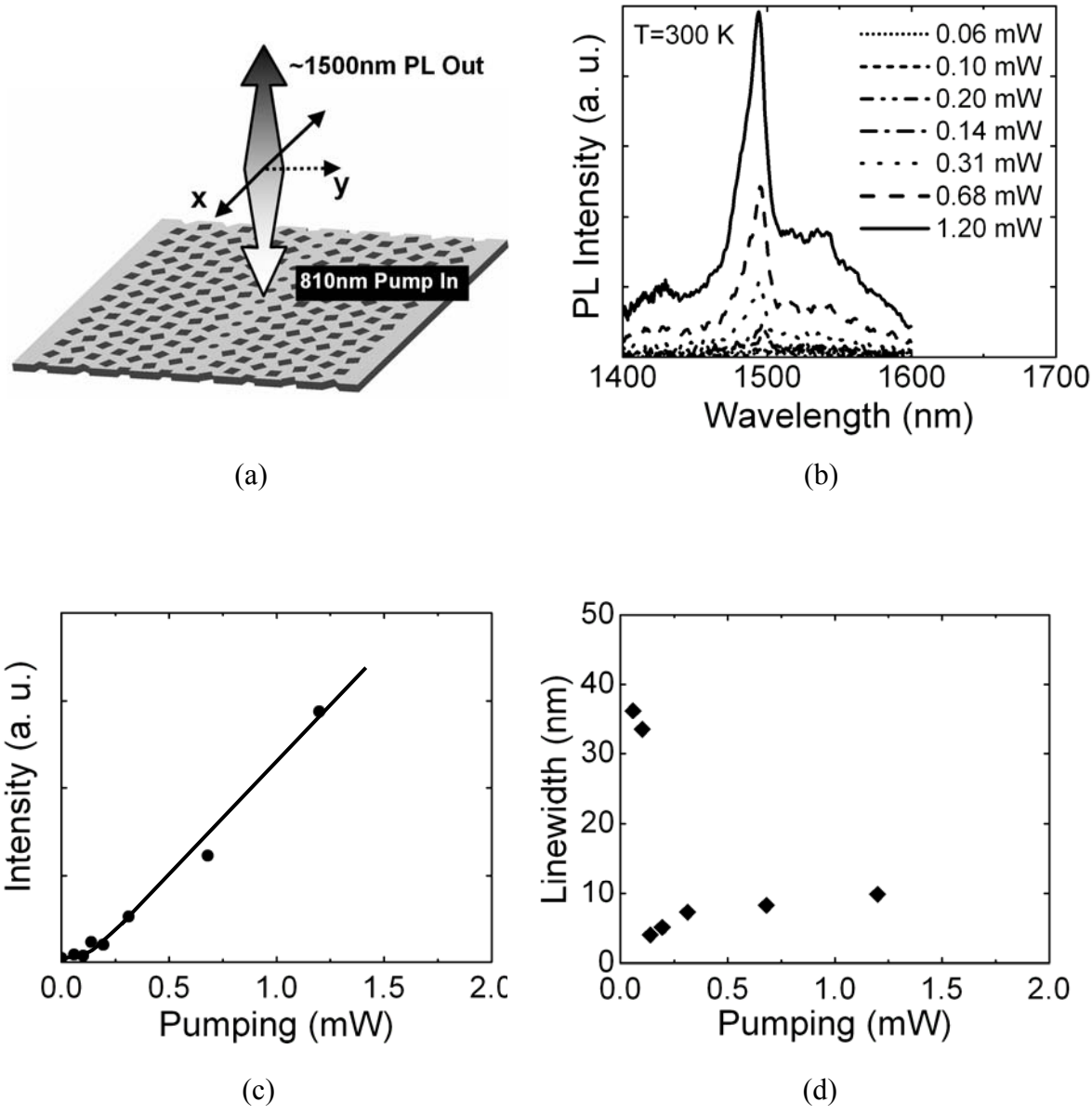

Figure 5.5: (a) Schematic of the active cavity characterization scheme, (b) emission spectra of a silicon random photonic crystal microcavity with PbSe quantum dots measured at 300K at different pump powers, (c) L-L characteristics, and (d) emission peak linewidth versus pump powers.

The observation of lasing could also be prevented by the low fill factor of the QDs in the microcavity and the resulting low modal gain in our experiment. Techniques to enhance the QD density are currently being investigated. Another important issue is the luminescence efficiency of the colloidal PbSe dots. It is observed that the efficiency is reduced, possibly due to surface contamination and oxidation, when the QDs are dried on the silicon PC microcavities. The luminescence efficiency is the highest in a sol-gel form or in a polymer matrix solution. It has also been recently demonstrated that PbS/PbSe core–shell nanocrystals are immune to degradation during the drying process [119]. The use of such dots will significantly enhance the radiative efficiency and the output intensity of the microcavity light sources. These aspects are also being undertaken.

5.4. Conclusion

A silicon-based light emitter has been demonstrated based on high-Q random cavities in disordered photonic crystal waveguides with embedded colloidal PbSe quantum dots. Emission with a minimum linewidth of 4 nm is observed. Such nanoscale light sources on silicon, with potential compatibility with complementary metal oxide semiconductor chips, could be of interest as optical interconnects in silicon photonics. It is possible, by immersing the quantum dots in a conducting polymer matrix, to eventually realize electrically injected devices.

CHAPTER 6

CONCLUSION AND SUGGESTIONS FOR FUTURE WORK

6.1. Summary of Present Work

The research described in this thesis involved a detailed study of self-organized InGaAs/GaAs quantum dot lasers directly grown on silicon substrates and their monolithic integration with guided-wave devices such as waveguides and modulators, with potential applications in chip-level optical interconnects.

Quantum dot lasers directly grown on silicon have been demonstrated for the first time. A novel dislocation reduction technique using self-organized quantum dots as a dislocation filter was proposed and its efficiency was analyzed with simulation of quasi-three-dimensional strain-dislocation interaction and with experiments including transmission electron microscopy and photoluminescence. Compared to two-dimensional strained layer superlattices, the quantum dot dislocation filter demonstrates a higher efficiency of blocking both threading dislocations and edge dislocations due to a stronger and anisotropic strain field in and around the nano-sized islands. By incorporating the optimized InAs quantum dot dislocation filter in a buffer layer, we have achieved high performance quantum dot lasers on silicon with low threshold current density (J_{th} ~ 900 A/cm^2), large

small-signal modulation bandwidth of 5.5 GHz at room temperature, a large characteristic temperature (T_0 = 278 K) and output slope efficiency of 0.4 W/A in the temperature range of 5-50 °C.

Next, the monolithic integration of the GaAs-based quantum dot laser, waveguide and the quantum well electroabsorption modulator on silicon has been demonstrated. Focused-ion-beam milling has been utilized to produce high-quality etched GaAs facets and coupling grooves. The etched facets have the reflectivity of 0.28. It is comparable to the reflectivity of 0.31 for cleaved facets, which enables quantum-dot laser comparable performance to those with cleaved facets. The laser-modulator coupling coefficient is greater than 20 % depending on the coupling-groove dimension, and the integrated quantum-well electroabsorption modulator on silicon exhibits a modulation depth of ~ 100% at 5 V reverse bias. In addition, a generalized coupling model taking into account the laser beam quality characteristics and Gouy phase shift has been developed. This model is not limited to a Gaussian light beam and more accurately describes the coupling behavior of an edge-emitting laser with a coupled waveguide. It is worthy noting that a quantitative explanation of the physical origin of Gouy phase shifts arising from diffraction effect for a general light beam has been deducted for the first time.

Additionally, the present study has demonstrated laser-waveguide integration on silicon using a lower-cost a:Si-H waveguides fabricated by plasma-enhanced-chemical-vapor deposition (PECVD). The a:Si-H waveguides exhibit a propagation loss of ~10 dB/cm for λ=1.05 μm and are expected to have much lower loss in the wavelength range of 1.3-1.55 μm. This on-chip integration approach will introduce flexibility in design and fabrication, which is important for the development of silicon photonics.

Finally, enhanced emission with a minimum linewidth of 4 nm at 1.5 μm wavelength has been observed from PbSe colloidal quantum dots embedded in a silicon-based random photonic crystal microcavity. Such microscale light sources can also be fabricated or integrated on silicon CMOS chips, and will be of interest in the application of optical interconnects.

6.2. Suggestions for Future Work

6.2.1. Integrated Quantum Dot Light Emitting Devices with Crystalline Silicon Waveguides

As discussed in Chapter 4, a:Si-H waveguides provide more flexibility in design and fabrication compared to SOI-based waveguides. However, SOI-based waveguides have lower propagation loss, especially in the wavelength range of 1.3~1.55 μm, and they are more suitable for electro-optic modulation. Crystalline Si membranes with active devices and circuits can be transferred onto other substrates by a lift-off process [128]. This technology can be extended to achieve low-loss waveguides and electro-optic modulators. Such transferred Si membrane waveguides could have the properties of SOI-based waveguides in addition to providing more flexibility in chip-scale integration.

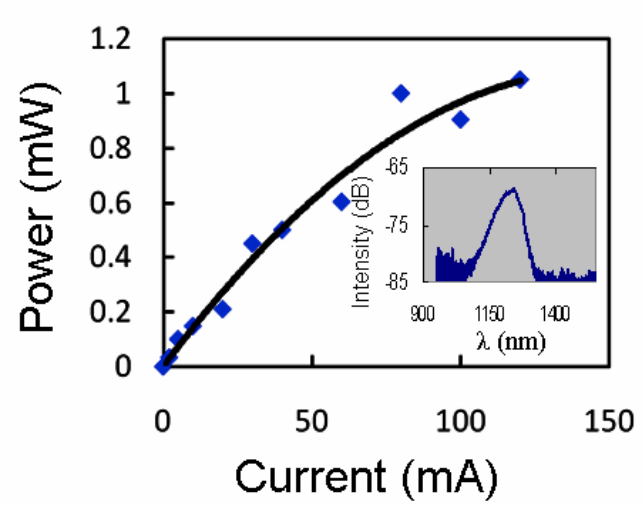

(a)

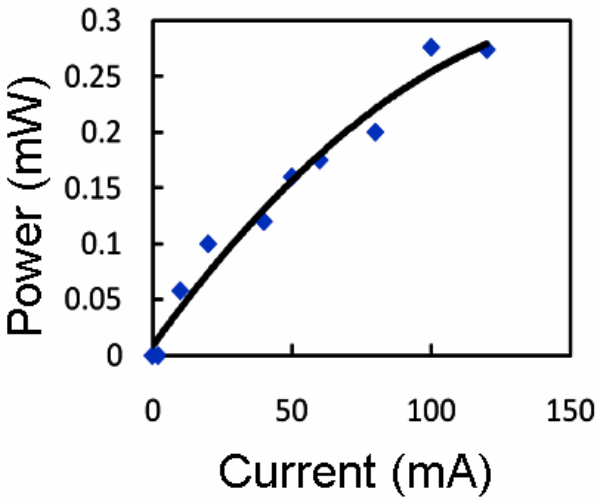

(b)

Figure 6.1: Light-current characteristics for output from (a) the InGaAs quantum dot LED, and (b) the coupled silicon waveguide, the inset is the electroluminescence spectrum.

A preliminary experimental study of a QD light emitting device (LED) integrated with a transferred Si membrane waveguide has been conducted. Si membranes with a thickness of 0.27 μm were detached from commercial SOI substrates and transferred onto specified regions of a wafer consisting of InGaAs/GaAs QD laser heterostructures. The waveguide cladding is PECVD SiO_x. The device fabrication is almost the same as de-

scribed above for the integrated laser/waveguide/modulator. Efficient optical coupling between the LED and transferred Si waveguide has been achieved, as shown in Fig. 6.1. Unfortunately, we did not achieve lasing due to oxygen contamination during MBE growth, which was detected later.

6.2.2. Integration of Quantum Dot Lasers with Silicon CMOS Transistors

The integration of III-V lasers with silicon CMOS transistors is a critical issue in silicon photonics, in terms of compatibility. To date, all III-V lasers directly grown on Si utilize offcut Si substrates in order to minimize anti-phase-domain defects resulting from the incompatibility of polar-on-nonpolar materials. So the question is whether offcut silicon can be accepted by the mature microelectronics industry. A preliminary experiment has been conducted to compare the characteristics of MOSEFET fabricated on Si and offcut Si substrates. Experiments show that the difference in MOSFET key parameters, such as mobility and transconductance, between regular Si (100) and offcut Si diminishes when the gate length is less than 1 μm as in Fig.6.2. This is because that the terrain steps on the surface of offcut silicon will not affect the device performance if the transistor gate size goes down micrometers. Therefore, offcut Si can be used for deep submicron and nanometer scale CMOS transistors, facilitating on-chip integration with QD-lasers. Another challenge in the processing of integrated III-V/silicon chips is the incompatibility in processing temperatures. For example, traditional CMOS process requires 900-1000 ºC thermoxidation for SiO_2 gate insulator and 600-650 ºC LPCVD for polysilicon gate deposition, which is much higher for GaAs or InP. Therefore, the scheme of "laser-after-gate" is preferred for the integration III-V laser and silicon CMOS chips. To introduce more

flexibility and better reliability in processing, we are currently investigating the monolithic integration of QD lasers with silicon CMOS transistors on off-cut Si substrates by using low-temperature processing with high-k dielectric materials for gate insulators. Recently, semiconductor industries such as Intel and IBM have made breakthroughs in high-k dielectric materials including HfO_2 as gate material, which makes our approach more promising.

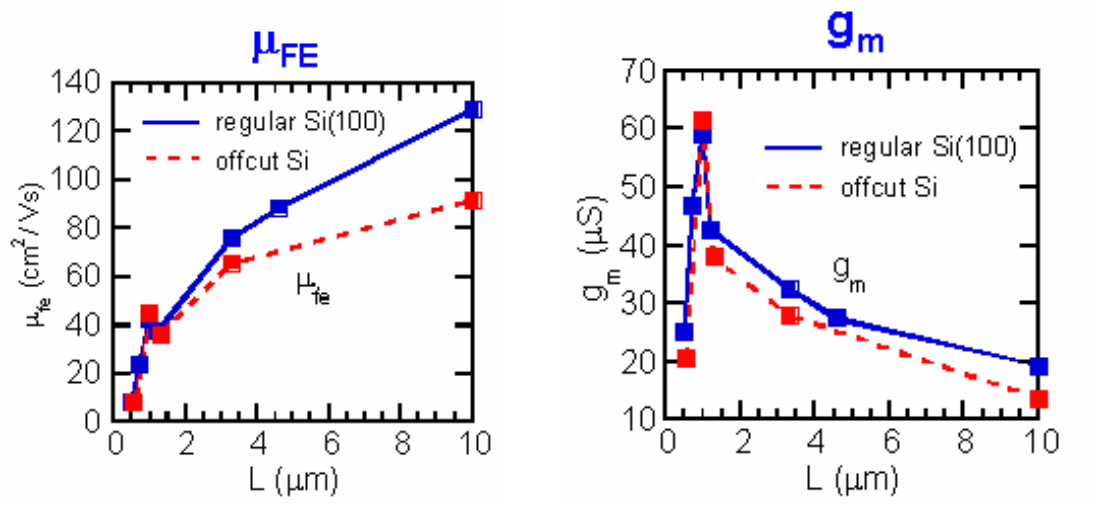

(a) (b)

Figure 6.2: The measured (a) mobility and (b) transconductance of MOSFETs, with different gate length, fabricated on regular Si (100) and offcut Si. (Courtesy of Zhenqiang Ma, University of Wisconsin, Madison)

6.2.3. WDM Array of GaAs-Based Quantum Dot Lasers

An optical transmitter based on a WDM laser array with gigabit to terabit capacity will play an important role in future optical interconnects for high-speed I/O data trans-

mission. To our knowledge, such an array has not been demonstrated with QD lasers. Quantum dot gain media have several advantages such as high gain and high differential gain which yield ultra-low threshold current and support higher modulation bandwidth with less chirp effects. Quantum dots also provide the opportunity of tuning the emission wavelength by varying the dot size and/or alloy composition during epitaxy of the heterostructure. Unfortunately, temperature stability may be a problem. The intrinsic non-uniformity of dot size can yield inhomogeneous gain broadening and support multi-wavelength lasing in a single laser with dramatically-reduced intensity nonuniformity [130]. This effect would provide QD lasers another unique application in WDM optical communications. Here, A WDM array of QD lasers, with λ~1.3-1.55 μm, low-bias, high modulation index, and chirp-free high frequency modulation, is proposed. For this application we need single-frequency tunable lasers with emission wavelength $\Delta\lambda$ apart. There are several promising ways of achieving this.

6.2.3.1. Single-Frequency DFB Quantum Dot Laser

The distributed feedback (DFB) laser provides a relatively simple technique of realizing a single-frequency laser. By varying the grating parameters, the emission wavelength can be tuned with good precision. To fabricate the WDM array, two steps of epitaxy are involved. The first-step MBE growth of the QD laser heterostructure forms the lower cladding layer, the active region and a certain thickness of the upper cladding layer. The gratings for the multiple lasers of the WDM array will then be defined by e-beam writing/UV interference lithography and etching. The grating pitch should be varied corresponding to the required $\Delta\lambda$ between different lasers in the array. The remaining upper

cladding layer and the p-contact layer of the laser will then be re-grown by MBE. Standard fabrication including optical lithography, contact metallization, wet- and dry-etching and end-facet AR coating will be used to realize the array. The processing steps are schematically shown in Fig. 6.3.

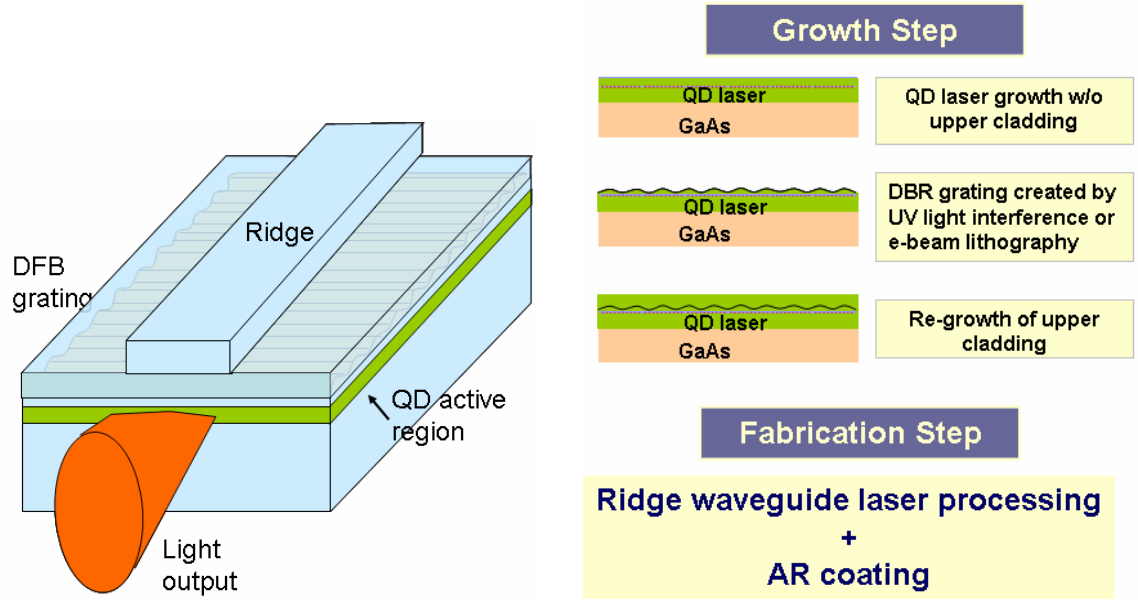

(a) (b)

Figure 6.3: (a) Illustration of DFB laser structure; (b) DFB laser growth and fabrication steps.

6.2.3.2. Widely Tunable Laser Arrays

The DFB lasers described above are fixed in frequency. It may be desirable that the elements of the WDM array are tunable. Wide tunability (50-60 nm tuning range) is achievable by active electronic tuning, an example of which is the sampled-grating distributed Bragg reflector (SGDBR) laser [131]. The proposed laser heterostructure and design are schematically shown in Fig. 6.4. The laser operates on the vernier mirror tun-

ing concept. The sampled-grating design uses two different multi-element mirrors to create two reflection combs with different wavelength spacings. The laser operates at a wavelength where the reflection peak from each mirror coincides. For electronic tuning, one mirror is tuned (by current) with respect to the other. A fourth phase section is sometimes included to fine-tune the mode location to access exact wavelength values. Tunable lasers using QD active regions will provide additional advantages of large and spectrally wide gain.

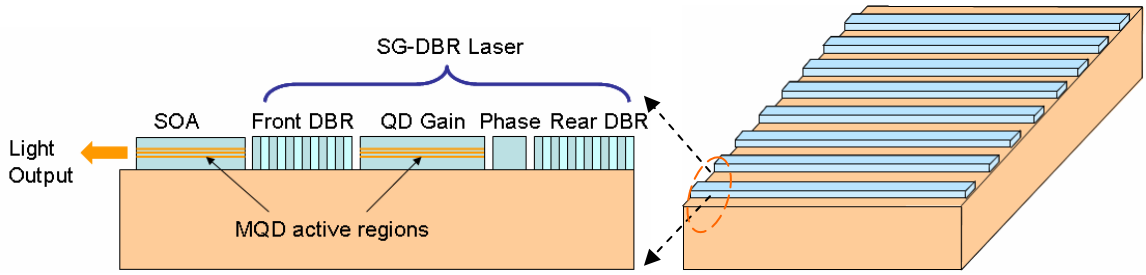

Figure 6.4: Illustration of sampled-grating DBR (SGDBR) with integrated SOA.

APPENDICES

A. DISLOCATION GLIDE VELOCITY IN LATTICE-MISMATCHED SYSTEMS

The light-emitting device degradation related to dislocation motion is discussed. For comparison, we estimate dislocation glide velocities in typical lattice-mismatched material systems including GaAs/Si, GaSb/Si, InP/Si, and GaN/sapphire.

The dislocation glide motion in semiconductors is dominated by the Peierls mechanism. Thus, the dislocation glide velocity V_d is determined by the applied shear stress $\Gamma = \tau/\tau_0$ and the dislocation mobility μ [47], namely,

$$V_d = \Gamma\mu, \quad \text{where } \mu = V_0 \exp(-E_d/kT). \tag{C-1}$$

Here, E_d is the activation energy of dislocation motion, T is the temperature, $V_0 \sim 10^6$ cm/s and $\tau_0 \sim$ 1MPa. In this study, only the order magnitudes of dislocation mobility and velocity are estimated. The E_d of several III-V compounds have been measured by many researches, as listed in Table A.1. The applied shear stress (τ) can be caused by misfit strain, thermal strain, and external mechanic strain. Here, we only consider the affect of misfit strain, which is determined by Peach-Koehler force equation as follow:

$$\vec{\tau} = \left(\hat{b} \cdot \vec{\sigma}\right) \times \hat{l}, \tag{C-2}$$

where $$\vec{\sigma} = \begin{pmatrix} \sigma_{\parallel} & 0 & 0 \\ 0 & \sigma_{\parallel} & 0 \\ 0 & 0 & 0 \end{pmatrix}$$

is the stress tensor, and $\sigma_{\parallel} = \dfrac{Y}{1-\nu}\varepsilon_{\parallel}$ is the in-plane stress related to Youngs modulus of elasticity (Y), Poisson ratio (ν), and in-plane strain ($\varepsilon_{\parallel}$). $\hat{b}$ and $\hat{l}$ is the unit vector for Burgers vector and dislocation line, respectively. For zinc-blende-structure material such as GaAs, GaSb and InP, the 60°-misfit dislocations are the most common. Assume Bur-

gers vector $\hat{b} = [\bar{1}01]/\sqrt{2}$ and line direction $\hat{l} = [110]/\sqrt{2}$, the magnitude of misfit stress is

$$\tau = \left|\left(\hat{b}\cdot\vec{\sigma}\right)\times\hat{l}\right| = \sigma_{\parallel}/2 = \frac{Y}{2(1-v)}\varepsilon_{\parallel}. \tag{C-3}$$

For wurzite-structure GaN, for simplicity, the worst case that the dislocations are in-plane (parallel to the interface) is assumed. Thus the magnitude of misfit stress

$$\tau = \sigma_{\parallel} = \frac{Y}{(1-v)}\varepsilon_{\parallel} \tag{C-4}$$

According to Eqs.(C-1), (C-3), and (C-4), misfit stress and dislocation glide velocity can be estimated, the results are listed in Table C.1

Table C.1: Comparison of dislocation glide velocity of GaAs, InP, GaSb on Si, and GaN on sapphire at 300K.

Material system	Lattice mismatch	Youngs modulus (*GPa*)	Band gap (*eV*)	Poisson ratio (*v*)	E_d (*eV*)	τ (*GPa*)	V_d (*μm/Year*)
GaAs/Si	4%	85.9	1.424	0.31	~1.25	2.5	1~5
InP/Si	8%	61.1	1.344	0.36	~1.2	3.8	10
GaSb/Si	12%	63.1	0.726	0.31	~1.2	5.5	15
GaN/Sapphire	16% (30°-rotation)	181	3.2	0.35	~2.1	44.6	1×10^{-13}

** part of data from "semiconductors on NSM" via http://www.ioffe.rssi.ru/SVA/NSM/Semicond/*

From the calculations, we found the material with wider bandgap and larger Youngs modulus prefer to slower dislocation motion. It is note that dislocation/defect glide velocity in GaAs (GaSb, InP) will be dramatically enhanced by a factor of 10^8-10^{10} under current injection, for example of 100 A/cm^2, due to the recombination enhancement effect of dislocation motions. However, such effect is not dominant in GaN-based materials. These

can explain why the hybrid GaAs(GaSb, InP)-on-Si light emitting devices (LEDs) suffer from fast degradation, while GaN-on-sapphire LEDs has little degradation in spite of high densities of dislocations ($>10^8$ cm^{-2}).

B. CHIRP AND α-PARAMETER IN QUANTUM DOT LASERS

The main difference of semiconductor lasers from conventional atomic lasers is the former has high density of state and refractive index modified by injection carriers. The dependence of refractive index on injection carriers makes semiconductor laser have far broader linewidth than atomic laser does. The linewidth Δν of a single longitudinal laser mode with output power P_{mode} from a single facet is given by [112]

$$\Delta\nu = \Delta\nu_0 + \frac{\upsilon_g \gamma_m h\nu}{8\pi} \frac{R_{sp} V_{ca}}{P_{\mathrm{mod}e}} (1+\alpha^2) \tag{B-1}$$

where $\Delta\nu_0$ is the power-independent linewidth, υ_g is the group velocity of photons, γ_m the mirror loss, R_{sp} is the spontaneous emission rate, V_{ca} is the active region volume, and the linewidth enhancement factor α is given by [112]

$$\alpha = -\frac{4\pi}{\lambda} \frac{\partial n_r / \partial n}{\partial g / \partial n} \ . \tag{B-2}$$

Here n_r is the the refractive index, n is the injection carrier density, $\partial g / \partial n$ is the differential gain.

The effect of refractive index modified by injection carriers also induces lasing wavelength shifting, i.e. frequency chirping, during the direct modulation of semiconductor laser. QD laser has very high differential gain $\partial g / \partial n$, which results in α-parameter of nearly zero. These are strongly related to the direct modulation characteristics, and chirp effect should be dramatically suppressed in quantum dot lasers.

Under small signal conditions, the modulation-resonance frequency is [112]

$$\omega_r \sim \left(\frac{c\bar{\varphi}\Gamma \partial g_r / \partial n}{n_r \tau_p} \right)^{1/2}, \tag{B-3}$$

where c is the velocity of light, $\bar{\varphi}$ is the average photon density, Γ is the modal confinement factor , and τ_p is the photon cavity lifetime. So high differenetial gain yields large modulation-resonance frequency.

C. SEMICONDUCTOR LASER DESIGN

A typical bipolar semiconductor laser is a p-i-n diode. Under forward bias, electrons in the conduction band and holes in the valence band are injected into the intrinsic region, namely, active region, from the n-doped and p-doped regions, respectively. Then electrons and holes recombine in the active region to convert to photons. With an optical cavity, laser action takes place under the balance between gain and loss. In bulk semiconductor lasers, a double heterostructure (DH) is usually used to confine carriers and photons in the same region to enhance the interaction of carriers and photons. An important performance characteristics of semiconductor lasers is the threshold current which is described by $J_{th}=eN_{th}d/\tau_c$ according to the two-level system approximation [112][132], where e is the electron charge, d is the active region thickness, τ_c is the carrier lifetime, and N_{th} is the threshold density of injected carriers. Therefore, Minimization of the threshold current can be realized by reducing active region dimension and threshold carrier density, or increasing carrier lifetime. First, these can be realized through the development of quantum-confined heterostructures including quantum wells (QW), quantum wires (QWire), and quantum dots (QD) with higher density of state (DOS) and separate energy levels, which significantly reduce the threshold carrier density as well as active region dimension. Next, especially in QW lasers, the development of band engineering reduces effective mass of holes by using strained heterostructures to decouple light holes and heavy holes, which enhances gain and differential gain. Also, the development of microcavity with high Q-factor produces small modal volume and less cavity loss as well as squeezes the total spontaneous recombination (increase τ_c), which even yields thresholdless lasing. Moreover, the development of various novel laser structures such as the tun-

neling-injection scheme increases injection efficiency (increase τ_c) by minimizing non-radiation loss such as leakage current and thermal effect related to hot carrier effect and Auger recombination. It is worthy noting that, in QW and QD lasers, a separate confinement heterostructure (SCH) instead of DH is usually used to efficiently confine both photons and carriers. In a SCH structure, carriers are confined in a quantum-sized active region (QW or QD), while photons are confined within a wavelength-scale waveguide region.

In addition to threshold current, the improvement of other important performance characteristics including modulation bandwidth and output power have also been extensively investigated. Some design schemes are discussed as follows.

High-speed laser design —— To design a high-speed laser with low chirp, a number of parameters have to be optimized. It requires high differential gain and photon density (see Appendix B), short carrier transport time, less gain compression, and small device size and parasitics, etc [112][132]. The use of lower-dimension quantum-confined heterostructures such as QWs, QWires, and especially QDs as active regions will significantly enhance differential gain. The introducing of strain in QWs can further increase differential gain due to the removal of degeneracy of light and heavy holes. The use of p-doping has also been demonstrated to enhance differential gain, which is discussed in Section 1.3.3. A narrower SCH will enhance the modulation bandwidth due to shorter carrier-transport time [132]. On the other hand, hot carrier effect can induce gain compression and consequently degrade the differential gain. In addition, carriers captured or preferably occupying in barriers, wetting layer and non-lasing excited states, especially in QDs with unique phonon bottleneck effect, can drastically limit the high-speed operation

of lasers. These problems can be significantly alleviated by using the tunneling-injection scheme, which is discussed in detailed in Section 1.3.3.

High-power laser design —— The output power of a semiconductor laser is typically limited by several factors such as multimode operation, catastrophic optical degradation (COD), thermal rollover, and temperature-dependent operation. Multimode-operation, the onset of higher-order spatial modes, will degrade wall efficiency of the output power. It exhibits discontinuities or kinks in light-current characteristics. Multimode operation can also degrade beam quality and enhance the formation of filamentation under high-level injection. Maintaining single mode in vertical direction can be realized by careful design of ridge-waveguide cavities, while single mode in lateral direction can be achieved by using tapered or curved ridge-waveguides [133]. The second limitation, COD, mainly refers to cavity facet damage due to high-optical-power-caused heating. The critical COD power density is ~1-5 MW/cm^2 for an uncoated AlGaAs facet. Facet coating and passivation techniques can increase the value to ~10-20 MW/cm^2 [132]. Broad aperture design is a typical technique to increase output power under a specific COD limit. In addition, an Al-free waveguide region is helpful to increase this critical COD power density [134]. The third limitation, thermal rollover, is caused by drastic gain compression due to thermal heating, current leakage, and hot carrier effects [112][132]. The light-current characteristic curve shows that under high injection current the wall efficiency decreases and eventually the output power saturates and even decreases. Such heating effect can be minimized by using uniformly-distributed bonding of contact wires, and p-side-down mounting with special thermal-conducting solders such as AuSn, Cu-W, or Cu-diamond [135]. The fourth limitation can be described by the dependence of

threshold current on temperature, which is characterized by T_0 through the relation $J_{th}(T)=J_{th}(0)exp(T/T_0)$. T_0 can be significantly increased by using the QD heterostructures as active region and p-doping technique.

D. REVISITING PHYSICAL ORIGIN OF GOUY PHASE SHIFT

In this section, a generalized refractive index that includes diffraction effects has been used to show that the Gouy phase shift can be seen as an intensity-averaged optical path difference between the generalized eikonal and the geometrical eikonal. This approach generalizes previous treatments to include the effects of phase distortion and confirms the role of transverse spatial confinement in the Gouy shift. In particular, for the first time a quantitative formula directly from wave equation has been derived for evaluating the evolution of Gouy phase shift for a general light beam. This formula, under the paraxial approximation, provides the estimation of Gouy phase shift from the beam quality M^2 factor, beam size and transmission matrices.

In 1890 Gouy observed an optical beam passing through its focus experiences an additional axial phase shift with respect to a plane wave [100], and further showed this phase anomaly exists for acoustic waves as well [101], and in fact, for all waves with transverse spatial confinement. The Gouy phase shift plays a significant role in wave phenomena, especially in optics. It accounts for the existence of phase advance for Huygens wavelets, the dependence of the resonator frequency on transverse modes in laser resonator [102], the formation of trapping force in laser tweezers technology [136]. In nonlinear optics the efficiency of high-order harmonic generation with focused beams is affected by the Gouy phase shift as well [137]. Recently, it was shown that the Gouy phase shift strongly affects the temporal-spatial evolution of focused few-cycle electromagnetic pulses [138] [139] [140]. Such phenomena have also been observed in acoustic pulses [141]. Because of the importance of the Gouy phase shift, many efforts have been made to try to give a clear physical explanation of it based on diffraction theory and topo-

logical Berry phase, *etc.*. The complexity of these theories makes explanation far from the nature of Gouy phase shift. More detailed comments can be found in Refs. [103] and [104]. More intuitive explanations of physical origin of Gouy phase shifts were given in terms of the geometrical properties of Gaussian beams [103], the transverse momentum spreading [104], and the geometrical quantum effect via the uncertainty principle [105]. The latter two propose that the Gouy phase shift arise as a wave is transversely confined. Unfortunately, Boyd's model [103] only yields approximate predictions and fail to properly describe the Gouy phase shift for cylindrical focusing. Quantum explanation [105] appears unconvincing for classical waves, e.g. acoustic waves. Feng and Winful's work is mainly based on a priori definition (see Eq.(3) in Ref.[104]) verified with Hermite-Gaussian beams, which will be shown here valid only for distortion-free paraxial beams.

Here an intrinsic explanation of the origin of Gouy phase shift is given on the basis of a generalized eikonal equation and the intensity moments theory. We start with the wave equation in ABCD system and strictly prove a general expression of the Gouy phase shift for paraxial beams and extend to non-paraxial cases. We have shown the total axial phase shift, including the Gouy phase shift and the intensity-averaged phase distortion with respect to the effective spherical wavefront, is determined by the intensity-averaged optical path difference between the generalized eikonal and the classical geometrical eikonal, owing to the spatial transverse confinement of finite beam itself. We have developed an intuitive geometrical picture for the origin of Gouy phase shifts which combines diffraction effects and geometrical properties of beams, and clarified the nature of Gouy phase shifts with exact quantitative derivations.

Consider a monochromatic wave field $\vec{E}(r,z)$ with frequency ω, which satisfies vector wave equation [142]

$$\nabla^2\vec{E}+\nabla\left(\vec{E}\cdot\frac{\nabla\varepsilon}{\varepsilon}\right)+n^2k^2\vec{E}=0\,. \tag{D-1}$$

Here wave number $k=\omega/c$, c is the speed of light in free space. $n=\sqrt{\varepsilon/\varepsilon_0}$ is the refractive index, and ε (ε_0) is the dielectric permittivity (in free space). For most interesting cases in which the change of ε over the distance of one wavelength is much less than ε itself, the second term in Eq. (D-1) can be ignored and wave equation Eq. (D-1) reduces to scalar Helmholtz equation

$$\nabla^2E+n^2k^2E=0 \tag{D-2}$$

Take $E(\vec{r},z)=\widetilde{E}(\vec{r},z)\exp\left(ik\widetilde{L}(\vec{r},z)\right)$, where the amplitude $\widetilde{E}$ and the eikonal $\widetilde{L}$ are real. By substituting it into Eq. (D-2) and separating the real and imaginary parts, one gets [143][144]

$$\left(\nabla\widetilde{L}\right)^2=n^2+\frac{1}{k^2}\frac{\nabla^2\widetilde{E}}{\widetilde{E}}\equiv n_G^2\,, \tag{D-3}$$

$$\nabla\cdot\left(\widetilde{E}^2\nabla\widetilde{L}\right)=0\,. \tag{D-4}$$

Eq. (D-3) is the generalized-eikonal equation involved both in geometry and wave, which reduces into the classical geometrical eikonal equation $\left(\nabla\widetilde{L}\right)^2=n^2$ by taking the limit $k\to\infty$ ($\lambda\to0$). So n_G can be viewed as the generalized refractive index for spatial-confinement optical wave [143] [144]. It is easily found that the Poynting vector $\vec{S}=\mathrm{Re}[\vec{E}\times\vec{H}^*]/2=\widetilde{E}^2\nabla\widetilde{L}/2c$ (assume permeability $\mu=1$) [145], so the direction of rays defined as $\nabla\widetilde{L}$ follows the energy flow everywhere. Consequently, Eq. (D-4) be-

comes the continuity equation for stationary electromagnetic field, i.e. $\nabla \cdot \vec{S} = 0$ which indicates the conservation of energy flow. n_G is the effective refractive index that local optical field of a finite beam can experience and then follow the familiar laws of ray optics, while the conventional definition of the refractive index holds only for infinite beams such as plane wave and spherical wave. Thus we can still trace rays for finite beams. These rays do follow the trajectories determined by the eikonal Eq. (D-3) not by the classical geometrical eikonal.

Many practical applications involve paraxial optical systems with the refractive index $n^2 = n_0^2 - n_0 n_2 (x^2 + y^2)$, which is described by ABCD matrices with

$$\begin{pmatrix} A & B \\ C & D \end{pmatrix} = \begin{pmatrix} \cos(n_2/n_0)^{1/2} z & (n_0 n_2)^{-1/2} \sin(n_2/n_0)^{1/2} z \\ -(n_0 n_2)^{1/2} \sin(n_2/n_0)^{1/2} z & \cos(n_2/n_0)^{1/2} z \end{pmatrix} \tag{D-5}$$

Writing field as $E(\vec{r}, z) = E_0(\vec{r}, z)\exp(in_0 kz)$ and following slowly varying envelope and paraxial approximation $\left|\partial^2 E_0/\partial z^2\right| << \left|\nabla_\perp^2 E_0\right|$, $\left|2kn_0 \partial E_0/\partial z\right|$ [102], we get paraxial wave equation

$$\nabla_\perp^2 E_0 + 2ikn_0 \partial E_0/\partial z + k^2(n^2 - n_0^2)E_0 = 0\,. \tag{D-6}$$

And taking the slowly varying amplitude $E_0(\vec{r}, z) = \psi(\vec{r}, z)\exp(ikL(\vec{r}, z))$, we separate the real and imaginary parts to get the eikonal equation and continuity equation, similar as Eqs. (D-3) and (D-4) but in the paraxial approximation, namely

$$(\nabla_\perp L)^2 + 2n_0 \frac{\partial L}{\partial z} + n_0^2 = \frac{1}{k^2}\frac{\nabla_\perp^2 \psi}{\psi} + n^2 \equiv n_G^2\,, \tag{D-7}$$

$$\nabla_\perp \cdot (\psi^2 \nabla_\perp L) + n_0 \frac{\partial \psi^2}{\partial z} = 0\,. \tag{D-8}$$

A general beam (not necessarily Gaussian) can be characterized in terms of certain average quantities with respect to its intensity distribution. These beam parameters are intensity moments of the form $\langle a \rangle = \int a \psi^2 dxdy$ (assuming the field has been normalized) and include the beam size $W_{r=x,y}^2 = 4\langle r^2 \rangle$ and the effective radius of curvature $R_{r=x,y} = \langle r^2 \rangle / \langle r \partial L / \partial r \rangle$ [107] [108]. Another quantity is the beam quality factor $M_{r=x,y}^2 = kW_{r0}\theta_r$ where W_{r0} is the beam size on the waist plane and θ_r is the beam far-field divergence. To see how the Gouy shift arises for this general beam we take an intensity-average over all the terms in Eq. (D-7), and then use the following relation which is a generalization of an invariance proven by Belanger [107]

$$\left\langle (\nabla_\perp L)^2 \right\rangle - \frac{1}{k^2} \left\langle \frac{\nabla_\perp^2 \psi}{\psi} \right\rangle = \sum_{r=x,y} \left(\frac{M_r^4}{k^2 W_r^2} + \frac{W_r^2}{4R_r^2} \right) \equiv \sum_{r=x,y} \theta_r^2 \,. \tag{D-9}$$

With this relation Eq. (D-7) reduces to

$$2n_0 \left\langle \frac{\partial L}{\partial z} \right\rangle = -\sum_{r=x,y} \left(\frac{M_r^4}{k^2 W_r^2} + \frac{W_r^2}{4R_r^2} + \frac{n_0 n_2 W_r^2}{4} \right). \tag{D-10}$$

For general paraxial beams, we can expand the phase L in a Taylor's series

$$kL = \sum_{r=x,y} kr^2 / 2R_r + \Phi_a(x,y,z) + \Phi_G(z). \tag{D-11}$$

Here, the zero-order term $\Phi_G(z)$ is independent of the transverse variables and the higher-order terms $\Phi_a(x,y,z) = \sum \left(c_m x^m + c_{pq} x^p y^q + c_n y^n \right)$ can be viewed as phase distortion with respect to effective spherical wavefront. Following intensity moments transformation [107] [108], we have

$$2n_0 \left\langle \frac{\partial}{\partial z} \left(\frac{r^2}{2R_r} \right) \right\rangle = \frac{M_r^4}{k^2 W_r^2} - \frac{W_r^2}{4R_r^2} - \frac{n_0 n_2 W_r^2}{4} \,. \tag{D-12}$$

Substituting Eq.(D-11) into (D-10) and using Eq. (D-12), we get

$$n_0\left\langle\frac{\partial\left(\Phi_a+\Phi_G\right)}{\partial z}\right\rangle=-\sum_{r=x,y}\frac{M_r^4}{kW_r^2}. \tag{D-13}$$

Combination of Eqs. (D-13) with (D-9) leads to

$$\frac{\partial\Phi_G}{\partial z}+\left\langle\frac{\partial\Phi_a}{\partial z}\right\rangle=\frac{1}{n_0k}\left\langle\frac{\nabla_\perp^2\psi}{\psi}\right\rangle-\frac{k}{n_0}\left(\left\langle\left(\nabla_\perp L\right)^2\right\rangle-\frac{W_r^2}{4R_r^2}\right). \tag{D-14}$$

Using the continuity equation (D-8) and the intensity moments, we can obtain an equation of motion for the moment $\partial\left\langle x^p y^q\right\rangle/\partial z=n_0^{-1}\left\langle px^{p-1}y^q\,\partial L/\partial x+qx^p y^{q-1}\,\partial L/\partial y\right\rangle$ (*p, q* are integers). Thus Eq. (D-14) reduces to

$$\frac{\partial\Phi_G}{\partial z}+\frac{\partial\left\langle\Phi_a\right\rangle}{\partial z}=\frac{1}{n_0k}\left\langle\frac{\nabla_\perp^2\psi}{\psi}\right\rangle, \tag{D-15}$$

Integrating and using properties of the Fourier transform, we get

$$\Phi_G(z)+\left\langle\Phi_a(z)\right\rangle=\int_0^z\frac{1}{n_0k}\left\langle\frac{\nabla_\perp^2\psi}{\psi}\right\rangle dz'=-\int_0^z\frac{\left(\left\langle k_x^2\right\rangle+\left\langle k_y^2\right\rangle\right)}{n_0k}dz' \tag{D-16}$$

where k_x, k_y are the wave vector components of real amplitude along x, y axes. We see that there are two contributions to the axial phase shift. The first is the Gouy shift and the second is an intensity-averaged phase distortion with respect to the effective spherical wavefront. Both shifts are induced by diffraction owing to the transverse spatial confinement of finite beams. The transverse Laplacian on the nonuniform field $\nabla_\perp^2\psi/\psi$ in the wave equation represents the effect of diffraction which indicates transverse momentum spreading $\left\langle k_x^2\right\rangle$, $\left\langle k_y^2\right\rangle$. The relation of the Laplacian to the Gouy phase shift has been mentioned qualitatively by Siegman [102].

By using Eq. (D-7), Eq. (D-16) becomes

$$\Phi_G(z) + \langle \Phi_a(z) \rangle = n_0^{-1} k \int_0^z \langle n_G^2 - n^2 \rangle dz', \tag{D-17}$$

which reminds one of an expression for optical path difference. Inasmuch as the diffraction effect induces the phase shift, it is the point to figure out the optical path difference between the real trajectory and the geometrical ray trajectory in terms of $n_G dS - nds$, as shown in Fig. D.1. Here dS is the real path (energy flow) the ray follows as it experiences the refractive index n_G, and ds is the geometrical optics path the ray follows without consideration of diffraction when the beam propagates a distance of dz. Using ray equation under the paraxial approximation and the fact that $\nabla_\perp^2 \psi / k^2 \psi << n$, we have $n_G dS - nds \approx \left(\nabla_\perp^2 \psi / n_0 k^2 \psi\right) dz = n_0^{-1} \left(n_G^2 - n^2\right) dz$, where $n_G \approx \left(n + \nabla_\perp^2 \phi / 2 n_0 k^2 \phi\right)$, $dS \approx [1 + (dX/dz)^2 / 2 + (dY/dz)^2 / 2] dz$, $ds \approx [1 + (dx/dz)^2 / 2 + (dy/dz)^2 / 2] dz$. As a consequence, Eq. (D-17) is just the paraxial approximation of the following relation

$$\Phi_G(z) + \langle \Phi_a(z) \rangle = k \int_0^z \langle n_G dS - nds \rangle \tag{D-18}$$

The result reveals that the total axial phase shift is just the intensity-averaged optical path difference between $n_G dS$ and nds. As shown in Fig. D.1, at a point P, if a ray will follow different paths dS and ds when the beam propagates a distance of dz, there exists an optical path difference between the two trajectories. Consider a bundle of rays filling the whole beam with the intensity weight, we get the total phase shift $k \int\int_{-\infty}^{+\infty} dx dy \psi^2(x, y) \left(n_G dS - nds\right)$ within z and $z + dz$. As mentioned above, the optical path difference is a consequence of the diffraction effect of finite beam, which causes Gouy phase shift and intensity-averaged phase distortion. Without distortion, such phase

shift appears solely as the Gouy phase shift. In principle, the Gouy phase shift developed by the beam exhibits the propagation behavior of light as a wave phenomenon rather than geometrical rays. Far from the focus or aperture, the beam looks more like rays and the Gouy phase shift is trivial; while close to focus or aperture, strong transverse confinement makes wave effect and Gouy phase shift significant. Such expression in terms of optical path difference gives an intuitive picture of the Gouy phase shift as a correction of wave propagation to geometrical optics rays.

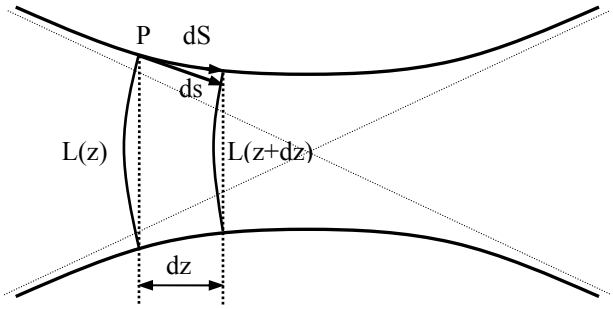

Figure D.1: A focused light beam with wavefront and path at point P, where dS is the real ray path with the generalized refractive index n_G and ds the imaginary geometrical path with the classical refractive index n.

For distortion-free beam, an analytical expression for Gouy phase shifts in ABCD systems is derived from Eq. (D-13)

$$\Phi_G = -\sum_{r=x,y} \frac{M_r^2}{2} \tan^{-1}\left(B \Big/ \left(A + \frac{B}{R_{1r}} \right) \frac{\pi W_{1r}^2}{\lambda M_r^2} \right) \tag{D-19}$$

where W_{1r} and R_{1r} are the beam size and the radius of the effective wavefront on the input plane, respectively. If the input plane lies on the waist plane, we have

$$\Phi_G = -\sum_{r=x,y} \left(M_r^2/2\right) \tan^{-1}\left(B/Az_r\right), \tag{D-20a}$$

$$\Phi_G = -\sum_{r=x,y} \left(M_r^2/2\right) \tan^{-1}\left(z/z_r\right) \quad \text{(in free space)}, \tag{D-20b}$$

where the Rayleigh range is $z_r = \pi W_{0r}^2 / \lambda M_r^2$.

In conclusion, from wave equation via the generalized eikonal and intensity moments, it is confirmed that the physical origin of the Gouy phase shift is the spatial confinement of finite beams. The Gouy phase shift can be expressed as the intensity-averaged optical path difference caused by diffraction effect. Moreover, it can be shown that the expression of the phase shift in terms of the optical path difference [Eq. (D-18)] is valid or extended for spatial solitons and non-paraxial beams such as stable Gaussian modes. Such a geometrical picture based on the wave equation makes it clear that the result we derived applies not only to electromagnetic waves but also to acoustic wave propagation.

E. PROCESS OF QUANTUM DOT LASERS AND THEIR INTEGRATION WITH ELECTROABSORPTION MODULATORS ON SILCION

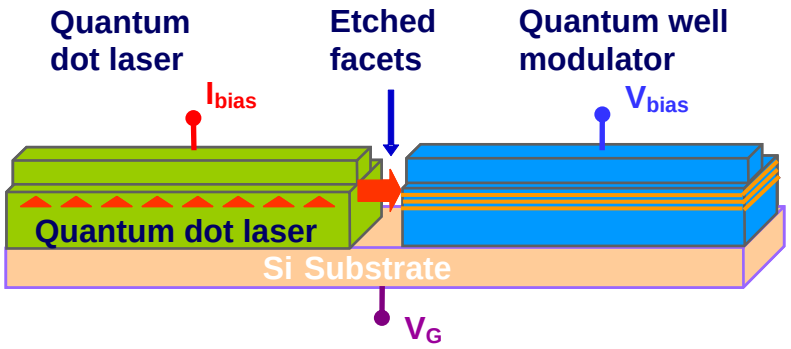

(a)

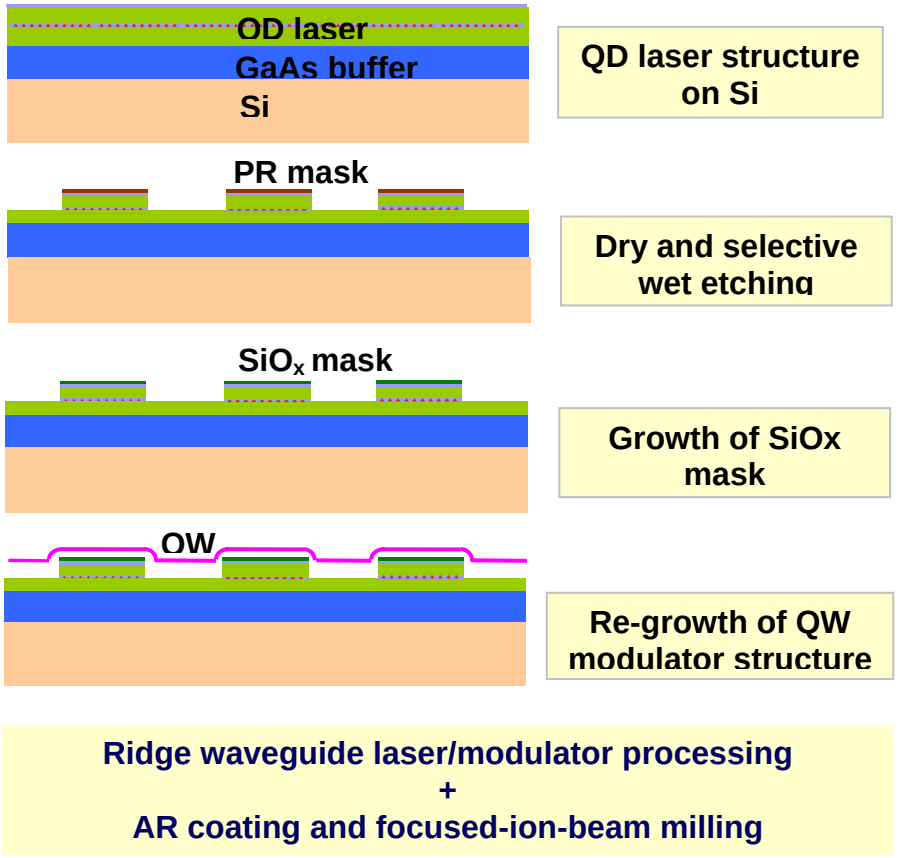

(b)

Figure E.1 (a) Scematic and (b) processing flow for the integrated quantum dot laser and quantum well electroabsorption modulator on silicon

Schematic and process flow of the groove-coupled integrated QD laser and QW electroabsorption modulator are illustrated in Fig. E. 1. The following is the recipe for device growth and fabrication.

I. Quantum Dot Laser Growth and Quantum Well Modulator Regrowth

---

1. Quantum Dot Laser MBE Growth

1.1. Oxide dissolve: 2×1 RHEED pattern occurs at 600 °C

1.2. GaAs, n-cladding AlGaAs, and p-cladding AlGaAs growth at 600 °C, 625 °C, 610 °C, respectively, growth rate 2 Å/sec

1.3. InGaAs QD grown at 500 °C, growth rate ~0.6-0.7 A/sec
InAs QD grown at 510 °C, growth rate ~0.15-0.2 A/sec, cover by 50 Å $In_{0.15}Ga_{0.85}As$

---

2. Trench Patterning and Etching

2.1. Lithography
Solvent clean: warm Acetone, IPA
Dehydrate bake: 2 min @ 130 °C hotplate
Resist coating: HMDS, SC1827 @ 4 krpm, 30 sec
Pre-bake: 1 min @ 105 °C hotplate
Exposure: 12~12.5 sec (vacuum/or hard contact)
Resist development: AZ 351 : DI H_2O = 1 : 5, 45 sec;
DI H_2O rinse 3 min
De-scum (plasma ashier): 1 min, 80 W, 250mTorr, 17% O_2

2.2. Etching:
ICP dry etching (LAM): Cl_2 : Ar=2.6 : 11.6 sccm, 2 mTorr,
TCP power=300 W, Bias power=36 W
Wet etching of AlGaAs: BHF

2.3 SiO_x protection layer deposition

PECVD: 200 °C, PECVD, 0.15-0.2 μm

2.4 Open trenches:

Solvent clean: warm Acetone, IPA
Dehydrate bake: 2 min @ 130 °C hotplate
Resist coating: HMDS, SC1813 @ 4 krpm, 30 sec
Pre-bake: 1 min @ 105 °C hotplate
Exposure: 6-6.5 sec (vacuum/or hard contact)
Resist development: AZ 319, 25-35 sec;
DI H_2O rinse 3 min
De-scum (plasma ashier): 1 min, 80 W, 250mTorr, 17% O_2
Wet etch: BHF, etch rate~100 Å/sec

---

3. MBE Regrowth of Quantum Well Modulator

3.1. Oxide dissolve: 2×1 RHEED pattern occurs at 600 °C

3.2. GaAs, n-cladding AlGaAs, and p-cladding AlGaAs growth at 600 °C, 625 °C, 610 °C, respectively, growth rate 2 Å/sec

3.3. InGaAs QW grown at 500 °C, thickness~70-80 Å

---

4. Indium Removal

4.1. Indium removal:

$HgCl_2$/dimethlyformamide solution with ultrasound

4.2. Lapping:

Backside planarization using 9 μm alumina grit

4.3. Solvent clean:

Xylenes (hot solution ready): >30 min 105 °C hotplate
Acetone: 10 min, warm
IPA: 10 min

---

5. Removal of Overgrown GaAs/AlGaAs on the Laser Region Surface

5.1. Lithography
Solvent clean: warm Acetone, IPA
Dehydrate bake: 2 min @ 130 °C hotplate

Resist coating: HMDS, SC1827 @ 4 krpm, 30 sec
Pre-bake: 1 min @ 105 °C hotplate
Exposure: 12~12.5 sec (vacuum/or hard contact)
Resist development: AZ 351 : DI H_2O= 1 : 5, 45 sec;
DI H_2O rinse 3 min
De-scum (plasma ashier): 1 min, 80 W, 250mTorr, 17% O_2

5.2. Etching:

ICP dry etching (LAM): Cl_2 : Ar=2.6 : 11.6 sccm, 2 mTorr,
TCP power=300 W, Bias power=36 W
Wet etching: H_3PO_4 : H_2O_2 : DI H_2O= 1 : 1 : 3, etch rate~1000 Å/sec

---

II. Ridge Wave-Guide Edge-Emitting Laser and Modulator Fabrication

---

6. P-Ohmic Metallization:

6.1. Oxide removal: BHF 30-60 sec.

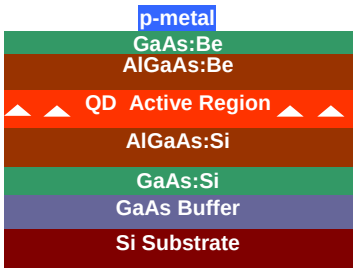

6.2. Solvent clean:

Xylenes > 15 min @ 105 °C hotplate
Acetone 10 min, clean with Q-tip
IPA 10 min

6.3. Lithography

Dehydrate bake: 2 min, 130 °C hotplate
Resist coating: HMDS, AZ5214 @ 4.0 krpm, 30 sec
Pre-bake: 1 min @ 105 °C hotplate
Edge removal:
Exposure: 60 sec,
Resist development: MF319, 60 sec; DI H_2O rinse 3 min
Exposure: 4 sec, vacuum contact.
Post-bake: 1 min @ 110~115 °C
Image reversal exposure: 90 sec
Resist development: MF319, 25~35 sec; DI H_2O 3 min

6.4. De-scum (plasma ashier): 1 min, 80 W, 250mTorr, 17% O_2

6.5. Oxide removal: BHF 20~30 sec; DI H_2O rinse 3 min

6.6. Deposition (E-beam evaporator): Pd/Zn/Pd/Au = 100/200/200/3000 Å.

6.7. Lift-off:

PRS1000 (hot solution ready): 105 °C hotplate
Acetone: 10 min, warm
IPA: 10 min

6.8. Dektak: measure metal thickness

---

7. Ridge Mesa Formation: Self Aligned Etching Using P-Metal.

7.1. RIE:

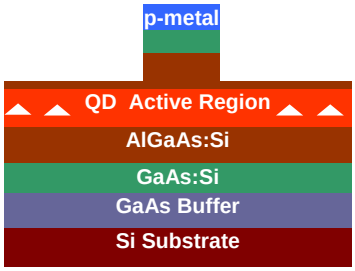

BCl_3/Ar = 11/21 sccm,

15 mT, 50W, 75 min (rate ~ 100 Å/min)

7.2. Dektak: Measure etch-depth

7.3. Wet-etching:

H_3PO_4 : H_2O_2 : DI water= 1 : 1 : 10

7.4. Dektak: Stop etching ~ 0.1 µm above the quantum dot active region.

* Note: This etch step is very critical and can significantly affect the performance; typically, etching stop at leaving 0.1 µm up-cladding layer. The dry etching and wet etching is alternate by repeating 2-3 circles.

---

8. N-Contact Mesa Formation and N-Ohmic Metallization:

8.1. Lithography:

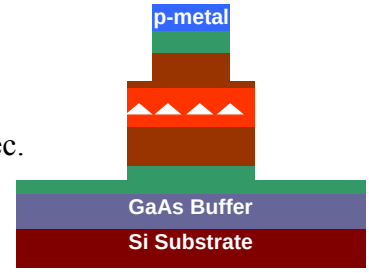

Solvent clean: warm Acetone, IPA.
Dehydrate bake: 2 min @ 130 °C hotplate
Resist coating: HMDS, SC1827 @ 4 krpm, 30 sec.
Pre-bake: 1 min @ 105 °C hotplate
Exposure: 12~12.5 sec (hard contact).
Resist development: AZ 351 : DI = 1 : 5, 45 sec;
DI H_2O rinse 3 min
De-scum (plasma ashier): 1 min, 80 W, 250mTorr, 17% O_2

8.2. Dektak:

8.3. Etching:

RIE: BCl_3 : Ar = 11 : 21 sccm, 10-15mT, 50 W, 60 min (rate ~ 100 Å/min)
Wet-etching: H_3PO_4 : H_2O_2 : DI H_2O=1 : 1 : 3 (rate ~ 1000 Å/sec)
Dektak
* Note: Too much dry etch will rough the surface;
Wet etch will create undercut for easy lift-off.

8.4. Oxide removal: BHF 25 sec.

8.5. Deposition: Ni/Ge/Au/Ti/Au = 250/325/650/200/3000 Å

8.6. Lift-off:

PRS1000 (hot solution ready): 105 °C hotplate
Acetone: 10 min, warm
IPA: 10 min

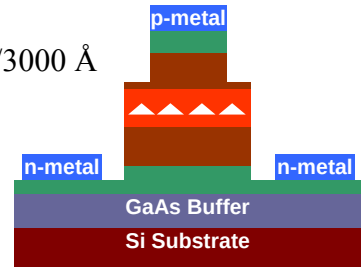

---

9. Contact Annealing:

250/410/250 °C: 45/90/45 sec.
* Note: Or two-step annealing (to avoid N-metal pill off):
P-metal annealing (after p-metal formation): 250/410/250 °C, 45/90/45 sec; N-metal annealing (after n-metal formation): 250/390/250 °C, 45/90/45 sec

---

10. Passivation:

10.1. Solvent clean: warm Acetone, IPA
10.2. PECVD: SiO_x deposition, 1 μm, 200 °C

* Note: Step 5 (annealing) and step 6 (passivation) can switch in sequence.

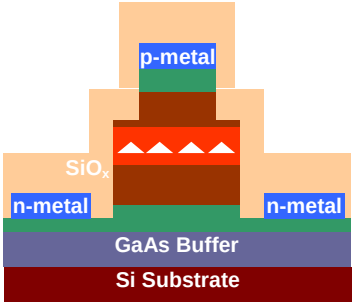

---

11. Via Hole (Open Hole for Interconnect):

11.1. Lithography

Solvent clean: warm Acetone, IPA.
Dehydrate bake: 2 min @ 130 °C hotplate
Resist coating: HMDS, SC1827 @ 4 krpm, 30 sec.
Pre-bake: 1 min @ 105 °C hotplate
Edge removal:
Exposure: 60 sec,
Resist development:
AZ 351 : DI H_2O = 1 : 5, 60 sec; DI water 3 min

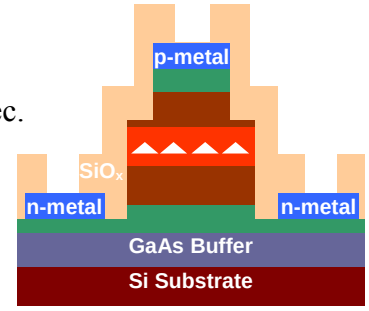

Exposure: 12~12.5 sec (vacuum/or hard contact).
Resist development: AZ 351 : DI = 1:5, 45 sec; DI H_2O rinse 3 min
De-scum (plasma ashier): 1 min, 80 W, 250mT, 17% O_2

11.2. Reactive-Ion-Etching (RIE):
Semigroup RIE: CF_4 : CHF_3 = 25 : 25 sccm, 40 mTorr, 180W,
etch rate ~300 Å/min.
Etch 15 minutes to obtain etch rate (or using a Dummy sample as a monitor)
Over etch 30 %

11.3. Strip resist:
Hot PRS1000 > 20 min, warm Acetone, IPA
Descum: 3 min @ 150W;
Or using RIE O_2 plasma etching: 100mT, 150W, 3~5 min

---

12. Interconnect Metallization:

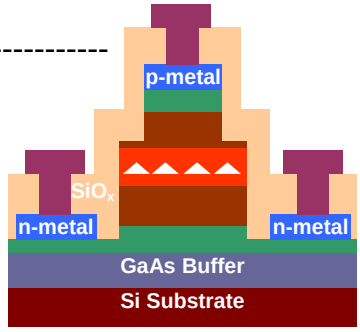

12.1. Lithography:

Solvent clean: warm Acetone, IPA.
Dehydrate bake: 2 min @ 130 °C hotplate
Resist coating: HMDS, SC1827 @ 3.5 krpm, 30 sec.
Pre-bake: 1 min @ 105 °C hotplate
Chlorobenzene soak: 5 min.
Exposure: 13~13.5 sec (vacuum/or hard contact).
Resist development: AZ 351 : DI = 1:5, 50 sec; DI H_2O rinse 3 min
De-scum (plasma ashier): 1 min, 80 W, 250mT, 17% O_2

12.2. Metal Deposition: Ti/Al/Ti/Au = 500/8000/500/3000 Å.
12.3. Liftoff: Hot PRS 1000 overnight, warm Acetone, IPA.

---

13. Scribing:

Make 2000 μm long, 400~1200 μm wide, 100 μm deep scribe.

---

14. Lapping

14.1. Mounting the sample on a glass plate with Paraffin wax (140~150 °C)

14.2. Lap down sample to ~ 120 μm and 80 μm for quantum dot lasers on GaAs and Si, respectively.

14.3. Solvent clean:

Xylenes > 15 min @ 105 °C hotplate
Acetone 10 min, clean with Q-tip
IPA 10 min

---

15. Cleaving

15.1. Mounting the sample on a metal strip with black wax (150~160 °C)

15.2. Bending the strip on the sharp edge

15.3. Solvent clean:

Xylenes > 30 min @ 105 °C hotplate
Acetone 10 min, clean with Q-tip
IPA 10 min

---

16. HR/AR coating:

16.1. Laser-bar Mounting:

Resist coating: HMDS, SC1827 @ 1 krpm, 10 sec
Rapidly mount laser bars with facet up
Bake 105 °C, 30~60 sec

16.2. Dielectric layer coating:

HR coating: MgF_2 : ZnSe=λ/4 : λ/4, 3-5 pairs; n_{MgF}~1.37, n_{ZnSe}~2.47
AR coating: Al_2O_3= λ/4, $n_{Al_2O_3}$~1.6

16.3. Resist removal:

Acetone 10 min, warm
IPA 10 min

* Note: The bar surface was also coated with a very thin dielectric layer, which form a residue line close to mounting facet.

---

17. Focused-Ion-beam (FIB) Etching:

17.1. Mounting: silver paint

17.2. Focusing: get clear SEM and FIB image

17.3. Etching:

Initially etching with large power (20 KV, ~2 nA);
Polishing the etched facets with small power (20 KV, ~100 pA)

17.4. Solvent clean:

Acetone 10 min, warm
IPA 10 min

BIBLIOGRAPHY

BIBLIOGRAPHY

[1] G. Moore, "Progress in Digital Integrated Electronics," *1975 IEEE, IEDM Tech Digest*, pp.11-13; and online link "Intel press kit released for Moore's Law's 40th anniversary by http://www.intel.com/pressroom/kits/events/moores_law_40th/index.htm.

[2] S. Luryi, J. Xu, and A. Zaslavsky (Eds.), *Future trends in Microelectronics: The Road Ahead*, Wiley, New York, 1999.

[3] M. A. Nielsen and I. L. Chuang, *Quantum Computation and Quantum Information*. Cambridge: Cambridge University Press, 2000.

[4] R. A., Jr. Freitas, *Nanomedicine*, Volume I: Basic Capabilities, pp.349-351, Austin, Texas: Landes Bioscience, 1999.

[5] J. W. Goodman, F. J. Leonberger, S. Y. Kung, and R. A. Athale, "Optical interconnections for VLSI systems," *Proc. IEEE*, vol.72, no.7, pp.850–866, 1984.

[6] D. A. B. Miller, **"**Rationale and challenges for optical interconnects to electronic chips**,"** *Proc. IEEE*, vol.88, no.6, pp.728-749, 2000.

[7] R. A. Soref and J. P. Lorenzo, "All-silicon active and passive guided-wave components for λ=1.3 and 1.6 μm," *IEEE J. Quantum Electron.*, vol.22, no.6, pp.873-879, 1986.

[8] R. Soref, "The past, present, and future of silicon photonics," *IEEE J. Sel. Top. Quantum Electron.* vol.12, no.6, pp. 1678-1687, 2006.

[9] B. Jalali and S. Fathpour, "Silicon photonics," *J. Lightwave Technol.*, vol.24, no.12, pp.4600-4615, 2006.

[10] M. Lipson, "Guiding, modulating, and emitting light on silicon — challenges and opportunities," *J. Lightwave Technol.*, vol.23, no.12, pp. 4222-4238, 2005.

[11] W. H. Chang, A. T. Chou, W. Y. Chen, H. S. Chang, T. M. Hsu, Z. Pei, P. S. Chen, S. W. Lee, L. S. Lai, S. C. Lu, and M. J. Tsai, "Room-temperature electroluminescence at 1.3 and 1.5 μm from Ge/Si self-assembled quantum dots," *Appl. Phys. Lett.*, vol.83, no.14, pp. 2958-2960, 2003.

[12] R. J. Walters, G. I. Bourianoff, and H. A. Atwater, "Field-effect electroluminescence in silicon nanocrystals," *Nature Mater.*, vol.4, no.2, pp.143-146, 2005.

[13] S. G. Cloutier, P. A. Kossyrev, and J. Xu, "Optical gain and stimulated emission in periodic nanopatterned crystalline silicon," *Nature Mater*., vol.4, no.12, pp.887-891, 2005.

[14] O. Boyraz and B. Jalali, "Demonstration of a silicon Raman laser," *Opt. Express*, vol.12, no.21, pp5269-5273, 2004.

[15] H. S. Rong, R. Jones, A. S. Liu, O. Cohen, D. Hak, A. Fang, and M. Paniccia, "A continuous-wave Raman silicon laser," *Nature,* vol.433, no.7027, pp.725-728, 2005.

[16] A. Georgakilas, G. Deligeorgis, E. Aperathitis, D. Cengher, Z. Hatzopoulos, M. Alexe, V. Dragoi, U. Gosele, E. D. Kyriakis-Bitzaros, K. Minoglou, and G. Halkias, "Wafer-scale integration of GaAs optoelectronic devices with standard Si integrated circuits using a low-temperature bonding procedure," *Appl. Phys. Lett.* vol.81, no.27, pp.5099-5101, 2002.

[17] A. W. Fang, H Park, O Cohen, R Jones, M. J. Paniccia, and J. E. Bowers, "Electrically pumped hybrid AlGaInAs-silicon evanescent laser," *Opt. Express*, vol.14, no.20, pp.9203-9210, 2006.

[18] R. Fischer, W. Kopp, H. Morkoc, M. Pion, A. Specht, G. Burkhart, H. Appelman, D. McGougan, and R. Rice, "Low threshold laser operation at room temperature in GaAs/(Al, Ga)As structures grown directly on (100) Si," *Appl. Phys. Lett.*, vol.48, no.20, pp.1360-1361, 1986.

[19] R. D. Dupuis, J. P. van der Ziel, R. A. Logan, J. M. Brown and C. J. Prinzone, "Low-threshold high-efficiency AlGaAs-GaAs double-heterostructure injection lasers grown on Si substrates by metalorganic chemical vapor deposition," *Appl. Phys. Lett.*, vol.50, no.7, pp.407-409, 1987.

[20] M. E. Groenert, C. W. Leitz, A. J. Pitera, V. Yang, H. Lee, R. J. Ram, and E. A. Fitzgerald, "Monolithic integration of room-temperature cw GaAs/AlGaAs lasers on Si substrates via relaxed graded GeSi buffer layers," *J. Appl. Phys*., vol.93, no.1, pp.362-367, 2003.

[21] J. Yang, P. Bhattacharya, and Z. Mi, "High-performance $In_{0.5}Ga_{0.5}As$/GaAs quantum-dot laser on silicon with multiple-layer quantum-dot dislocation filters," *IEEE Trans. Electron Dev.*, vol.54, no.11, pp. 2849-2855, 2007.

[22] R. A. Soref and B. R. Bennett, "Electrooptical effects in silicon," *IEEE J. Quantum Electron.*, vol.23, no.1, pp.123-129, 1987.

[23] D. A. B. Miller, D. S. Chemla, T. C. Damen, A. C. Gossard, W. Wiegmann, T. H. Wood, and C. A. Burrus, "Band-edge electroabsorption in quantum well structures: the quantum-confined Stark effect," *Phys. Rev. Lett.*, vol.53, no.22, pp.2173-2176, 1984.

[24] J. P. Lorenzo and R.A. Soref, "1.3 μm electro-optic silicon switch," *Appl. Phys. Lett.*, vol.5, no.1, pp. 6-8, 1987.

[25] C. K. Tang and G. T. Reed, "Highly efficient optical phase modulator in SOI waveguides," *Electron. Lett.*, vol.31, no.6, pp. 451-452, 1995.

[26] A. S. Liu, R. Jones, L. Liao, D. Samara-Rubio, D. Rubin, O. Cohen, R. Nicolaescu, and M. Paniccia, "A high-speed silicon optical modulator based on a metal-oxise-semiconductor capacitor," *Nature*, vol.427, no.6975, pp.615-618, 2004.

[27] L. Liao, D. Samara-Rubio, M. Morse, A. S. Liu, D. Hodge, D. Rubin, U. D. Keil, and T. Franck, "High speed silicon Mach-Zehnder modulator," *Opt. Express*, vol.13, no.8, pp.3129-3135, 2005

[28] Q. F. Xu, B. Schmidt, S. Pradhan, and M. Lipson, "Micrometer-scale silicon electro-optic modulator," *Nature*, vol.435, no.7040, pp.325-327, 2005.

[29] O. Qasaimeh, P. Bhattacharya, and E. T. Croke, "SiGe-Si quantum-well electroabsorption modulators," *IEEE Photon. Technol. Lett.*, vol.10, no.6, pp.807-809, 1998.

[30] Y. H. Kuo, Y. K. Lee, Y. S. Ge, S. Ren, J. E. Roth, T. I. Kamins, D. A. B. Miller, and J. S. Harris, "Strong quantum-confined Start effect in germanium quantum-well structures on silicon," *Nature*, vol.437, no.7063, pp.1334-1336, 2005.

[31] K. K. Lee, D. R. Lim, and L. C. Kimerling, J. Shin, and F. Cerrina, "Fabrication of ultralow-loss Si/SiO_2 waveguides by roughness reduction," *Opt. Lett.*, vol.26, no.23 pp.1888-1890, 2001.

[32] Y. A. Vlasov and S. J. McNab, "Losses in single-mode silicon-on-insulator strip waveguides and bends," *Opt. Express*, vol.12, no.8, pp.1622-1631, 2004.

[33] C. Manolatou, S. G. Johnson, S. H. Fan, P. R. Villeneuve, H. A. Haus, and J. D. Joannopoulos, "High-density integrated optics," *J. Lightwave Technol.*, vol.17, no.19, pp. 1682-1692, 1999.

[34] M. Loncar, D. Nedeljkovic, T. Doll, J. Vuckovic, A. Scherer, and T. P. Pearsall, "Waveguiding in planar photonic crystals," *Appl. Phys. Lett.*, vol.77, no.13, pp.1937-1939, 2000.

[35] G. Cocorullo, F. G. Della Corte, R. De Rosa, I. Rendina, A. Rubino, and E. Terzini, "Amorphous silicon-based guided-wave passive and active devices for silicon integrated optoelectronics," *IEEE J. Sel. Top. Quantum Electron.*, vol.4, no.6, pp.997-1002, 1998.

[36] A. Harke, M. Krause, and J. Mueller, "Low-loss singlemode amorphous silicon waveguides," *Electron. Lett.*, vol.41, no.25, pp. 1377-1379, 2005.

[37] N. M. Park, T. S. Kim, and S. J. Park, "Band gap engineering of amorphous silicon quantum dots for light-emitting diodes," *Appl. Phys. Lett.*, vol.78, no.17, pp. 2575-2577, 2001.

[38] M. W. Pruessner, T. H. Stievater, M. S. Ferraro, and W. S. Rabinovich, "Thermo-optic tuning and switching in SOI waveguide Fabry-Perot microcavities," *Opt. Express*, vol.15, no.12, pp.7557-7563, 2007; and references therein.

[39] S. F. Fang, K. Adomi, S. Iyer, H. Morkoc, H. Zabel, C. Choi, and N. Otsuka, "Gallium arsenide and other compound semicondtors on silicon," *J. Appl. Phys.*, vol.68, no.7, pp.R31-R58, 1990.

[40] S. Sakai, T. Soga, M. Takeyasu and M. Umeno, "Room-temperature laser operation of AlGaAs GaAs double heterostructures fabricated on Si substrates by metalorganic chemical vapor deposition," *Appl. Phys. Lett.*, vol.48, no.6, pp.413-414, 1986.

[41] R. Fischer, D. Neuman, H. Zabel, H. Morkoc, C. Choi and N. Otsuka, "Dislocation reduction in epitaxial GaAs on Si (100)," *Appl. Phys. Lett*., vol.48, no.18, pp.1223-1225, 1986.

[42] T. Egawa, Y. Hasegawa, T. Jimbo and M. Umeno, "Effects of dislocation and stress on characteristics of GaAs-based laser grown on Si by metalorganic chemical vapor deposition," *Jpn. J. Appl. Phys. Part 1*, vol.31, no.3, pp.791-797, 1992.

[43] E. A. Fitzgerald, G. P. Watson, R. E. Proano, D. G. Ast, P. D. Kirchner, G. D. Pettit and J. M. Woodall, "Nucleation mechanisms and the elimination of misfit dislocations at mismatched interfaces by reduction in growth area," *J. Appl. Phys.*, vol.65, no.6, pp.2220-2237, 1989.

[44] S. Nakamura, M. Senoh, S. Nagahama, N. Iwasa, T. Yamada, T. Matsushita, H. Kiyoku, Y. Sugimoto, T. Kozaki, H. Umemoto, M. Sano, and K. Chocho, "InGaN/GaN/AlGaN-based laser diodes with modulation-doped strained-layer superlattices grown on an epitaxially laterally overgrown GaN substrate," *Appl. Phys. Lett.*, vol.72, no. 2, pp.211-213, 1998.

[45] G. Balakrishnan, S. H. Huang, A. Khoshakhlagh, P. Hill, A. Amtout, S. Krishna , G. P. Donati, L. R. Dawson, D. L. Huffaker, "Room-temperature optically-pumped InGaSb quantum well lasers monolithically grown on Si(100) substrate," *Electron. Lett.*, vol.41, no.9, pp.531-532, 2005.

[46] K. Eisenbeiser, J. M. Finder, Z. Yu, J. Ramdani, J. A. Curless, J. A. Hallmark, R. Droopad, W. J. Ooms, L. Salem, S. Bradshaw, and C. D. Overgaard, "Field effect transistors with $SrTiO_3$ gate dielectric on Si," *Appl. Phys. Lett.*, vol.76, no.10, pp.1324-1326, 2000.

[47] L. Sugiura, "Comparison of degradation caused by dislocation motion in compound semiconductor light-emitting devices," *Appl. Phys. Lett.*, vol.70, no.10, pp.1317-1319, 1997; and references therein.

[48] K. Maeda, M. Sato, A. Kubo, and S. Takeuchi, "Quantitative measurements of recombination enhanced dislocation glide in gallium arsenide," *J. Appl. Phys.*, vol.54, no. 1, pp.161-168, 1983.

[49] D. Bimberg, "Quantum dots: paradigm changes in semiconductor physics," *Semiconductors*, vol.33, no.9, pp.951-955, 1999.

[50] J. P. Van der Ziel, R. Dingle, R. C. Miller, W. Wiegmann, and W. A. Nordland Jr., "Laser oscillations from quantum states in very thin GaAs-$Al_{0.2}Ga_{0.8}As$ multilayer structures," *Appl. Phys. Lett.*, vol.26, no.8, pp. 463-465, 1975.

[51] R. D. Dupuis, P. D. Dapkus, N. Holonyak Jr., E. A. Rezek, and R. Chin, "Room-tempertaure laser operation of quantum-well $Ga_{1-x}Al_xAs$ laser diodes grown by metalorganic chemical vapor deposition," *Appl. Phys. Lett.*, vol.32, no.5, pp.295-297, 1978.

[52] A. I. Ekimov and A. A. Onushchenko, "Quantum size effect in 3-demennsional microscopic semisconductor crystas," *JETP Lett.*, vol.34, no.6, pp.345-349, 1981.

[53] Y. Arakawa and H. Sakaki, "Multidimensional quantum well laser and temperature dependence of its threshold current," *Appl. Phys. Lett.*, vol.40, no.11, pp.939-941, 1982.

[54] M. Asada, Y. Miyamoto, and Y. Suematsu, "Gain and threshold of three-dimmentioanl quantum box-lasers," *IEEE J. Quantum Electron.*, vol.22, no.9, pp.1915-1921, 1986.

[55] J. Urayama, T. Norris, J. Singh, and P. Bhattacharya, "Observation of phonon bottleneck in quantum dot electronic relaxation," *Phys. Rev. Lett.*, vol.86, no.21, pp.4930-4933, 2001.

[56] J. Urayama, T. B. Norris, H. Jiang, J. Singh, and P. Bhattacharya, "Temperature-dependent carrier dynamics in self-assembled InGaAs quantum dots," *Appl. Phys. Lett.*, vol.80, no.12, pp.2162-2164, 2002.

[57] I. Vurgaftman, Y. L. Lam, and J. Singh, "Carrier thermalization in sub three-dimmentional electronics systems: Fundamental limits on modulation bandwidth in semiconductor lasers," *Phys. Rev. B*, vol.50, no.19, pp.14309-14326, 1994.

[58] P. Bhattacharya, S. Ghosh, S. Pradhan, J. Singh, Z. K. Wu, J. Urayama, K. Kim, and T. B. Norris, "Carrier dynamics and high-speed modulation properties of tunnel injection InGaAs–GaAs quantum-dot lasers," *IEEE J. Quantum Electron.*, vol.39, no.8, pp. 952-962, 2003.

[59] P. R. Berger, K. Chang, P. Bhattacharya, J. Singh and K. K. Bajai, "Role of strain and growth-conditions on the growth front profile of $In_xGa_{1-x}As$ on GaAs during the pseudomorphic growth regime," *Appl. Phys. Lett.*, vol.53, no.8, pp.684-686,1988.

[60] D. Leonard, M. Krishnamurthy, C. M. Reaves, S. P. Denbaars, and P. M. Petroff, "Direct formation of quantum-sized dots from uniform coherent islands of InGaAs on GaAs surfaces," *Appl. Phys. Lett*., vol.63, no.23, pp.3203-3205, 1993.

[61] J. Pamulapati, P. K. Bhattacharya, J. Singh, P. R. Berger, C. W. Snyder, B. G. Orr, R. L. Tober, "Realization of in-situ sub two-dimensional quantum structures by strained

layer growth phenomena in the $In_xGa_{1-x}As/GaAs$ system," *J. Electron. Mater*., vol.25, no.3, pp.479-483, 1996.

[62] F. C. Frank, and J. H. van der Merwe, "One-dimensional dislocations: 1. static theory," *Proceedings of Royal Society of London A*, vol.198, no.1053, pp.205-216, 1949.

[63] I. N. Stranski, and L. Krasranow, "Sitzungsberichte d. Akad. D. Wissenschaften in Wien," *Abt. IIb.*, Band, vol.146, pp.146, 1937.

[64] M. Volmer, and A. Weber, *Z. Phys. Chem*., "Germ-formationin oversaturated figures," vol.119, no.3-4. pp. 277-301, 1926.

[65] H. Hirayama, K. Matsunaga, M. Asada, and Y. Suematsu, "Lasing action of $Ga_{0.67}In_{0.33}As/GaInAsP/inP$ tensile-strained quantum box lasers," *Electron. Lett.*, vol.30, no.2, pp.142-143, 1994.

[66] N. Kirstaedter, N. N. Ledentsov, M. Grundmann, D. Bimberg, V. M. Ustinov, S. S. Ruvimov, M. V. Maximov, P. S. Kopev, Z. I. Alferov, U. Richter, P. Wernep, U. Gosele, and J. Heydenreich, "Low threshold, large T_0 injection laser emission from (InGa)As quantum dots," *Electron. Lett.*, vol.30, no.17, pp. 1416-1417, 1994.

[67] K. Kamath, P. Bhattacharya, T. Sonowski, T. Norris, J. Phillips, "Room-temperature operation of $In_{0.4}Ga_{0.6}As/GaAs$ self-organized quantum dot lasers," *Electron. Lett.*, vol.32, no.15, pp.1374-1375, 1996.

[68] R. Mirin, A. Gossard, and J. Bowers, "Room temperature lasing from InGaAs quantum dots," *Electron. Lett.*, vol. 32, no.18, pp. 1732–1734, 1996.

[69] P. G. Eliseev, H. Li, G. T. Liu, A. Stintz, T. C. Newell, L. F. Lester, and K. J. Malloy, "Ground-state emsiison and gain in ultralow-threshold InAs-InGaAs quantum-dot lasers," *IEEE J. Sel. Top. Quantum Electron.*, vol.7, no.2, pp.135-142, 2001.

[70] D. Klotzkin, K. Kamath, K. Vineberg, P. Bhattacharya, R. Murty, and J. Laskar, "Enhanced modulation bandwidth (20GHz) of $In_{0.4}Ga_{0.6}As/GaAs$ self-organized quantum dot lasers at cryogenic temperatures: role of carrier relaxation and differential gain," *IEEE photon. Technol. Lett.*, vol.10, no.7, pp.932-934, 1998.

[71] N. Kirstaedter, O. G. Schmidt, N. N. Ledentsov, D. Bimberg, V. M. Ustinov, A.Y. Egorov, A. E. Zhukov, M. V. Maximov, P. S. Kopev, and Z. I. Alferov, "Gain and differential gain of single layer InGaAs/GaAs quantum dot injection lasers," *Appl. Phys. Lett.*, vol.69, no.9, pp.1226-1228, 1996.

[72] H. Saito, K. Nishi, and S. Sugou,"Low chirp operation in 1.6 μm quantum dot laser under 2.5Ghz direct modulation," *Electron. Lett.*, vol.37, no.21, pp.1293-1295, 2001.

[73] T. C. Newell, D. J. Bossert, A. Stintz, B. Fuchs, K. J. Malloy, and L. F. Lester, "Gain and linewidth enhancement factor in InAs quantum dot diodes," *IEEE Photon. Technol. Lett.*, vol.11, no.12, pp.1527-1529, 1999.

[74] H. C. Sun, L. Davis, S. Sethi, J. Singh, and P. Bhattacharya, "Properties of a tunneling injection quantum-well laser — recipe for a cold device with a large modulation bandwidth," *IEEE Photon. Techn. Lett.*, vol.5, no.8, pp. 870-872, 1993.

[75] L. V. Asryan and S.Luryi, "Tunnel-injection quantum dots laser: ultra-high temperature stability," *IEEE J. Quantum Electron.*, vol.37, no.7, pp. 905-910, 2001.

[76] P. Bhattacharya and S. Ghosh, "Tunnel injection $In_{0.4}Ga_{0.6}As$/GaAs quantum dot lasers with 15 GHz modulation bandwidth at room-temperature," *Appl. Phys. Lett.*, vol. 80, no.19, pp.3482-3484, 2002.

[77] Y. Miyamoto, Y. Miyake, M. Asada, and Y. Suematsu, "Threshold current density of GaInAsP/InP quantum box lasers," *IEEE J. Quantum Electron.*, vol. 25, no.9, pp.2001-2006, 1989.

[78] O. B. Shchekin and D. G. Deppe, "Low-threshold high-T_0 1.3 μm InAs quantum dot lasers due to p-type modulation doping of the active region," *IEEE Photon. Technol. Lett.*, vol.14, no.9, pp.1231-1233, 2002.

[79] D. G. Deppe, H. Huang, and O. B. Shchekin, "Modulation characteristics of quantum-dot lasers: The influence of p-type doping and the electronic density of states on obtaining high speed," *IEEE J. Quantum Electron.*, vol.38, no.12, pp.1587-1593, 2002.

[80] S. Fathpour, Z. Mi, P. Bhattacharya, A. R. Kovsh, S. S. Mikhrin, I. L. Krestnikov, A. V. Kozhukhov, and N. N. Ledentsov, "The role of Auger recombination in the temperature-dependent output characteristics ($T_0 = \infty$) of p-doped 1.3 μm quantum dot lasers," *Appl. Phys. Lett.*, vol.85, no.22, pp.5164–5166, 2004.

[81] M. Gioannini, "Investigation of p-type doping effect on the gain characteristics of quantum dash semiconductor lasers," *Proc. SPIE*, vol. 5452, pp. 526–533, 2004.

[82] N. N. Ledentsov, M. V. Maximov, D. Bimberg, T. Maka, C. M. S. Torres, I V. Kochnev, I. L. Krestnikov, V. M. Lantratov, N. A. Cherkashin, Y. M. Musikhin, Z. I Alferov, "1.3 μm luminescence and gain from defect-free InGaAs-GaAs quantum dots grown by metal-organic chemical vapour deposition," *Semicond. Sci. Technol*., vol.15, no.6, pp.604-607, 2000.

[83] J. W. Matthews and A. E. Blakeslee, "Defects in epitaxial multilayers: I. misfit dislocations," *J. Crystal. Growth*, vol.27, pp.118-125, 1974.

[84] N. A. EL-Masry, J. C. Tarn and N. H. Karam, "Interactions of Dislocations in GaAs grown on Si substrates with InGaAs-GaAsP Strained layered superlattices," *J. Appl. Phys.,* vol.64, no.7, pp.3672-3677, 1988.

[85] M. O. Peach and J. S. Koehler, "The forces exerted on dislocations and the stress fields produced by them" *Phys. Rev.*, vol.80, no.3, pp.436-439, 1950.

[86] D. Huang, M. A. Reshchikov, F. Yun, T. King, A. A. Baski and H. Morkoc, "Defect reduction with quantum dots in GaN grown on sapphire substrates by molecular beam epitaxy," *Appl. Phys. Lett.*, vol.80, no.2, pp.216-218, 2002.

[87] Z. Mi, P. Bhattacharya, J. Yang, and K. P. Pipe, "Room-temperature self-organised $In_{0.5}Ga_{0.5}As$ quantum dot laser on silicon," *Electron. Lett.*, vol.41, no.13, pp.742-744, 2005.

[88] K. Tillmann and A. Forster, "Critical dimensions for the formation of interfacial misfit dislocations of $In_{0.6}Ga_{0.4}As$ islands on GaAs(001)," *Thin Solid Film,* vol.368, no.1, pp.93-104, 2000.

[89] I. A. Ovid'ko, "Relaxation mechanisms in strained nanoislands," *Phys. Rev. Lett*., vol. 88, no.4, art. no.046103, 2002.

[90] H. Jiang and J. Singh, "Strain distribution and electronic spectra of InAs/GaAs self-assembled dots: An eight-band study," *Phys. Rev. B*, vol.56, no.8, pp.4696-4701, 1997.

[91] J. Y. Tsao and B. W. Dodson, "Excess stress and the stability of strained heterostructures," *Appl. Phys. Lett*., vol.53, no.10, pp.848-850, 1988.

[92] H. Y. Liu, S. L. Liew, T. Badcock, D. J. Mowbray, M. S. Skolnick, S. K. Ray, T. L. Choi, K. M. Groom, B. Stevens, F. Hasbullah, C. Y. Jin, M. Hopkinson, and R. A. Hogg, "p-doped 1.3 μm InAs/GaAs quantum-dot laser with a low threshold current density and high differential efficiency," *Appl. Phys. Letts.*, vol.89, no.7, art. no.073113, 2006.

[93] A. Lenz, H. Eisele, R. Timm, S. K. Becker, R. L. Sellin, U. W. Pohl, D. Bimberg, and M. Dahne, "Nanovoids in InGaAs/GaAs quantum dots observed by cross-sectional scanning tunneling microscopy," *Appl. Phys. Letts.*, vol. 85, no.17, pp.3848-3850, 2004.

[94] T. H. Wood, "Multiple quantum well (MQW) wave-guide modulators," *J. Lightwave Technol.* vol.6, no.6, pp.743-757, 1988.

[95] O. Qasaimeh, K. Kamath, P. Bhattacharya, J. Phillips, "Linear and quadratic electro-optic coefficients of self-organized $In_{0.4}Ga_{0.6}As$/GaAs quantum dots," *Appl. Phys. Lett.*, vol.72, no.11, pp.1275-1277, 1998.

[96] L. A. Coldren, K. Furuya, B. I. Miller and J. A. Rentschler, "Etched mirror and groove-coupled GaInAsP/InP laser devices for integrated optics," *IEEE J. Quantum Electron.* vol.18, no.10, pp.1679-1688, 1982.

[97] G. P. Agrawal and N. K. Dutta, *Semiconductor Lasers*, 2nd ed., New York: Van Nostrand-Reinhold, 1993, Ch.8.

[98] W. D. Herzog, M. S. Unlu, B. B. Goldberg, G. H. Rhodes and C. Harder, "Beam divergence and waist measurements of laser diodes by near-field scanning optical microscopy," *Appl. Phys. Lett.*, vol.70, no.6, pp.688-690, 1997.

[99] A. E. Siegman, "New developments in laser resonators," in Optical Resonators, D. A. Holmes, ed., *Proc. SPIE*, vol.1224, pp.2–14, 1990.

[100] Gouy, *C. R. Acad. Sci. Paris*, vol.110, pp.1251, 1890.

[101] Gouy, *Ann. Chim. Phys. Ser.* vol. 6, XXIV, pp.145, 1891.

[102] A. E. Siegman, *Laser*, University of Science Books, 1986.

[103] R. W. Boyd, "Intutive explanation of the phase anomaly of focused light-beams," *J. Opt. Soc. Am.*, vol. 70, no.7, pp.877-880, 1980.

[104] S. Feng and H.G. Winful, "Physical origin of the Gouy phase shift,"*Opt. Lett.*, vol. 26, no. 8, pp. 485-487, 2001.

[105] P. Hariharan and P. A. Robinson, "The Gouy phase shift as a geometrical quantum effect," *J. Mod. Optics*, vol. 43, no.2, pp. 219-221, 1996.

[106] J. Yang and H. G. Winful, "Generalized eikonal treatment of the Gouy phase shift," *Opt. Lett.*, vol.31, pp.104-106, 2006.

[107] P.A. Belanger, "Beam propagation and the ABCD ray matrices," *Opt. Lett.*, vol.16, no.4, pp.196-198, 1991.

[108] J. Yang and D. Fan, "Intensity-moments characterization of general pulsed paraxial beams with the Wigner distribution function," *J. Opt. Soc. Am. A*, vol.16, no.10, pp. 2488-2493, 1999.

[109] Y. Yuan, T. R. Jambunathan, J. Singh and P. Bhattacharya, "Finite-Difference Time-domain analysis and experimental examination of the performance of a coupled-cavity MQW laser/active waveguide at 1.54μm," *IEEE J. Quantum Electron.*, vol.33, no.3, pp.408-415, 1997.

[110] M. P. Mack, G. D. Via, A. C. Abare, M. Hansen, P. Kozodoy, S. Keller, J. S. Speck, U. K. Mishra, L. A. Coldren, and S. P. DenBaars, "Improvement of GaN-based laser diode facets by FIB polishing," *Electron. Lett.*, vol.34, no.13, pp.1315- 1316, 1998.

[111] L. Bach, S Rennon, J. P. Reithmaier, A. Forchel, J. L. Gentner and L. Goldstein, "Laterally coupled DBR laser emitting at 1.55 μm fabricated by focused ion beam lithography," *IEEE Photon. Tech. Lett.*, vol.14, no.8, pp.1037-1039, 2002.

[112] P. Bhattacharya, *Semiconductor Optoelectronic Devices*, 2nd ed., Prentice Hall, 1996.

[113] C. Ribbat, R. L. Sellin, I. Kaiander, F. Hopfer, N. N. Ledentsov, D. Bimberg, A. R. Kovsh, V. M. Ustinov, A. E. Zhukov and M. V. Maximov, "Complete suppression of filamentation and superior beam quality in quantum-dot lasers," *Appl. Phys. Lett.*, vol.82, no.6, pp.952-954, 2003.

[114] J. Yang, Z. Mi, and P. Bhattacharya, "Grooved-coupled InGaAs/GaAs quantum dot laser/waveguide on silicon," *J. Lightwave Technol.*, vol.25, no.7, pp.1826-1831, 2007.

[115] Z. Mi, P. Bhattacharya, and J. Yang, "Growth and characteristics of ultralow threshold 1.45 μm metamorphic InAs tunnel injection quantum dot lasers on GaAs," *Appl. Phys. Lett.*, vol.89, no.15, art. no.153109, 2006.

[116] Z. Wu, Z. Mi, P. Bhattacharya, T. Zhu, and J. Xu, "Enhanced spontaneous emission at 1.55 μm from colloidal PbSe quantum dots in a Si photonics crystal microcavity," *Appl. Phys. Lett.*, vol.90, no.17, art. no.171105, 2007.

[117] R. Bose, X. D. Yang, R. Chatterjeee, J. Gao, and C. W. Wong, "Weak coupling interactions of colloidal lead sulphide nanocrystals with silicon photonic crystal nanocavities near 1.55 μm at room temperature," *Appl. Phys. Lett.*, vol.90, no.11, art. no.111117, 2007.

[118] W. W. Yu, J. C. Falkner, B. S. Shih, and V. L. Colvin, "Preparation and characterization of monodisperse PbSe semiconductor nanocrystals in a noncoordinating solvent," *Chem. Mater.*, vol.16, no.17, pp.3318-3322, 2004.

[119] J. Xu, D. H. Cui, T. Zhu, G. Paradee, Z. Q. Liang, Q. Wang, S. Y. Xu, and A. Y. Wang, "Synthesis and surface modification of PbSe/PbS core-shell nanocrystals for potential device applications," *Nanotechnology*, vol.17, no.21, pp.5428-5434, 2006.

[120] S. G. Johnson and J. D. Joannopoulos, *Photonic Crystals: the Road from Theory to Practice*, 1st edition (Kluwer, Dordrecht, 2002).

[121] T. Asano, B. S. Song, and S. Noda, "Analysis of the experimental Q factors (similar to 1 million) of photonic crystal nanocavities," *Opt. Express*, vol.14, no.5, pp.1996-2002, 2006.

[122] J. Topolancik, F. Vollmer, and B. Ilic, "Random high-Q cavities in disordered photonic crystal waveguides," *Appl. Phys. Lett.*, vol. 91, no. 20, art. no.201102, 2007.

[123] S. John, "Strong localization of photons in certain disordered dielectric superlattices," *Phys. Rev. Lett.*, vol. 58, no.23, pp.2486-2489, 1987.

[124] A. Yamilov, X. Wu, X. Liu, R. P. H. Chang, and H. Cao, "Self-optimization of optical confinement in an ultraviolet photonic crystal slab laser," *Phys. Rev. Lett.*, vol.96, no.8, art. no.083905, 2006.

[125] H. Cao and Y. G. Zhao, S. T. Ho, E. W. Seelig, Q. H. Wang, and R. P. H. Chang, "Random laser action in semiconductor powder," *Phys. Rev. Lett.*, vol. 82, no.11, pp.2278-2281, 1999.

[126] H. Cao, "Random lasers: development, features and applications," *Opt. & Photon. News*, pp.24-29, 2005.

[127] K. Y. Bliokh, Y. P. Bliokh, and V. D. Freilikher, "Resonances in one-dimensional disordered systems: localization of energy and resonant transmission," *J. Opt. Soc. Am. B*, vol.21, no.1, pp.113-120, 2004.

[128] H. C. Yuan and Z. Q. Ma, "Microwave thin-film transistors using Si nanomembranes on flexible polymer substrate," *Appl. Phys. Lett.*, vol.89, no.21, art. no.212105, 2006.

[129] www.compoundsemiconductor.net news, "IBM and Intel make high-k gate breakthrough," http://compoundsemiconductor.net/cws/article/news/26922, Jan 29, 2007.

[130] J. R. Liu, Z. G. Lu, S. Raymond, P. J. Poole, P. J. Barrios, and D. Poitras, "1.6-μm multiwavelength emission of an InAs-InGaAsP quantum-dot laser," *IEEE Photon. Tech. Lett.*, vol.20, no.2, pp.81-83, 2008.

[131] V. Jayaraman, Z. M. Chuang, L. A. Coldren, Theory, design, and performance of extended tuning range semiconductor lasers with sampled gratings, *IEEE J. Quantum Electron.*, vol.29, no.6, pp.1824-1834, 1993.

[132] E. Kapon ed., *Semiconductor lasers* (I and II), Academic Press, 1999.

[133] R. B. Swint, T. S. Yeoh, V. C. Elarde, M. S. Zediker, and J. J. Coleman, "High power single lateral mode diode lasers," *Proc. of SPIE*, vol.4973, pp.10-17, 2003.

[134] J. K. Wade, L. J. Mawst, D. Botez, J. A. Morris, "8.8 W CW power from broad-waveguide Al-free active-region (λ = 805 nm) diode lasers," *Electron. Lett.*, vol. 34, no. 11, pp.1100–1101, 1998.

[135] W. Pittroff, G. Erbert, G. Beister, F. Bugge, A. Klein, A. Knauer, J. Maege, P. Ressel, J. Sebastian, R. Staske, and G. Traenkle, "Mounting of high power laser diodes on boron nitride heat sinks using an optimized Au/Sn metallurgy," *IEEE Transactions on Advanced Packaging*, vol.24, no.4, pp.434-441, 2001.

[136] F.Gittes and C. F. Schmidt, "Interference model for back-focal-plane displacement detection in optical tweezers," *Opt. Lett.*, vol. 23, no.1, pp.7-9, 1998.

[137] R. W. Boyd, *Nonlinear Optics* (2nd edition), pp.111-117, Acadmic Press, 2003.

[138] S. M. Feng, H. G. Winful, R. W. Hellwarth, "Gouy shift and temporal reshaping of focused single-cycle electromagnetic pulses," *Opt. Lett.*, vol. 23, no.5, pp.385-387, 1998.

[139] R. W. McGowan, R. A. Cheville and D. Grischkowsky, "Direct observation of the Gouy phase shift in THz impulse ranging," *Appl. Phys. Lett.*, vol.76, no.6, pp.670-672, 2000.

[140] F. Lindner, G. G. Paulus, H. Walther, A. Baltuska, E. Goulielmakis, M. Lezius and F. Krausz, "Gouy phase shift for few-cycle laser pulses," *Phys. Rev. Letts.*, vol. 92, no.11, art. no.113001, 2004.

[141] N. C. R. Holme, B. C. Daly, M. T. Myaing, and T. B. Norris, "Gouy phase shift of single-cycle picosecond acoustic pulses,"*Appl. Phys. Lett.*, vol.83, no.2, pp.392-394, 2003.

[142] D. Marcuse, *Light transmission optics* (2nd edition), Ch1, Van Nostrand Reinhold Press, 1982.

[143] X. Deng and H. Fang, *Chinese J. Lasers*, vol.7, pp.14 (1980)

[144] H. Guo and X. M. Deng, "Differential geometrical methods in the study of optical-transmission (scalar theory): 1. Static transmission case," *J. Opt. Soc. Am. A*, vol.12, no.3, pp.600-606, 1995.

[145] S. C. Yap, B. C. Quek, K.S. Low, "Generalized eikonal approximation: 2. Propagation of stationary electromagnetic waves in linear and nonlinear media," *J. Opt. Soc. Am. A*, vol.15, no.10, 2725-2729, 1998.